

Air-sea fluxes with a focus on heat and momentum

Meghan F. Cronin^{1*}, Chelle L. Gentemann², James B. Edson³, Iwao Ueki⁴, Mark Bourassa⁵, Shannon Brown⁶, Carol A. Clayson³, Chris Fairall⁷, J. T. Farrar³, Sarah T. Gille⁸, Sergey Gulev⁹, Simon Josey¹⁰, Sieji Kato¹¹, Masaki Katsumata⁴, Elizabeth C. Kent¹⁰, Marjolaine Krug¹², Peter J. Minnett¹³, Rhys Parfitt³, Rachel T. Pinker¹⁴, Paul W. Stackhouse¹¹, Sebastiaan Swart¹⁵, Hiroyuki Tomita¹⁶, Doug Vandemark¹⁷, Robert A. Weller³, Kunio Yoneyama⁴, Lisan Yu³, Dongxiao Zhang¹⁸

¹Pacific Marine Environmental Laboratory (NOAA), United States, ²Earth and Space Research, United States, ³Woods Hole Oceanographic Institution, United States, ⁴Japan Agency for Marine-Earth Science and Technology, Japan, ⁵Florida State University, United States, ⁶NASA Jet Propulsion Laboratory (JPL), United States, ⁷Earth System Research Laboratory (NOAA), United States, ⁸Scripps Institution of Oceanography, University of California, San Diego, United States, ⁹P.P. Shirshov Institute of Oceanology (RAS), Russia, ¹⁰National Oceanography Centre, University of Southampton, United Kingdom, ¹¹Langley Research Center, United States, ¹²Council for Scientific and Industrial Research (CSIR), South Africa, ¹³Rosenstiel School of Marine and Atmospheric Science, University of Miami, United States, ¹⁴University of Maryland, College Park, United States, ¹⁵University of Gothenburg, Sweden, ¹⁶Institute for Space-Earth Environmental Research, Nagoya University, Japan, ¹⁷University of New Hampshire, United States, ¹⁸Joint Institute for the Study of the Atmosphere and Oceans, University of Washington, United States

Submitted to Journal:
Frontiers in Marine Science

Specialty Section:
Ocean Observation

Article type:
Review Article

Manuscript ID:
434858

Received on:
03 Nov 2018

Revised on:
06 Apr 2019

Frontiers website link:
www.frontiersin.org

Conflict of interest statement

The authors declare a potential conflict of interest and state it below

NOAA PMEL has had a Cooperative Research and Development Agreement (CRADA) with Saildrone, Inc. since 2014 that covers work with Saildrone ASV by MFC. This has involved in kind contributions from Saildrone, Inc. towards NOAA ASV missions. It is expected that this work will benefit NOAA's mission and the entire ASV industry. CG had a contract for 6 weeks of her time from Saildrone, Inc. The contract was to coordinate a 2-month Saildrone cruise that occurred in Spring 2018. DV had a contract for 2 weeks of his time from Saildrone Inc. in 2018 to advise on the data collection and processing of turbulent flux measurements using their platform.

Author contribution statement

MC, CG, JE and IU were first authors for abstracts that were merged into the present version. MC wrote first draft of the paper; CG, JE, SB, IU, EK, RW, SJ, RP, SK, CF, HT, PM, TF, SS contributed text sections; LY, MB, PM, and MC contributed figures; all authors contributed to manuscript revision, and read and approved the submitted version.

Keywords

Air-sea heat flux, Latent heat flux, surface radiation, ocean wind stress, Autonomous surface vehicle, OceanSITES, ICOADS, Satellite-based ocean monitoring system

Abstract

Word count: 347

Turbulent and radiative exchanges of heat between the ocean and atmosphere (hereafter heat fluxes), ocean surface wind stress, and state variables used to estimate them, are Essential Ocean Variables (EOVs) and Essential Climate Variables (ECVs) influencing weather and climate. This paper describes an observational strategy for producing 3-hourly, 25-km (and an aspirational goal of hourly at 10-km) heat flux and wind stress fields over the global, ice-free ocean with breakthrough 1-day random uncertainty of 15 W m⁻² and a bias of less than 5 W m⁻². At present this accuracy target is met only at OceanSITES reference station moorings and research vessels (RVs) that follow best practices. To meet these targets globally, in the next decade, satellite-based observations must be optimized for boundary layer measurements of air temperature, humidity, sea surface temperature, and ocean wind stress. In order to tune and validate these satellite measurements, a complementary global in situ flux array, built around an expanded OceanSITES network of time series reference station moorings, is also needed. The array would include 500 - 1000 measurement platforms, including autonomous surface vehicles, moored and drifting buoys, RVs, the existing OceanSITES network of 22 flux sites, and new OceanSITES expanded in 19 key regions. This array would be globally distributed, with 1 - 3 measurement platforms in each nominal 10° by 10° boxes. These improved moisture and temperature profiles and surface data, if assimilated into Numerical Weather Prediction (NWP) models, would lead to better representation of cloud formation processes, improving state variables and surface radiative and turbulent fluxes from these models. The in situ flux array provides globally distributed measurements and metrics for satellite algorithm development, product validation, and for improving satellite-based, NWP and blended flux products. In addition, some of these flux platforms will also measure direct turbulent fluxes, which can be used to improve algorithms for computation of air-sea exchange of heat and momentum in flux products and models. With these improved air-sea fluxes, the ocean's influence on the atmosphere will be better quantified and lead to improved long-term weather forecasts, seasonal-interannual-decadal climate predictions, and regional climate projections.

Funding statement

EK was funded by the NERC CLASS Programme (NE/R015953/1). CG was funded by NASA grant 80NSSC18K0837.

Data availability statement

Generated Statement: No datasets were generated or analyzed for this study.

1 **Air-sea fluxes with a focus on heat and momentum**

2 **Meghan F. Cronin^{1*}, Chelle L. Gentemann², James Edson³, Iwao Ueki⁴, Mark Bourassa⁵,**
3 **Shannon Brown⁶, Carol Anne Clayson³, Chris Fairall⁷, J. Thomas Farrar³, Sarah T. Gille⁸,**
4 **Sergey Gulev⁹, Simon A. Josey¹⁰, Seiji Kato¹¹, Masaki Katsumata⁴, Elizabeth Kent¹⁰,**
5 **Marjolaine Krug¹², Peter J. Minnett¹³, Rhys Parfitt⁵, Rachel T. Pinker¹⁴, Paul W. Stackhouse**
6 **Jr.¹¹, Sebastiaan Swart¹⁵, Hiroyuki Tomita¹⁶, Douglas Vandemark¹⁷, Robert A. Weller³, Kunio**
7 **Yoneyama⁴, Lisan Yu³, Dongxiao Zhang¹⁸**

8 ¹NOAA Pacific Marine Environmental Laboratory (PMEL), USA

9 ²Earth and Space Research, USA

10 ³Woods Hole Oceanographic Institution (WHOI), MA, USA

11 ⁴Japan Agency for Marine-Earth Science and Technology (JAMSTEC), Japan

12 ⁵Florida State University (FSU), USA

13 ⁶Jet Propulsion Laboratory (JPL), USA

14 ⁷NOAA Earth System Research Laboratory (ESRL), USA

15 ⁸University of California San Diego (UCSD), USA

16 ⁹P.P.Shirshov Institute of Oceanology (IORAS), Russia

17 ¹⁰National Oceanography Centre (NOC), UK

18 ¹¹NASA Langley Research Center, USA

19 ¹²Council for Scientific and Industrial Research (CSIR), South Africa

20 ¹³Rosenstiel School of Marine and Atmospheric Science (RSMAS), University of Miami USA

21 ¹⁴University of Maryland College Park, USA

22 ¹⁵University of Gothenburg, Sweden

23 ¹⁶Nagoya University Institute for Space-Earth Environmental Research (ISSEE), Japan

24 ¹⁷University of New Hampshire, USA

25 ¹⁸University of Washington Joint Institute for the Study of the Atmosphere and Ocean, USA

26 *** Correspondence:** Meghan F Cronin Meghan.F.Cronin@noaa.gov

27

28 **Keywords:** Air-sea heat flux, latent heat flux, surface radiation, ocean wind stress, autonomous
29 surface vehicle (ASV), OceanSITES, ICOADS, Satellite-based ocean monitoring system

30

31 *A submission for the OceanObs'19 Special Collection*

32

33 **Abstract**

34 Turbulent and radiative exchanges of heat between the ocean and atmosphere (hereafter heat fluxes),
 35 ocean surface wind stress, and state variables used to estimate them, are Essential Ocean Variables
 36 (EOVs) and Essential Climate Variables (ECVs) influencing weather and climate. This paper
 37 describes an observational strategy for producing 3-hourly, 25-km (and an aspirational goal of hourly
 38 at 10-km) heat flux and wind stress fields over the global, ice-free ocean with breakthrough 1-day
 39 random uncertainty of 15 W m^{-2} and a bias of less than 5 W m^{-2} . At present this accuracy target is
 40 met only at OceanSITES reference station moorings and research vessels (RVs) that follow best
 41 practices. To meet these targets globally, in the next decade, satellite-based observations must be
 42 optimized for boundary layer measurements of air temperature, humidity, sea surface temperature,
 43 and ocean wind stress. In order to tune and validate these satellite measurements, a complementary
 44 global *in situ* flux array, built around an expanded OceanSITES network of time series reference
 45 station moorings, is also needed. The array would include 500 - 1000 measurement platforms,
 46 including autonomous surface vehicles, moored and drifting buoys, RVs, the existing OceanSITES
 47 network of 22 flux sites, and new OceanSITES expanded in 19 key regions. This array would be
 48 globally distributed, with 1 - 3 measurement platforms in each nominal 10° by 10° boxes. These
 49 improved moisture and temperature profiles and surface data, if assimilated into Numerical Weather
 50 Prediction (NWP) models, would lead to better representation of cloud formation processes,
 51 improving state variables and surface radiative and turbulent fluxes from these models. The *in situ*
 52 flux array provides globally distributed measurements and metrics for satellite algorithm
 53 development, product validation, and for improving satellite-based, NWP and blended flux products.
 54 In addition, some of these flux platforms will also measure direct turbulent fluxes, which can be used
 55 to improve algorithms for computation of air-sea exchange of heat and momentum in flux products
 56 and models. With these improved air-sea fluxes, the ocean's influence on the atmosphere will be
 57 better quantified and lead to improved long-term weather forecasts, seasonal-interannual-decadal
 58 climate predictions, and regional climate projections.

59 **1 Introduction**60 **1.1 Societal importance of air-sea fluxes**

61 The oceans impact weather and climate by heating (and cooling) the lower atmosphere. In particular,
 62 as seawater evaporates, the ocean surface cools; and when the moisture later condenses into cloud
 63 droplets, this heat is released, warming the atmosphere. This moistening, and then warming, makes
 64 the air buoyant, driving low-level baroclinicity and atmospheric convection, causing wind
 65 convergence at the surface and divergence aloft. At the equator, ocean heating of the atmosphere can
 66 result in towering convective clouds that reach the top of the troposphere. These disturbances in turn
 67 drive teleconnections in the atmosphere, affecting weather and climate remotely. Most dramatically,
 68 every 2 - 7 years, zonal shifts in the surface heating patterns along the equatorial Pacific, associated
 69 with El Niño Southern Oscillation (ENSO), lead to climate extremes across the world. Patterns of
 70 surface heat fluxes (Figures 1, 2) also affect large-scale atmospheric circulation patterns, with deep
 71 convection over the thermal equator forming the upward branch of the “Hadley Cell” that drives
 72 trade winds. Westerly jet streams in both hemispheres are likewise associated with vertical-
 73 meridional cells in the midlatitude and high latitudes. Again, their rising branches and storm tracks
 74 are aligned with the surface heating of the atmosphere associated with warm ocean western boundary
 75 currents that extend into the midlatitude ocean basins (Figures 1, 2). These surface wind patterns,
 76 e.g., westerly winds at high latitudes and easterly trades in the tropics, in turn drive the ocean general
 77 circulation. Western boundary currents associated with the wind-forced subtropical ocean gyres are

particularly important as they carry warm water poleward, helping to transfer heat from the tropics (where there is greater heating of the earth's surface by solar radiation per area) to higher latitudes (where heat lost at the surface by latent and sensible heat flux and net infrared cooling is greater than that gained by solar radiation). As discussed in this paper, quantifying these air-sea fluxes, which represent the direct communication between the ocean and atmosphere, is challenging. Through the recommendations presented here, we believe that remaining large biases and uncertainties that result in differences in global fields (Figure 1c-f) could be reduced by up to an order of magnitude, enabling better resolution of phenomena on scales ranging from sub-diurnal and mesoscale to global and interannual.

Reducing inaccuracies (both biases and random uncertainty) in air-sea fluxes is important for improving long-term weather and climate predictions. Because the ocean's capacity to store heat is about 1000 times greater than that of the atmosphere, long-term weather and climate predictability has its origins in the oceans. Heat storage and release occurs on a range of time scales (Figure 2; Table S1) and can provide predictability out to 10 - 100 days (e.g., Madden-Julian Oscillation, Asian/Indian Monsoon), on seasonal-interannual time scales (e.g., ENSO), and out to decades (e.g., Pacific Decadal Oscillation, Atlantic Multidecadal Oscillation). Predictions of weather and climate on these time scales have great economic benefits for agriculture, water resource management, energy management, human and ecosystem health among others. Thus, to achieve useful predictions we must be able to quantify where, when and how much heat is released to the atmosphere. As a first step, here, we discuss strategies for improving our ability to quantify the amount of heat that at present is being exchanged between the ocean and atmosphere, regionally and globally. Because these air-sea heat exchanges are highly related to the surface dynamics and turbulent properties, we will also address quantification of wind stress.

Strong air-sea fluxes can occur on short time and space scales (Figure 2; Table S1), challenging both *in situ* (because of technical difficulties in extreme conditions and undersampling) and satellite observations (because of grid-averaging). The primary external time scales affecting air-sea fluxes are the diurnal cycle and the annual cycle associated orbital forcing. Internal dynamics lead to a range of other time and space scale variability in wind stress and air-sea heat fluxes. Sea-surface temperature (SST) fronts in the ocean are particularly critical to air-sea fluxes. The largest magnitude and temporal variability of air-sea fluxes is found in regions associated with SST fronts, specifically at western boundary currents such as the Gulf Stream, where intense poleward currents carry warm tropical water into the subtropics. In winter, large ocean heat loss is associated with cold air outbreaks, when cold and dry air blowing over much warmer water drive frequent episodic high flux events (e.g., Bond and Cronin, 2008; Shaman et al., 2010; Tilinina et al., 2018). Additionally, the intense SST gradients at ocean fronts result in strong heat flux gradients. These strong gradients in heat flux are known to be crucial for modulating both synoptic atmospheric variability and in turn the mean atmospheric state (Parfitt et al., 2016; Parfitt and Seo, 2018). Away from ocean fronts, whilst turbulent mixing of colder and dryer air aloft generally results in a near surface air temperature cooler than the SST and relative humidity less than 100%, the net surface heat loss from the ocean is much weaker. As will be discussed below, there are many challenges associated with resolving air-sea fluxes in regions of strong ocean fronts.

Because the specific heat capacity of water is considerably larger than that of land, air temperature is more variable over land than over the oceans, leading to a tendency for milder coastal climates than inland. Oceanic heat loss due to evaporation is associated with moisture fluxes that are an important source of water for agriculture and human consumption. Understanding and quantifying the exchange

123 of heat and momentum between the ocean and atmosphere is therefore critically important for proper
 124 management of natural resources and reducing risks to vulnerable populations.

125

126 1.2 Quantifying Air-Sea Exchanges of Heat and Momentum

127 The net surface heat flux (Q_{net}) comprises net shortwave (i.e., solar) (Q_{SW}) and net longwave (i.e.,
 128 infrared (IR) (Q_{LW}) radiative fluxes, and surface turbulent (latent and sensible) heat fluxes:

$$129 \quad Q_{net} = Q_{SW} - Q_{LW} - Q_{lat} - Q_{sen} \quad (1.1)$$

130 Surface latent heat flux, Q_{lat} , is the heat extracted from the ocean when seawater evaporates. This
 131 heat is released to the atmosphere when and where this vapor condenses, forming clouds. Likewise,
 132 sensible heat flux, Q_{sen} , is the heat extracted from the ocean associated with an air-sea temperature
 133 difference. The sign convention used here enables each term to be expressed generally as a positive
 134 value (i.e., as a magnitude) for most applications. When averaged over the global oceans and a full
 135 year, there should be a near-balance between solar radiative heating of the ocean (reduced by net
 136 longwave radiative heat loss), latent heat loss due to evaporation and sensible heat loss induced by
 137 air-sea temperature and humidity differences. However, due to biases in flux estimates, existing
 138 products have difficulties closing the heat budget, as discussed in section 2.3.

139 The net shortwave radiation flux, Q_{SW} , is the net difference between the incoming (i.e.,
 140 downwelling, $SW \downarrow$, and reflected outgoing shortwave radiations, $SW \uparrow$, and is commonly computed
 141 using a surface shortwave albedo, $\alpha = SW \uparrow / SW \downarrow$, estimate:

$$142 \quad Q_{SW} = SW \downarrow - SW \uparrow = SW \downarrow (1 - \alpha). \quad (1.2)$$

143 Likewise, because the outgoing surface longwave radiation $LW \uparrow$ comprises both the IR radiation
 144 emitted by the surface of the ocean and the portion of atmospheric downwelling IR radiation $LW \downarrow$
 145 that is not absorbed by the ocean surface, the net longwave radiation flux, Q_{LW} , can be expressed as:

$$146 \quad Q_{LW} = LW \uparrow - LW \downarrow = \epsilon \sigma_{SB} T_s^4 + (1 - \epsilon) LW \downarrow - LW \downarrow = \epsilon (\sigma_{SB} T_s^4 - LW \downarrow) \quad (1.3)$$

147 where ϵ is the IR surface emissivity ($\epsilon = 1$ for black-body emission) and is taken to be equal to the
 148 absorptivity, σ_{SB} is Stefan-Boltzmann constant, and T_s is the surface (skin) temperature that is
 149 emitting the IR-radiation, in degrees Kelvin. The skin temperature of the ocean is generally cooler
 150 than the water beneath, as the ocean is nearly always and everywhere giving heat to the atmosphere
 151 (Fairall et al., 1996a). On the aqueous side of the interface, viscosity and the air-sea density
 152 difference prevent the turbulent transfer of heat from ocean to atmosphere and so the heat supplied to
 153 the interface to feed the latent and sensible heat fluxes and into the layer that emits infrared radiation
 154 to the atmosphere, is provided by molecular conduction, which requires a vertical temperature
 155 gradient. This temperature gradient is referred to as the thermal skin layer (Donlon et al., 2002;
 156 Minnett et al., 2011). As a result, the surface layer of the ocean is in nearly all cases cooler than at a
 157 depth of a millimeter or so. The thickness of the layer emitting infrared radiation that is subsequently
 158 measured by satellite radiometers to derive SST is comparable to the thermal skin layer (~ 0.1 mm;
 159 Wong and Minnett 2016a, 2016b, 2018), and so the derived temperature is referred to as the ocean
 160 skin temperature.

The latent and sensible heat fluxes are typically estimated from state variables, using a “bulk flux algorithm” (e.g., Fairall et al., 2003). As described in section 1.2.1, the primary state variables for turbulent fluxes, including wind stress, are surface winds relative to surface currents, skin temperature, near-surface air temperature, and near-surface humidity. Because most *in situ* estimates of the oceanic near-surface properties are below the skin, as discussed in section 1.2.2, parameterizations must be used to extrapolate the bulk sea surface measurements to the air-sea interface. Likewise, as described in section 1.2.2, flux EOV and ECV for the surface radiation include downward solar radiation, upward solar radiation (or surface albedo), downward longwave radiation, skin temperature, and longwave surface emissivity. We refer to the variables listed here as the “flux Essential Climate Variables (ECVs)” and “flux Essential Ocean Variables (EOVs)”.

171

172 1.2.1 Turbulent momentum and heat flux EOV and ECVs

The surface momentum (aka wind stress), sensible heat and latent heat fluxes provide surface boundary conditions for turbulent flux profiles in the lower atmosphere and upper ocean. These surface turbulent fluxes are most directly quantified by measuring the direct covariance (aka eddy correlation) between the fluctuating vertical velocity that drives the exchange with the fluctuating quantity of interest within the constant flux layer above the air-sea interface. For example, the directly measured latent heat flux is determined from

$$179 \quad Q_{lat} = \rho L_v \langle wq \rangle \quad (1.4)$$

where ρ is the density of air; L_v is the latent heat of evaporation, w and q represent the fluctuating vertical velocity and specific humidity, respectively, and the brackets denote a temporal average of, generally, an hour or less. The turbulent fluxes, however, are difficult to measure at sea due to challenges that include platform motion contamination, flow distortion, high power requirements, rain and sea-spray contamination. Additionally, numerical forecast models do not resolve near surface turbulence, so surface fluxes must be parameterized.

These parameterizations are typically based on the assumption that the flux of some quantity is proportional to the vertical gradient of that quantity, e.g., the latent heat flux is proportional to the gradient in specific humidity. This approach, commonly referred to as the gradient or profile method, provides first-order closure in numerical models. The approach therefore requires vertical profiles of the observed or model-resolved non-turbulent state variables of temperature, specific humidity and velocity. The multiplicative factor that relates the flux to the gradient is known as the eddy viscosity for the momentum flux and the eddy diffusivity for the heat fluxes, e.g., the latent heat is determined from

$$194 \quad Q_{lat} \approx -\rho L_v K_q \frac{\partial q}{\partial z} \quad (1.5)$$

where K_q is the eddy diffusivity for moisture, and $\partial q / \partial z$ is the vertical gradient of the mean specific humidity. Commonly used parameterizations of the eddy viscosity and diffusivity in the surface (constant flux) layer assume that the efficiency of mixing by turbulent eddies scales with the height above the ocean surface. The efficiency of mixing is also a function of atmospheric stability, where mixing is suppressed under stable (thermally stratified) conditions and enhanced in unstable (convective) conditions. These two considerations predict semi-logarithmic profiles that includes a function that accounts for atmospheric stability.

202 It is also difficult, however, to measure vertical profiles and implement the gradient method over the
 203 ocean due to many of the challenges given for the direct covariance method. Instead, the surface
 204 fluxes are generally estimated using sea-air differences in the mean “bulk” state variables measured
 205 (or modeled) at the surface and at some height within the surface layer. The bulk aerodynamic
 206 method links the turbulent fluxes to mean air-sea velocity, temperature and humidity difference using
 207 transfer coefficients:

$$208 \quad \tau_x = -\rho \langle uw \rangle \approx \rho C_D S \Delta U, \quad \tau_y = \rho \langle vw \rangle \approx \rho C_D S \Delta V, \quad (1.6a)$$

$$209 \quad Q_{lat} = \rho L_v \langle wq \rangle \approx \rho L_v C_E S \Delta Q, \quad (1.6b)$$

$$210 \quad Q_{sen} = \rho c_p \langle w\theta \rangle \approx \rho c_p C_H S \Delta \theta, \quad (1.6c)$$

211 where c_p is specific heat at constant pressure; u and v are the fluctuating along-wind and cross-wind
 212 velocity components, respectively; and θ is the fluctuating potential temperature; C_D , C_E , and C_H are
 213 the transfer coefficients (known as the drag coefficient) for momentum, latent heat and sensible heat,
 214 respectively; S is the scalar wind speed relative to the ocean surface that includes gustiness; and
 215 ΔU , ΔV , ΔQ , and $\Delta \theta$ are the sea-air differences in the along-wind, crosswind, specific humidity and
 216 potential temperature, respectively.

217 At low winds, convective conditions, large-scale eddies drive gustiness that results in differences
 218 between the vector average wind components, U and V , and the wind speed, S , that includes
 219 gustiness. Convective gustiness has been shown to drive surface fluxes even when the vector-
 220 averaged winds are close to zero (Beljaars, 1995; Fairall et al., 1996b). However, the wind speed is
 221 difficult to measure on a moving platform due to wave contamination of the anemometers (i.e.,
 222 vector averaging is used to remove this contamination but at the expense of gustiness). Additionally,
 223 the momentum equations in numerical models generally predict the vector components. Therefore, a
 224 common solution is to add convective gustiness to the vector averaged winds such that $S^2 = U^2 +$
 225 $V^2 + U_g^2$ where U_g represents the gustiness due to convection. This is the approach used in the
 226 COARE algorithm (Fairall et al., 1996b). However, gustiness parameterizations that provide a single
 227 value of U_g regardless of height are physically inconsistent as convective gustiness is expected to
 228 vary with height within the boundary layer. More work is needed on this topic.
 229

230 Although difficult, direct covariance estimates of the fluxes have been successfully measured from a
 231 variety of over-ocean platforms or a wide range of conditions as described in section 2. These fluxes
 232 provide direct estimates of the transfer coefficients after normalization of the appropriate bulk state
 233 variables as given by 1.6. The measured transfer coefficients are then used to develop
 234 parameterizations of these coefficients that take into account two principal effects: atmospheric
 235 stability and ocean surface roughness. For example, direct measurements of the momentum flux are
 236 used to parameterize the drag as

$$237 \quad C_D = \frac{-\langle uw \rangle}{S \Delta U} = \left(\frac{\kappa}{\ln(z/z_0) - \psi_u} \right)^2 \quad (1.7)$$

238 where the middle term is the measured drag coefficient and the last term is a parameterization that
 239 includes a roughness length, z_0 , and a function that accounts for stability, ψ_u . This formulation is
 240 based on the assumption of a semi-logarithmic profile in the marine surface layer.

The impact of atmospheric stability is generally determined using Monin-Obukhov Similarity (MOS) scaling. MOS is used to develop functions (e.g., ψ_u) that account for the effects of stability in three overall stability classes: 1) neutral conditions, 2) unstable or convective conditions, and 3) stable or stratified conditions. Neutral surface layers are associated with high winds and little solar heating where turbulent mixing is driven by wind shear. The stability function equals zero under neutral conditions, i.e., $\psi_u(\text{neutral}) = 0$, in the absence of convection or stratification. Unstable surface layers range from situations where turbulent mixing is completely driven by convective processes (aka free convection) to more common situations where the mixing is driven by both buoyancy and wind shear (aka forced convection). Stable surface layers force the wind shear to do work against the stratification, thereby inhibiting mixing and turbulent exchange.

While the form of the stability functions can be guided by scaling arguments (e.g., in the free convective limit), the actual form of these functions must be determined empirically from direct measurements. Successful formulations are able to parameterize the entire range of stability classes. Reasonably consistent formulations have been determined through observations in a number of overland (e.g., Dyer and Hicks, 1970; Businger et al., 1971; Dyer and Bradley, 1982), over-ice (e.g., Grachev et al., 2007) and overwater (e.g., Edson and Fairall, 1998; Vickers and Mahrt, 1999; Edson et al., 2004, 2007, 2013) investigations, which have shown MOS scaling to be valid as long as the assumptions central to its application are not violated. These include a constant turbulent flux layer, stationarity and horizontal homogeneity.

Before developing parameterizations that account for the varying roughness of the underlying sea surface, the impact of atmospheric stability must first be removed (e.g., Fairall et al., 1996b). This is done using the MOS stability functions by adjusting the transfer coefficients to neutral conditions where, e.g., $\psi_u(0) = 0$ and the neutral drag coefficient is defined as $C_{DN} = (\ln(z/z_0))^2$. The roughness length is commonly parameterized using the roughness Reynolds number for smooth flow to provide the surface “roughness” at low winds (Smith, 1988). Other low wind studies have suggested the use of Weber number scaling to parameterize the roughness as a function of surface tension (Wu, 1994). The low-wind roughness is added to another roughness length that accounts for the increasing roughness of surface waves at increasingly higher wind speeds. This roughness length commonly relies on a relationship suggested by Charnock (1955). The Charnock relationship effectively models the surface roughness due to wind-waves as the ratio of surface forcing (i.e., the surface stress) to the restoring force of gravity. This ratio is multiplied by a variable of proportionality known as the Charnock parameter.

The Charnock parameter is expected to account for the wide-range of physical processes that impact wind-wave interaction. Therefore, it should come as no surprise that there is a wide range of published parameterizations of the Charnock parameter. The transfer coefficients are known to have a wind speed dependence – strong for C_D and weak for C_E and C_H . This dependence has naturally led to the parameterization of the transfer coefficients as a function of wind speed (e.g., Large and Pond, 1981) or using a wind-speed dependent Charnock parameter (e.g., Fairall et al., 2003). Other bulk algorithms have explicit dependencies on sea state (e.g., significant wave height, wave period and wave steepness, wave-age, directional differences between the wind and wave fields), and fraction of ice cover. Such dependencies in measured fluxes are often modelled using Charnock’s relationship where the Charnock parameter is parameterized in terms of the wind-speed, wave-slope, wave-age and ice fraction. However, understanding the relation between the roughness parameter and the sea state, and likewise the effect of sea state on the relative winds, remains an area of active research (e.g., Liu et al., 1979; Large and Pond, 1981; Donelan et al., 1993; Mahrt et al., 1996; Fairall et al.,

286 1996b, 2003; Bourassa et al., 1999; Brunke et al., 2003; Drennan et al., 2005; Edson et al., 2013;
 287 Hristov and Ruiz-Plancarte, 2014).

288 The impact of waves on air sea-fluxes also extends to the sensible and latent heat fluxes. For
 289 example, many formulations of the transfer coefficients for sensible and latent heat include the drag
 290 coefficient to the one-half, $C_D^{1/2}$, times a scalar component for heat and moisture; e.g., the transfer
 291 coefficient for latent heat can be defined as $C_E = C_D^{1/2} C_q$ where C_q is the scalar component of the
 292 moisture transfer. This formulation predicts that any wave-related dependencies in the drag
 293 coefficient will be included in these formulations in a somewhat muted form. Analogous to the
 294 aerodynamic roughness length used to define the drag coefficient, the scalar components are
 295 commonly defined using “thermal” roughness lengths. For example, the transfer coefficient for latent
 296 heat has been defined as

$$297 \quad C_E = C_D^{1/2} C_q = \left(\frac{\kappa}{\ln(z/z_0) - \psi_u} \right) \left(\frac{\kappa}{\ln(z/z_{0q}) - \psi_q} \right) \quad (1.8)$$

298 where z_{0q} is the thermal roughness length for moisture and ψ_q is a MOS stability function for
 299 humidity. The thermal roughness lengths are often parameterized as a function of the roughness
 300 Reynolds number, which is defined using the aerodynamic roughness length (see Liu et al., 1979 and
 301 Fairall et al., 1996b for details). As such, any wave-related parameterization of the aerodynamic
 302 roughness length will also be included in the thermal roughness lengths.

303 The more sophisticated algorithms account for the difference between a bulk water temperature and
 304 the interface temperature, wind gustiness, and surface currents, as discussed in section 1.2.2.
 305 However, there is a balance between increasing parameterization complexity and hence dependence
 306 on additional variables that may be uncertain or unknown, and improvements that may be gained by
 307 considering additional physics. The COARE algorithm transfer coefficients are claimed to be
 308 accurate **on average** to approximately $\pm 5\%$ for C_D and C_E (set equal to C_H) for wind speeds from 2 to
 309 20 m s^{-1} . By this we mean that some 15,000 hours of direct flux measurements, converted to transfer
 310 coefficients, and averaged in wind speed bins will be within 5% of the COARE transfer coefficients
 311 at the same wind speed. The scatter of individual 1-hr measured values is about 25% and are
 312 generally wind speed and certainly platform dependent. This scatter is principally sampling error and
 313 is well-understood in terms of turbulence statistical theory (Blomquist et al., 2014). Research
 314 challenges that could lead to improved bulk flux parameterizations include:

- 316 • Development of **wave-dependent surface flux parameterization** that outperform wind-
 317 speed dependent parameterizations under a wide range of wind, wave and current conditions.
- 318 • Development of **flux-profile relationships** that account for both stratification and wave-
 319 induced perturbations on the wind profile though the wave boundary layer (WBL) and
 320 beyond under a wide range of wind, wave and current conditions.
- 321 • Development of surface flux and flux-profile relationships that account for **directional
 322 differences between the wind and wave fields**.
- 323 • Development of **Geophysical Model Functions (GMF)** to provide remotely sensed surface
 324 stress estimates that match or exceed the accuracy of bulk fluxes using in situ measurements.
- 325 • Development of **convective gustiness parameterizations** that are valid through the surface
 326 layer to the lowest grid point in high resolution forecast models.
- 327 • Development of **gustiness parameterizations for coherent structures** such as roll vortices
 328 in forced convection.

- Validation and continued development of models to simulate **evaporating sea-spray** and their impact on momentum, heat and mass fluxes under high to extreme wind conditions.
- Development of **scale-dependent flux parameterizations** for nested high-resolution models down to Large Eddy Simulation (LES) scale.
- Development of **coupled LES** with sufficient accuracy to simulate wind-wave-current interaction near the ocean surface to provide output that can be considered data for parameterization and model development.

In summary, modern bulk algorithms need to better incorporate the impact of waves and currents on the magnitude and direction of the surface stress and their modulation of fluxes and mean profiles (e.g., Grachev et al., 2003; Hara and Belcher, 2004; Hristov and Ruiz-Plancarte, 2014; Buckley and Veron, 2016; Grare et al., 2013, 2018; Cifuentes-Lorenzen et al., 2018). The wavy boundary layer and shallow atmospheric boundary layers provide a number of additional challenges associated with sea-spray, gustiness, severe stratification and extreme winds. The impact of boundary layer processes on surface fluxes above the surface layer are best studied with additional boundary layer measurement in combination with numerical models and simulations. Therefore, resolving the main issues with bulk algorithms will require a combination of field observations and specialized atmosphere-wave models. Because of the many dependencies, detailed research models such as advance wave codes (e.g., Banner and Morison, 2010; Kukulka et al., 2007; Kudryavtsev et al., 2014) and wave-LES models (e.g., Sullivan et al., 2014, 2018; Hara and Sullivan, 2015), in combination with observations in many different regimes, can provide a rational way to explore the phase space of parameterization variables.

1.2.2 Parameterizations to extrapolate measurements to air-sea interface

While the transfer coefficients used in bulk algorithm introduce some uncertainty into the estimation of the surface air-sea fluxes, perhaps a larger uncertainty comes from treatment of the flux state variables used to estimate the flux. In particular, for most state-of-the-art bulk algorithms, the sea surface temperature (SST) and specific humidity are assumed to be ocean skin values. If instead, a bulk sea temperature is used (i.e., sea temperature measured at depths ranging between 0.01 and 5 m or even deeper), then it should be adjusted to the surface using either parameterizations or models. Fairall et al. (1996a), for example, uses first estimates of the net surface heat flux and wind stress to force a one-dimensional mixed-layer model of the diurnal warm layer relative to the pre-dawn conditions. This is then used to account for stratification (i.e., the warm layer) above the depth of the bulk temperature measurement. Fairall et al. (1996a) also provides a “cool skin” model to account for the surface cooling from non-solar radiative components of the net surface heat flux to compute the SST or skin temperature. Other methods exist for making these extrapolations. For example, the Webster et al. (1996) method relies upon a specification of wind speed and peak solar flux to compute the diurnal warm SST variability at the surface. Parameterizations in terms of wind speed lead to a simple thermal skin effect correction (Donlon et al., 2002; Minnett et al., 2011). For tropical open ocean environments, the average warm layer correction leads to about a 5 W m^{-2} increase in Q_{net} , while the average cool skin adjustment is a decrease of about 10 W m^{-2} . However, corrections due to the warm layer can lead to substantially larger fluxes when the measurements are made at depth in the presence of large diurnal warming events.

Likewise, for these state-of-the-art bulk algorithms, surface current estimates are needed to compute the wind speed and vertical wind shear relative to ocean surface as given by ΔU and ΔV in Equation (1.6). The resulting changes in stress are usually small compared to the stress except in regions of strong currents such as over western boundary currents. However, ignoring surface currents in the

development of flux parameterization can lead to a systematic bias in the transfer coefficients (Edson et al., 2013) as the wind- and wave-driven currents are generally in the direction of the wind. As a result, the wind speed relative to water is generally smaller than the wind speed relative to earth. These differences are also large enough to cause substantial errors in the horizontal gradient of stress, which can have substantial impact on ocean circulation, upwelling, biology and biogeochemistry (Shi, 2017). Surface currents, however, are generally measured *in situ* at 10 m or deeper. There is growing appreciation that there can be non-negligible shear within the upper 10 m on timescales of the flux calculations. This can add to the errors in the relative wind, and potentially to errors in the flux parameterizations if the currents are not consistently adjusted to the surface. Brodeau et al. (2017) estimated the effect of surface currents on the wind stress to be on average within $\pm 0.005 \text{ N m}^{-2}$ with the largest uncertainties amounting to $0.02\text{--}0.025 \pm 0.005 \text{ N m}^{-2}$.

387

388 **1.2.3 Radiative heat flux EOV/ECV**

The net radiative component of the air-sea heat flux comprises a shortwave component that is emitted by the sun ($\text{SW}\downarrow$) and reflected from the ocean surface ($\text{SW}\uparrow$) in the spectral range of 0.3–4.0 μm , and a longwave component that is emitted by the atmosphere ($\text{LW}\downarrow$) and surface ($\text{LW}\uparrow$) in the spectral range of 4.0–100.0 μm (Equations 1.1–1.3). $\text{SW}\downarrow$ has a direct and a diffuse component that interacts differently with the underlying surface due to differences in their spectral composition and angularly dependent properties. About half of the solar radiation incident on the top of the atmosphere reaches the surface of the Earth after being transmitted through the atmosphere. Extinction of solar radiation in the atmosphere is mostly by ozone, water vapor, clouds, and aerosols. The vertical profiles of clouds, water vapor, and temperature largely determine the longwave emission by the atmosphere. Clouds play a major role in determining the net radiative balance at the surface, dependent on their amount and optical properties (e.g., optical depth, a general measure of the capacity of a cloud to control the amount of light that will reach the surface). Most atmospheric constituents (e.g., cloud, aerosols, and water vapor) can now be derived from satellite instruments. At the ground, $\text{SW}\downarrow$ is measured with pyranometers (spectral range of 0.310 to 2.800 μm) and $\text{LW}\downarrow$ is measured with pyrgeometers (spectral range of 4.5 to 42 μm). The upward component of the surface solar radiation, $\text{SW}\uparrow$, depends upon $\text{SW}\downarrow$ spectral composition controlled by the solar zenith angle, atmospheric and cloud properties, as well as the surface optical properties, which depend upon the sea state (i.e., wind speed) and chlorophyll concentration in the upper ocean (Jin et al., 2004). *In situ* measurements of $\text{SW}\uparrow$ are very rare and thus it is typically estimated from the $\text{SW}\downarrow$ and surface albedo, α (Equation 1.2).

The strong albedo dependence upon solar zenith angle means that more reflection occurs at lower sun angles (during dawn and dusk, in winter and at higher latitudes). Payne (1972) used observations of both upwelling and downwelling shortwave radiation to develop a relation between albedo and solar zenith angle and atmospheric transmittance. At low solar zenith angles, the albedo is 0.03 to 0.06, but at high solar zenith angles it can approach 0.3. Li et al. (2006) examined wind speed and zenith angle dependent models of the albedo from the perspective of upwelling shortwave at the top of the atmosphere. They found that differences among models were less than 10 W m^{-2} and the difference in the global mean was within $\pm 2.5 \text{ W m}^{-2}$ compared with Clouds and the Earth's Radiant Energy System (CERES) data. In the TOGA COARE bulk formulae, Fairall et al. (1996a) use a fixed albedo of 0.055. Errors in albedo can introduce errors in the net shortwave radiation and air-sea heat flux. Further work is needed to improve albedo parameterizations for use in state of the art bulk algorithms, NWP, and satellite radiation algorithms.

421 *In situ* observations of longwave radiation at sea have become more common only in the last ten to
 422 twenty years. Prior to that, various bulk formulae for net longwave radiation at the sea surface were
 423 used that depended upon air- and sea-surface temperature, humidity, cloud cover (and type), and
 424 latitude (Fung et al., 1984). While *in situ* observations are used for local radiation budgets and for
 425 validations of computed radiative fluxes, only satellite observations can provide surface radiative
 426 fluxes at a global scale. To estimate radiative fluxes from satellite observations, we need to rely on
 427 radiative transfer models. Inputs for radiative transfer models include temperature and water vapor
 428 specific humidity vertical profiles, and cloud and aerosol properties. The accuracy of these properties
 429 largely influences the accuracy of surface radiative flux computations. Surface radiative fluxes are
 430 especially sensitive to near surface temperature and humidity profiles and boundary layer cloud
 431 properties. Consequently, improvements to these near surface properties are critical for reducing
 432 uncertainty in satellite-derived surface radiative fluxes.

433

434 2 Current capabilities

435 Quantifying the air-sea fluxes over the global ice-free oceans requires a hierarchy of observations
 436 specifically targeted for (1) improving understanding of processes controlling air-sea exchange and
 437 their relationship to atmospheric and oceanic state variables, and specifically, for improving the “bulk
 438 algorithm” for computing these fluxes; (2) measuring flux EOVs and ECVs over the global ice-free
 439 ocean with sufficiently high spatial and temporal resolution, coverage, and accuracy to generate the
 440 global flux products; and (3) obtaining high-quality long time series and regionally distributed
 441 measurements that can be used for validating and improving these flux products. Here we describe the
 442 current capabilities of the *in situ* networks for measuring air-sea heat and momentum fluxes, and
 443 remotely sensed capabilities. Each has its strengths and weaknesses and NWP are commonly used to
 444 integrate these disparate observations into dynamically consistent fields. We thus also describe current
 445 capabilities in NWP and hybrid NWP flux products.

446

447 2.1 Current capabilities for *in situ* flux EOV/ECV measurements

448 2.1.1 ICOADS

449 The International Comprehensive Ocean-Atmosphere Data Set (ICOADS, Freeman et al., 2017,
 450 2019) collates surface marine data extending back three centuries. Before about 1970 almost all
 451 ICOADS observations are from ship voyages but as ocean technology has developed, data from more
 452 platforms (surface moorings, drifters, floats) have been incorporated into the archive. At present,
 453 nearly all near-real time surface marine data available through the Global Telecommunication
 454 System (GTS) are incorporated into the database and periodically data from delayed mode archives
 455 are incorporated. Flux ECV and EOVs available through ICOADS include: SST, air temperature,
 456 humidity, wind speed and direction, barometric pressure, visually observed characteristics of sea
 457 state, and coded weather information. ICOADS contains few radiation measurements, but does
 458 contain visually observed cloud observations (Eastman et al., 2011). Sampling in ICOADS is very
 459 heterogeneous with observations concentrated in the major shipping routes of the Northern
 460 Hemisphere. Sampling errors in surface turbulent fluxes computed from ICOADS reports may
 461 amount to more than 60 W m^{-2} in poorly sampled regions (e.g., Gulev et al., 2007). ICOADS
 462 observations can be challenging to use, but if handled with care, ICOADS provides data for *in situ*
 463 flux calculations and global surface flux products (Josey et al., 1999; Berry and Kent, 2009).
 464 ICOADS also provides a major input data source for reanalyses (e.g., ERA-Interim: Dee et al., 2011;

465 20th Century Reanalysis: Compo et al., 2011; and CFSR: Saha et al., 2010). ICOADS is also the
 466 main *in situ* data source for the construction of gridded analyses of surface marine ECVs and EOFs
 467 including those used as surface boundary conditions for atmospheric reanalyses (e.g., HadSST3:
 468 Kennedy et al., 2011; ERSSTv5: Huang et al.; 2017; COBE-SST2: Hirahara et al., 2014;
 469 HadNMAT2: Kent et al., 2013). Additionally, ICOADS data are used for satellite data calibration
 470 and evaluation (e.g., Jackson and Wick, 2010; Liman et al., 2018; Tomita et al., 2018), as well as
 471 long-term regional reconstructions of surface fluxes (Gulev et al., 2013). ICOADS is an archive for
 472 observations but requires access to expertly-managed data from each different network type.
 473 Presently there is no international system for the expert management and archival of observations
 474 from the GTS although several national weather services maintain their own collections.

475

476 **2.1.2 *In situ* sensors for measuring fluxes**

477 A typical set up to estimate the momentum, sensible heat and latent heat flux on a moving platform
 478 includes a 3-axis sonic anemometer/thermometer; a 3-axis motion package and an open path infrared
 479 hygrometer. Sonic anemometers/thermometers have become the tool of choice for marine research.
 480 Although they experience some dropouts and occasional spikes, particularly in rain, they are
 481 generally very reliable in the marine environment. Motion sensors are finding their way into many
 482 (non-marine) applications. As a result, researchers now have a number of small, low-power,
 483 reasonably inexpensive and sufficiently accurate motion packages to choose from. The infrared
 484 hygrometer is ideally deployed alongside a system that flushes the optics between rain events. A
 485 closed-path hygrometer avoids many issues associated with contamination of the optics. However,
 486 experience has shown that they suffer from uncorrectable attenuation of the signal due to the sticky
 487 nature of water vapor within sampling tubes in high humidity environments. The fluxes should be
 488 measured using the wind velocity relative to water, which requires a 2-axis current meter.
 489 Investigation of wind-wave interaction requires surface wave information for the wave height, wave
 490 direction and wave period to compute variables such as wave-slope and wave-age from directional
 491 wave spectra. These estimates can be made from ships and surface moorings with some difficulty and
 492 limits in the frequency/wavenumber resolution due to the size of the platform. Instead, the latest
 493 generation of directional wave-buoys are recommended for these investigations. These buoys have
 494 onboard processing and near real-time data telemetry of key wave parameters. They are small enough
 495 to resolve a large fraction of the shorter wind-wave spectra in addition to the dominant waves. There
 496 is also a growing use of fast-response pressure sensors to investigate pressure-work and energy
 497 transfer primarily from fixed towers and specialized research platforms like the Floating Instrument
 498 Platform (*R/P FLIP*). The latest generation of these sensors appear to measure absolute pressure to
 499 sufficient accuracy for these studies. The main challenge, however, is in the design of the sensor head
 500 required to remove dynamic pressure fluctuations to isolate the desired static pressure fluctuations.

501 The meteorology sensors are best deployed at a height above the wavy boundary layer
 502 (corresponding to the height of the dominant waves or more about mean sea level) due to issues that
 503 arise when attempting to measure the fluxes too close to the ocean surface. Specifically, since the
 504 size of the turbulent eddies supporting the fluxes scales with the height above the surface, ever higher
 505 frequency measurements are required to capture the flux as one nears the surface (Kaimal et al.,
 506 1972). Similarly, stronger winds shift energy toward higher frequencies. However, there is an
 507 inherent limitation to the size of the eddies that can be measured with sonic anemometers and
 508 infrared hygrometers. This stems from the ~10 cm path length of these devices, which means that any
 509 fluctuations smaller than this length are path-averaged and unresolvable. This limits their ability to
 510 capture the flux and resolve the inertial subrange very near the ocean surface, particularly at high

winds, no matter how fast the sampling is. High winds also produce sea spray that poses a number of measurement challenges (Andreas et al., 2008, 2015). Besides the challenge of actually measuring spray to investigate their modulation of the fluxes (e.g., Richter and Veron, 2016), the droplets are known to contaminate sensors used to measure the latent heat (moisture) flux. In fact, the direct measurement of latent heat flux under high wind and rainy conditions remains one of our greatest needs and challenges. Additionally, the measurement of surface fluxes under extreme wind conditions are complicated by additional considerations such as an increasing “pressure stress” term reported in the LES study by Hara and Sullivan (2015). However, a major challenge for air-sea interaction research is to observe momentum, heat and mass exchange within the wavy boundary layer. The observational challenge is to minimize these issues through the use of innovative platforms and new sensors specifically designed for the near-surface environment.

522

523 ***2.1.3 In situ platforms for observing fluxes***

524 Historically, ships have been the primary platform for marine surface observations over the open
 525 ocean. Prior to 2000, nearly all direct covariance flux observations that have gone into developing the
 526 state of the art bulk flux algorithms were from ship-based observations (e.g., Fujitani 1981, 1985;
 527 Donelan et al., 1997; Fairall et al., 1997); notable exceptions being fluxes measured from the R/P
 528 FLIP; (Fisher and Spiess, 1963) and the Air-Sea Interaction Spar (ASIS, Gruber et al., 2000; Drennan
 529 et al., 2003, 2005). Care was taken in the development of these algorithms to account for issues
 530 associated with making surface marine observations from ships. For example, the large profile of the
 531 ship can cause flow distortion so that wind measured on the deck is not characteristic of the ambient
 532 wind (Yelland et al., 1998). Likewise, micro-climates on the ship decks can affect air temperature
 533 (Berry et al., 2004), humidity, and even barometric pressure measurements. Ideally, ship-based
 534 measurements are made on a well-exposed mast, forward of any obstructions.

535 The flow distortion in the measured mean winds can then be accounted for using empirically,
 536 modelled and/or wind tunnel derived corrections. Limiting relative wind directions and using
 537 aspirated radiation shields (or using naturally aspirated radiation shield when the relative winds are
 538 above some limit) reduce the errors due to heat island effects (i.e., ship micro-climate). The motion
 539 of the ship can also affect the surface turbulence measurements (e.g., Landwehr et al., 2015). In
 540 particular, wind and ocean currents must be transformed into Earth coordinates using high quality
 541 navigation data. In the past few years, the quality of inertial motion sensors has increased
 542 significantly, making it possible to now do motion correction routinely at 20 Hz resolution. Such
 543 technology, however, is not always available and even when available, as for example for Voluntary
 544 Observing Ships, motion correction is not always applied. For further discussion on best practices for
 545 surface marine data, see Bradley and Fairall (2006), which can be found in the Ocean Best Practice
 546 repository website for GO-SHIP measurements:
 547 <https://www.oceanbestpractices.net/handle/11329/386>.

548 Many of these “field errors” are minimized in measurements taken from moored surface buoys.
 549 Progress has been made in both developing sensors suitable for unattended deployment at sea on
 550 surface buoys and in quantifying their uncertainties. As a consequence, in moderate conditions an
 551 accuracy of 8 W m^{-2} in net heat flux has been achieved over hours to days and longer (Tables 1, 2),
 552 and further improvements are possible. In wind speeds below $\sim 3 \text{ m s}^{-1}$ active ventilation is needed of
 553 air temperature and humidity sensors and radiometers. New generation humidity sensors offering
 554 better stability and improved accuracy should be phased in. Platform tilts should be monitored as
 555 mean tilt is a source of error for incoming shortwave and longwave radiation observations. New

556 sensors are being developed that can distinguish diffuse radiation, allowing the computation of the
557 direct solar radiation component and its correction for effective changes in zenith angle associated
558 with platform motion.

559 Researchers have recently begun collecting year-long time series of direct covariance flux
560 measurements of momentum, heat and mass fluxes from surface moorings (Weller et al., 2012;
561 Bigorre et al., 2013; Farrar et al., 2015). The instrumentation on these moorings experiences less flow
562 distortion than ships and measures a wider variety of conditions given their longer deployments. For
563 example, fluxes were measured on a 3-m discus buoy for 15 months during the NSF CLIMODE field
564 program. The buoy experienced wind conditions spanning 0 - 23 m s⁻¹ over a wide range of stability
565 and surface wave conditions. The fluxes measured under these conditions were used to develop the
566 COARE 3.5 algorithm (Edson et al., 2013).

567 Similar flux packages have been deployed as part of NSF's Ocean Observatories Initiative (OOI),
568 which have been measuring motion-corrected winds for over five years, which will enable direct
569 stress and buoyancy flux measurements. Recently, fast response hygrometers were used in the NASA
570 SPURS programs (Farrar et al., 2015) to directly measure the latent heat flux. Similar work is
571 underway to develop buoy CO₂ flux systems by drying the sample. Flux systems now exist that can
572 compute and telemeter fluxes in near real-time to shore. In general, deployment duration on buoys is
573 limited by battery power, although some sensors are subject to biofouling and other issues that affect
574 the calibrations. Surface buoys are also exposed to weather, vandalism, waves, and sea birds.
575 Redundant installation of meteorological sensors is often necessary to avoid data gaps due to sensor
576 failures. This is particularly important for flux calculations since failure of any one of the primary
577 state variables will result in a data gap in the air-sea flux. Even with these precautions, however,
578 surface moorings must be refreshed at 12 - 18 month intervals, requiring a ship to transit to these
579 distant locations and adding to their expense. On the other hand, these mooring cruises provide an
580 opportunity to do repeat sections to key locations in the global climate system.

581 Computational fluid dynamic flow studies of the buoy tower and sensors are recommended to
582 identify errors due to flow distortion and guide improved sensor placement and tower design.
583 Protection from marine birds is recommended. In freezing conditions, heated sensors are required to
584 prevent ice buildup; and heating of the buoy tower maybe required to prevent ice buildup leading to
585 tipping or inversion of the surface buoy. Of course, adding heating and ventilation as well as
586 additional sensors to measure the fluxes directly requires increased battery payloads. This has been
587 done successfully using isolated battery packs to deliver power on a duty cycle. The buoys of the
588 OOI provide continuous power using additional sources that include solar panels and wind generators
589 with rechargeable storage batteries.

590 The success of buoy-based systems has led to the development and use of a wide variety of platforms
591 for observing air-sea interactions, including Autonomous Surface Vehicles (ASVs), surface drifters
592 and spar buoys (Figure 3). ASVs generally have propulsion powered by either waves (e.g., Wave
593 Glider) or wind (e.g., Saildrone, Sailbuoy), and have electronics powered by solar energy and/or
594 batteries. ASVs navigation can be controlled by setting corridor width and waypoints via satellite
595 communication system (e.g., Iridium). With speeds of up to 2.5 knots for wave-propulsion ASV and
596 7 knots for wind-propulsion ASV (depending upon wind and ocean conditions), and endurances of 6
597 months to a year, ASVs can cover thousands of nautical miles. This gives ASVs the capability to
598 either sample in a station-keeping mode, like moored buoys, to create a fixed time series, or in repeat
599 section-mode, or adaptive sampling mode, to do surveys like a research vessel. Recent examples
600 include sampling through hurricanes/typhoons (Lenain and Melville, 2014; Mitarai and McWilliams,

601 2016) and in the harsh Southern Ocean (Monteiro et al., 2015; Schmidt et al., 2017; Thomson and
602 Girton, 2017).

603 Nearly all components for calculating bulk EOV/ECV fluxes have been measured from ASVs,
604 including wind speed and direction, air-temperature, humidity, solar and longwave radiation, bulk
605 temperature, skin SST, and surface currents, although some of these measurements are less mature
606 than others. While ASVs tend to have minimal flow distortion, their platform motion (pitch, roll,
607 heading) must be removed when transforming their measurements into Earth coordinates. Improved
608 Global Positioning Systems (GPS) enable corrections for platform motions at better than 10 Hz. With
609 sonic wind sensors measuring 3-dimension winds at 10 Hz or faster (particularly at high winds near
610 the surface), field tests are underway to determine whether these platforms can be used to measure
611 covariance flux wind stress directly in addition to the mean wind. The low height of sensors making
612 atmospheric measurements on some of the ASVs remains a technical issue. The community also does
613 not have a good handle on the effects of wave shadowing or distortion on the atmospheric boundary
614 layer and its impact for example on the measured wind field (Schmidt et al., 2017) and further efforts
615 are required to assess and address this. Quantification of the accuracy for measurements associated
616 with air-sea heat and momentum fluxes are continuing.

617 ASV technology is new and currently at a pilot Technical Readiness Level (TRL) of 4 (“Trial”) - 5
618 (“Verification”) (Lindstrom et al., 2012). Before it can be expanded to a global array, the TRL needs
619 to be increased to a mature TRL of 9 (“Sustained”). For this, all sensors and systems need to be
620 validated against known standards under a wide range of field conditions on a routine basis. The
621 platforms themselves must be understood with respect to flow distortion, height of the various
622 instruments, and other complicating factors. Navigation needs to be automated in ways that maintain
623 safety at sea, and enables coordinated work with other observational platforms, such as moorings,
624 ships, and gliders (see Swart et al., this issue). Adaptive sampling of atmospheric (e.g.,
625 storms/hurricanes) or ocean (e.g., fronts and eddies) features require automatic identification and
626 tracking by ASV. Such capability would enable optimal exploration of complex atmosphere-oceanic
627 environments. Likewise, onboard data processing needs to be developed and tested, and sensor
628 system, data, and metadata must be standardized. Finally, the ASV community must agree to
629 common data delivery, archiving and best practice. An ASV governing body could help develop
630 these standards and create an ASV network.

631 Drifting or Lagrangian platforms such as the ASIS (Graber et al., 2000) have been used to
632 successfully measure the surface fluxes in field campaigns for decades. Drifting spar buoys generally
633 require less motion correction, experience less flow-distortion and place sensors above the difficult-
634 to-resolve processes within the wave-boundary layer (Hara and Sullivan, 2015); all of which results
635 in accurate direct flux estimates (Edson et al., 2013; Drennan et al., 2014). Another advantage of a
636 Lagrangian measurement of the air-sea fluxes in combination with oceanic temperature and salinity is
637 that, to the extent the drifter follows the mean mixed layer currents, an ocean heat budget assessment
638 can be simplified by reducing the advective flux divergence contribution to the budget (e.g.,
639 Silverthorne and Toole, 2013). Thus the surface fluxes measured by a drifter can be more directly
640 constrained by changes in the upper ocean heat or salt content, and more directly compared to one-
641 dimensional ocean models to evaluate the effects of surface forcing on the upper ocean (e.g., du
642 Penhoat et al., 2002). Low-profile Lagrangian surface drifters provide reliable measurements of
643 surface currents and waves over a wide range of conditions (e.g., Herbers et al., 2012). Recent
644 advances in these platforms have included the ability to measure EOVs and subsurface turbulence
645 with, e.g., SWIFT drifters (Thomson, 2012). Drifting versions of the traditional surface mooring are
646 being developed at several institutions. These “minibuoys” provide flux measurements at

647 significantly lower cost for field programs and could also be used to significantly augment
 648 conventional operational networks such as NDBC and TAO. The community should be encouraged
 649 to continue its efforts to design innovative platforms and flux systems while observing and
 650 developing best practices that include assessment against accepted standards.

651 2.1.4 OceanSITES reference time series

652 The accuracy of fluxes from moorings approaches and in some cases exceeds that required for
 653 monitoring many of the ocean air-sea interaction phenomena (Figure 2). Moorings thus can provide
 654 “reference time series” for tuning satellite measurements and assessing uncertainties in satellite and
 655 NWP fields. The purpose of the OceanSITES network (<http://www.oceansites.org>) is to collect,
 656 deliver and promote the use of high-quality multi-disciplinary data from long-term, high-frequency
 657 observations at fixed locations in the open ocean. These long time-series help to distinguish
 658 variations in EOVS due to temporal variability from that due to spatial variability. The large set of
 659 co-located EOVs at these sites (e.g., surface heat fluxes, ocean wind stress, subsurface temperature,
 660 salinity, velocity, surface mixed layer depth,...), allow many terms in the heat, momentum and salt
 661 equations to be evaluated and thus processes responsible for variability to be identified. Such
 662 analyses are critical for identifying causes of biases in NWP reanalyses and ultimately improving the
 663 model physics.

664 The OceanSITES network comprises moorings funded by individual principal investigators from
 665 oceanographic agencies in many different nations. Most sites were initiated through research process
 666 studies. For example, the Stratus mooring at 20°S 85°W, was initiated during a cloud feedbacks study
 667 (Mechoso et al., 2014; Weller, 2015), while the Kuroshio Extension Observatory (KEO) was initiated
 668 during a field study of western boundary current physics (Cronin et al., 2013). Station Papa, a site of
 669 an ocean weather ship from 1940 to 1981 in the NE Pacific subpolar gyre, has been at the center of
 670 many oceanographic process studies (Freeland, 2007; Cronin et al., 2015). The NOAA surface
 671 mooring there was initiated during a process study of the carbon cycle. The WHOI Hawaii Ocean
 672 Timeseries (WHOT) mooring was initiated as an oceanic sentinel sister site to the Moana Loa
 673 “Keeling Curve”. Monterey Bay Aquarium Research Institute (MBARI) maintains a station in the
 674 California Current system. Its primary purpose is for monitoring and understanding the ecosystem
 675 productivity and biogeochemical cycling in this upwelling zone. The OOI Irminger Sea station is part
 676 of the Overturning in the Subpolar North Atlantic Program (OSNAP). The Southern Ocean Flux
 677 Station (SOFS) south of Tasmania monitors the ventilation and mode water formation in the
 678 Subantarctic Zone (Schulz et al. 2012). SOFS and the OOI Southern Ocean (50°S, 90°W) site west of
 679 Patagonia are the only two stations in the Southern Ocean. Both are subject to storms, waves, and
 680 strong currents. The Tropical Atmosphere and Ocean (TAO) mooring array in the Pacific was
 681 initiated to better understand, monitor and predict ENSO (McPhaden et al., 1998; Cronin et al.,
 682 2006), while the tropical array in the Atlantic was designed to monitor and predict both ENSO-like
 683 and meridional modes and the Indian Ocean tropical array was designed to also monitor monsoon
 684 variability (McPhaden et al., 2009). The commonality of these long time series sites is that they all
 685 are publicly available through the OceanSITES global data assembly center, in a common data
 686 format. Figure 4 shows a comparison of a satellite-based latent and sensible heat fluxes and
 687 OceanSITES moorings. Not all these moorings carry radiation sensors and therefore only a subset of
 688 these OceanSITES moorings monitor net surface heat flux.

689 The long time series provided by the sustained surface moorings of OceanSITES have proven to be
 690 of high value, and continuation of the sustained observing sites is recommended. Merged, quality-
 691 controlled time series are produced at a number of such sites and have been sought after by the
 692 modelling community, by the remote sensing community (Pinker et al., 2018), and by those

evaluating new hybrid flux products (Valdivieso et al., 2017). Some of the time series are just now entering a third decade of observing, and these time series are capturing accurate records of decadal variability as well as of trends. Testing whether or not models and flux products replicate the broad range of time scales in the fluxes, out to decadal and beyond, is critical and requires sustained surface flux time series of high quality. Further, detection of long-term trends and separation of trends from decadal and multidecadal variability also requires ongoing long time series. These sustained time series sites also become foci for process studies that will improve understanding of air-sea interaction and fluxes and support further improvement of models.

Within the global ocean observing system, data from OceanSITES reference stations moorings are particularly important for validating gridded products of fluxes as they provide long records of high-quality flux EOV and ECV at high temporal resolution, co-located with other ancillary EOVs such as the surface ocean mixed layer. In this way, the sources of the biases can sometimes be determined, leading to improvements. The suite of sensors from OceanSITES flux moorings should include not only all flux EOV/ECV, but also, if possible, direct covariance flux estimates as well, although this may require technological development for the platforms. Likewise, sea state EOVs are being tested as flux EOVs and therefore should be included if possible. In addition, it is strongly encouraged to obtain additional environmental parameters which could help represent atmospheric and oceanic conditions that may affect the air-sea exchanges and their impacts. For example, Global Navigation Satellite System (GNSS) receiver, could provide precipitable water vapor, which has been shown to improve weather forecasts (Li et al., 2015).

Current EOV/ECV observations all suffer from different drawbacks. Comparison of point measurements from *in situ* instruments to satellite measurements, which inherently represent an average over some spatial footprint that is typically kilometers or more in extent, is made difficult by the differences in spatial and temporal sampling. These differences, caused by spatial variability on scales smaller than the satellite footprint, can be compensated somewhat by temporal averaging of the *in situ* data to effectively attenuate the small-scale variability (e.g., May and Bourassa, 2011; Lin et al., 2015), but the difference in time-space averaging in different observational approaches remains a fundamental difficulty. The *in situ* moored buoy data is accurate and has high temporal resolution, often for a long record, but these point measurements tend to be too sparsely distributed for mapping spatial patterns and understanding teleconnections. The moored buoys tend to be located along coastlines where they are easier to maintain, and in the three main tropical arrays. Furthermore, while the surface moorings that contribute to OceanSITES and coastal arrays and to research endeavors provide many flux EOV and ECV, few measure all. In particular, only a small subset of these moorings measure solar radiation and not all of these sites measure downward longwave radiation. Likewise, surface current observations are available at only a small subset of surface mooring sites. There are also large gaps in the center of ocean basins and at high latitudes, especially in the Southern Hemisphere (see Swart et al., this issue). There are currently only 22 operating sites in this global network that measure net surface heat flux, with only 7 of those being in the Southern Hemisphere. This drastically undersamples important ocean-atmospheric regimes that are known areas of high error for flux analyses. These long, high-quality time series are critical data for satellite algorithm developers, for model testing and development, and for analyzing critical processes in the climate system. These large gaps in coverage reduce the efficacy of the observation for the research and weather applications discussed in section 1.

736

737 2.2 Current capabilities for remotely sensed flux EOV/ECV measurements

The current capabilities for remotely sensed flux EOV/ECV are summarized in Table 3 and Figure 5. In particular, typical uncertainty estimates for the highest resolution swath products as well as high resolution gridded products. These uncertainty estimates are presented along with their contribution to uncertainty in the net surface heat flux, estimated by linearizing Equation (1.1) with respect to the EOV/ECV following Cronin et al. (2014). It should be noted that these uncertainties are based upon comparisons to buoys, which are primarily located in the tropics. Table 3 also describes the typical spatial and temporal resolution, and where technology developments are necessary. Figure 5 shows the status of the constellation for each EOV/ECV over the next decade, and actions needed for improvement. The status of each system is described briefly here.

The ocean surface roughness measured by satellite sensors is normally transformed into an ocean wind speed at 10 m height using algorithms developed through comparisons with ocean buoys and NWP products (Hirahara et al., 2014; Meissner et al., 2014; Meissner and Wentz, 2012; Shibata, 2012). In reality, the ocean surface roughness is related to the air-sea velocity difference, which is actually the variable of most interest for flux calculations. The measurement of ocean surface roughness from scatterometers (e.g., ASCAT, QuikSCAT, RapidSCAT) and passive microwave (MW) radiometers (e.g., SSMI, SSMI/S, WindSAT, AMSR-E, AMSR2) is already at a spatial resolution and accuracy sufficient for most global flux estimates. At NDBC, TAO, and PIRATA buoys, monthly mean satellite wind speeds are found to have average biases of 0.3 m s^{-1} and RMS of 0.73 and 0.81 m s^{-1} (QuikSCAT and SSMI, respectively) (Wallcraft et al., 2009). RMS is a bit larger for the daily mean wind speed; RMS of 1.25 m s^{-1} at TAO buoy is reported (Hirahara et al., 2014). It is even larger in the Kuroshio Extension region; RMS is 1.6 m s^{-1} at KEO buoy for AMSR2 (Tomita et al., 2015).

The recent generation of satellite SST sensors (e.g., VIIRS, AATSR and its successor, SLSTR) are close to meeting the global uncertainty of 0.3 K for surface skin temperature measurements, but the uncertainty has regional non-random characteristics that may not always meet the uncertainty requirements (Petrenko et al., 2014). There have been efforts to generate a stable SST record (e.g., ESA Climate Change Initiative for SST, NOAA Pathfinder AVHRR, MODIS - VIIRS). In regions with persistent, seasonal cloud cover, observations are simply not possible from IR instruments, which hinders the accuracy of daily and monthly SST analyses (Liu and Minnett, 2016). Other sources of error, such as water vapor and atmospheric aerosols have regional and temporal characteristics that will impact the uncertainty (Luo et al., 2018). Passive microwave SSTs approximate to the sub-skin value, but with simultaneous observation of wind speeds, and further research into transformation of these observations into a skin value, they can provide essential observations in regions where the IR observations are simply not available due to cloud cover (see section 2.2.1). Donlon et al. (2002) found the skin to subskin difference asymptotes to a value of -0.14 K for wind speeds above approximately 6 m s^{-1} . Since subsurface temperature measurements from buoys are widely used in IR atmospheric correction algorithm development and validation, an offset of -0.17 K is used as an estimate of the global thermal skin effect, so the subsurface temperatures approximate to a skin SST (Kilpatrick et al., 2015).

Near-surface air temperature is an exceptionally difficult observation from satellite measurements, as existing instrumentation cannot adequately resolve the planetary boundary layer, which has thicknesses varying from $\sim 500 \text{ m}$ to 3 km over the ocean (von Engeln and Teixeria, 2013). This observable is currently estimated using atmospheric sounders and hyperspectral sensors, both of which have drawbacks. The sounders have higher sensitivity to the upper, rather than lower, atmospheric temperatures and have low vertical resolution, making the measurement of near surface temperature exceptionally challenging. The hyperspectral instruments such as AIRS and IASI, have

784 high spectral resolution and offer better vertical resolution, but still suffer from the fundamental
 785 physical problem that the vertical resolution of derived profiles is limited to ~1 km. The use of
 786 passive MW imagers to determine near-surface air temperature and humidity has been undertaken
 787 with some success, if a first-guess SST is used, with small (< 0.1 °C) bias and roughly 1.5 °C RMS
 788 (Roberts et al., 2010; Clayson and Brown, 2016).

789 Near-surface air humidity is very difficult to infer accurately from satellite radiometers, for the same
 790 reasons as for near-surface air temperature. For both temperature and humidity, the weighting
 791 functions used for retrievals are dependent on the temperature and humidity profiles and,
 792 consequently, cannot be fixed for given wavelengths. Thus, there is a risk that the near-surface
 793 variables are artificially correlated with the sea-surface temperature and the state of the atmosphere,
 794 and distinguishing the true physical correlations from those that are artifacts of the measurement is
 795 difficult. In addition, the retrieval algorithms for near-surface temperature and humidity are
 796 commonly trained with *in situ* buoy and/or ship measurements. The relationship between satellite
 797 measurements and near-surface variables is strongly regime dependent, displaying a step-like
 798 transition (or separation) from the warm/humid regime to the cold/dry regime (Yu and Jin, 2018).
 799 The evidence suggests that the skill of the retrieval algorithm is highly dependent of the vertical
 800 distribution of water vapor. Current remote-sensing algorithms to derive near-surface humidity using
 801 a satellite MW radiometer show RMS disagreements of ~1.0 g kg⁻¹ with smaller positive bias in mid-
 802 latitudes (Tomita et al., 2018). A recent regime-dependent approach that treats the warm/humid and
 803 cold/dry regimes separately shows noted improvement with RMS of 0.8 g kg⁻¹ for air specific
 804 humidity and 0.5°C for air temperature (Yu and Jin, 2018).

805 As discussed in section 1.2.3, surface radiative fluxes are computed using radiative transfer models
 806 with input provided by cloud properties retrieved from satellites combined with temperature and
 807 humidity profiles. Comparisons of *in situ* surface observations and satellite-derived irradiances are
 808 used to estimate the uncertainty in satellite-derived irradiances; there are however only a limited
 809 number of radiation measurements over the global ocean and most of these are in the tropics.
 810 Comparisons reported by Kato et al. (2018) show that surface monthly mean downward fluxes agree
 811 with observations to within a mean difference (RMS) of 5 (11) W m⁻² respectively for shortwave, and
 812 2 (5) W m⁻² for longwave, when the differences are averaged over 46 ocean sites. Rutan et al. (2015)
 813 using CERES Edition 3 3-hourly products found an RMS of 55 and 20 W m⁻² for SW↓ and LW↓
 814 respectively. These root-mean-square differences between observed and satellite-derived 3-hourly
 815 and monthly mean irradiances are used for the uncertainty shown in Table 3. These are within the
 816 reported monthly averaged uncertainty of observed radiative fluxes at buoys of ~5 W m⁻² (Colbo and
 817 Weller, 2009). Comparison uncertainties are influenced by atmospheric, cloud and aerosol properties
 818 as well as temporal and spatial sampling issues. Ambient conditions, such as aerosol deposition, have
 819 also been shown to degrade buoy radiative flux measurements as well (Foltz et al., 2013). Although
 820 satellite derived surface radiative fluxes agree with observed radiative fluxes at buoys to within the
 821 uncertainty, most buoys are located in the tropics. To evaluate satellite derived radiative fluxes in a
 822 wide range of atmospheric conditions, observations in mid- and high-latitude regions are needed.

823 2.2.1 Systematic uncertainties near fronts and regions of persistent clouds

824 Because persistent clouds can form at fronts, IR satellite SST observations (e.g. AVHRR, MODIS,
 825 VIIRS...) can be spatially patchy due to contamination by clouds. Conversely, IR data cloud
 826 screening algorithms can also mischaracterize actual IR-observed ocean SST variability near fronts
 827 as being cloud (Kilpatrick et al. 2019). A separate issue near fronts stems from the fact that the 25-50
 828 km spatial footprint of microwave satellite SST retrievals often exceeds the frontal scale.
 829 Furthermore, these larger footprints and antenna side-lobes can allow land contamination to impact

SST front detection in coastal regions. At present, many mapping products interpolate through these patches (e.g., Reynolds et al., 2013), leading to western boundary current fronts that are too smooth and that do not capture the mesoscale variability associated with the meandering of these fronts. Because the atmospheric response depends upon the sharpness of the SST gradient (Chelton et al., 2004; Minobe et al., 2010; Parfitt et al., 2016), this bias can result in a cascade of errors. Even multi-satellite merged data are unlikely to eliminate the gaps in surface variables completely in part because of land contamination in coastal microwave-based measurements, although a proposed higher resolution sensor could mitigate this problem (e.g. Rodriguez et al., this collection).

A strategy must be developed for handling patchy data in frontal and coastal regions, using alternative data sources. While drifters, ASVs and underway ship measurements may be able to fill these gaps at times, they are likely to be too sparse both in time and space to fill all gaps. Repeat sections from these platforms, however, may provide structure functions for sharp fronts, which when combined with information about the location of the front from altimeter and tidal data, could then help fill the gaps in the patchy data with properly located sharp fronts in flux EOV and ECVs fields. Ultimately, regional atmospheric modelling, preferably with non-hydrostatic model settings and high-resolution NWP products must be used to fill in remaining patches in data with dynamically consistent fields.

2.2.2 Systematic uncertainties due to inadequate sampling of diurnal variability and episodic events

Satellite instruments can provide global or near-global coverage, but the spatial coverage comes at the cost of reduced temporal resolution. Many of the satellites used for estimating surface fluxes are in sun-synchronous polar orbits. Polar orbits have the virtue of providing near global coverage, and sun-synchronous orbits have significant engineering advantages, as satellite observations are made within a narrow range of local times so that solar angles and sun glint are relatively consistent at all times. For some variables, such as SST, geostationary satellites are also useful, with the advantage of providing higher temporal sampling rates that can resolve the diurnal cycle of SST. SST can vary by more than 2-4 K over the course of a day in regions of high solar insolation and low winds. Resolving only nighttime SST can lead to biases of up to 5-10 W m⁻² in the long-term mean heat fluxes (Clayson and Bogdanoff, 2013).

Resolving the diurnal cycle is particularly important since the diurnal cycle in solar radiation leads to an afternoon near-surface stratification that can trap surface forcing into a thin layer. As a consequence, rain-puddles formed during the daytime are fresher than ones formed at nighttime (Cronin and McPhaden, 1999). Likewise, “diurnal jets” can form, with anomalous wind-forced surface currents that are stronger in the afternoon than at nighttime (Cronin and Kessler, 2009, their Figure 5). The afternoon near-surface stratification also traps surface heat fluxes, making them more effective at causing SST change than at nighttime when the mixed layer depth is deeper. The diurnally varying mixed layer depth, in this way, causes rectification of diurnal variability into longer timescales (Bernie et al., 2005).

Satellite and NWP/reanalyses fluxes may also be biased due to poor representation of short-term extreme flux events associated with very strong winds and strong temperature and humidity gradients near the surface. In satellite-based fluxes these biases are likely due to poor sampling while in NWP and reanalyses they also might be associated with inability of atmospheric models to adequately simulate such conditions. Bentamy et al. (2017) using probability density function approach (Gulev and Belyaev, 2012) demonstrated that extreme fluxes derived from satellite products may deviate

874 from flux extremes estimated from buoy measurements by tens of Wm-2, even if the mean flux
 875 estimates are comparable.

876 Except at high latitudes, a single polar orbiting satellite can provide a maximum of two
 877 measurements per day (e.g., at 10:30 am and 10:30 pm), which is inadequate for resolving
 878 atmospheric synoptic variability or for resolving the amplitude and phase of the diurnal cycle. The
 879 diurnal cycle can be resolved by either placing several satellites in different sun-synchronous orbit
 880 planes to sample several discrete local times or by a single satellite in a lower inclination orbit. In the
 881 latter case, the satellite will precess through the diurnal cycle for any location on the ground over a
 882 period of time (days to months) that is related to the orbit inclination. Placing several satellite in sun-
 883 synchronous orbits, while more costly, has the benefit of sampling the diurnal cycle daily at discrete
 884 local times and reduces the overall re-visit time for resolving rapidly-evolving storms and short-lived
 885 extreme events.

886

887 2.3 Current capabilities for gridded flux products

888 To create the global flux products, the flux EOFs and ECVs must be observed or estimated with
 889 sufficient resolution and coverage to map their fields, or to constrain NWP model solutions and
 890 reanalyses to produce realistic flux fields. For flux products that extend back to the early-mid
 891 twentieth century, these gridded products based upon observations and NWP rely exclusively upon *in*
 892 *situ* data, primarily from underway ships. In the past decades, a satellite constellation has been
 893 building that can provide several of the gridded EOFs necessary for creating the flux products.
 894 However, because satellites are at present unable to provide some EOFs (e.g. surface air temperature
 895 and humidity) with acceptable accuracy, for some “blended” products such as the OAFlux product
 896 (Yu and Weller, 2007), air temperature and humidity are instead based on bias-adjusted NWP
 897 outputs, while other flux EOFs and ECVs are derived from satellite data. Satellite measurements
 898 appear to provide sufficient signal-to-noise ratios to produce high-quality stress estimates; however,
 899 direct *in situ* measurements of stress are too sparse to provide adequate calibration. The common
 900 practice is to derive winds from satellite backscatter measurements by utilizing *in situ* wind
 901 measurements and compute wind stress from bulk flux parameterization.

902 Even NWP and blended flux products, however, have large biases and uncertainties (Cronin et al.,
 903 2006; Valdivieso et al., 2017; Bentamy et al., 2017; Tomita et al., 2019; Yu, 2019). Mean fields from
 904 12 products show standard deviations of up to 30 W m^{-2} for net surface heat flux and $5 \times 10^{-2} \text{ N m}^{-2}$
 905 for wind stress (Figure 1c-d). It should be noted though that agreement between the different
 906 products does not mean that there are no biases; it may mean that all products are biased in the same
 907 way. In this case, the standard deviation around the multiproduct mean is not an appropriate estimate
 908 of the uncertainty. Moreover, the standard deviation could be overestimated due to outlying products.
 909 Thus, independent reference data are required to determine the accuracy of these products.

910 For the global average, ocean heat content estimates show the net surface heat flux into the ocean to
 911 be less than 1 W m^{-2} (e.g., Roemmich et al., 2015); for most products, the global average of the net
 912 air-sea heat flux is up to an order of magnitude larger than this (Figure 6a; Table 4). Comparisons of
 913 the state variables against moored reference station data show that a substantial part of this mean bias
 914 is due to deficiencies in the bulk algorithm used by the NWP (Zhang et al., 2016; Jiang et al., 2005).
 915 Bias can also be associated with the radiative heat flux components (Figure 6b), highlighting the need
 916 to improve satellite radiative observations and the presence of clouds in NWP. In order to understand

917 the regional distribution of these errors and diagnose their causes, in situ reference stations are
 918 needed (Figure 4).

919 To improve NWP fluxes, marine boundary layer physics in NWP must be improved, including their
 920 algorithms for computing air-sea fluxes. In addition, more *in situ* and remotely-sensed data with
 921 higher accuracy are needed to constrain the NWP. More accurate satellite-based moisture and
 922 temperature profiles and surface data would greatly improve remotely-sensed estimates of surface
 923 radiation and latent and sensible heat fluxes, and if assimilated into NWP models, would likely lead
 924 to improved representation of cloud formation processes and thereby improved representation of the
 925 state variables and surface radiative and turbulent fluxes from these NWP models.

926

927 **3 Aspirational Sampling Requirements and Target Uncertainties**

928 Air-sea fluxes are challenging to observe because high-frequency variability and gustiness rectifies
 929 into the longer time scales. To adequately represent the annual cycle of heat fluxes, synoptic
 930 variability associated with storms must be captured. Subdiurnal resolution is required to adequately
 931 represent fluxes associated with fast-moving storms or in regions with a large diurnal cycle in SST.
 932 Fast moving atmospheric synoptic transients are associated with surface flux extremes (e.g., Tilinina
 933 et al., 2018), which can only be resolved in high resolution data. A gridded air-sea flux product that
 934 has 25 km or better spatial resolution and at least 3-hourly temporal resolution with a random
 935 uncertainty of 15 W m^{-2} and a bias of less than 5 W m^{-2} would be able to capture most of the air-sea
 936 interaction phenomena shown in Figure 2. The corresponding wind stress product should have a
 937 random uncertainty of $\pm 0.01 \text{ N m}^{-2}$ (or a 5% noise-to-signal ratio, whichever is larger) and a bias of
 938 $< 0.005 \text{ N m}^{-2}$. It is important though to realize that the native resolution of the source observations
 939 for this gridded product must be at least 2-4 times better -- at least 10 km and hourly. While this
 940 represents an improved accuracy at this resolution for wind stress, for the heat flux product,
 941 achieving this accuracy would represent a breakthrough advancement. Table 5 summarizes the
 942 sampling requirements for each flux EOV/ECV needed to meet this aspirational target. Because SST
 943 is the primary ocean EOV that drives the air-sea flux, and can be controlled by ocean frontogenesis
 944 processes, SST must have the highest spatial resolution of all EOV/ECV. We set an aspirational
 945 target of 1 km. This aspirational target, even now, is partially met for many parts of the global ocean.

946

947 **4 Opportunities for improved fluxes in the global ice-free ocean**

948 For global ice-free ocean estimates of turbulent heat and momentum fluxes, it is necessary to
 949 measure the flux EOVs and ECVs with sufficient accuracy, coverage and resolution to meet the
 950 targeted uncertainty and stability. As described in section 2, the primary state variables for computing
 951 turbulent air-sea fluxes of heat and momentum include near surface air temperature, ocean skin SST,
 952 near-surface humidity, and the surface wind relative to the ocean surface currents. At present,
 953 humidity and air-temperature ECVs do not meet the requirements needed for global flux estimation
 954 (Tables 3 and 5; Figure 7). Our two major recommendations, described below, and our roadmap to
 955 flux improvement described in section 5, will address these deficiencies and others, enabling
 956 adequate sampling for all primary flux EOV/ECV by 2030.

957 **4.1 Space-based sensor for near surface moisture and air-temperature retrievals**

958 A future remote-sensing measurement system designed for the boundary layer can address many of
959 the issues that bedevil the present system. In particular, as described in section 2.2, existing remote
960 sensing satellites are able to measure near surface wind speed and surface skin temperature with
961 sufficient accuracy using either microwave or IR instruments, although further algorithm
962 development is needed since these measurements are often tuned to bulk (rather than skin) SST and
963 wind speed (rather than wind stress). Current atmospheric sounders are able to measure vertical
964 profiles of temperature and water vapor, and these observations are the basis for deriving satellite-
965 based near-surface air temperature and humidity.

966 Three major challenges need to be addressed to improve remotely-sensed estimates of heat fluxes:
967 improvements to retrievals, improvements to time coincidence of EOVS/ECVs, and improvements to
968 algorithms. The first challenge is to improve the sensitivity and vertical resolution of microwave
969 sounders in the boundary layer. Existing microwave sounders typically only have a few channels
970 giving sensitivity at less than 10 evenly spaced levels from the surface to 20 km for temperature and
971 to 10 km for water vapor. These channels are also fixed in frequency and often introduce biases due
972 to the shift of the weighting functions (see section 2.2). This may be overcome by adding additional
973 channels, such as hyperspectral microwave sounding spectrometers at 50 and 183 GHz. Simulations
974 of a notional hyperspectral sensor with a neural network retrieval algorithm predict uncertainties of
975 0.6°C for near-surface air temperature and 7% error for near-surface specific humidity, effectively
976 doubling the accuracy of existing retrievals, for 1 km layers from the surface to 10 - 20 km altitude
977 (Boukabara and Garrett, 2011; Blackwell, 2005; Blackwell et al., 2011). Assimilation of these better-
978 resolved profiles into NWP should lead to additional improvements to the representation of near-
979 surface conditions and thus air-sea fluxes.

980 The second challenge is to improve the time coincidence of the remotely sensed flux EOV/ECV
981 measurements, which are typically made by independent systems and therefore usually not coincident
982 in time, introducing de-correlation errors when computing fluxes from merged data. Time
983 coincidence could be achieved by combining instruments on the same platform, or by using
984 instruments on separate platforms flying in formation, which would most likely require a set of small
985 satellite sensors to be cost effective. Alternatively, a passive microwave radiometer that combined
986 low-frequency window channels used to measure SST and wind speed with atmospheric temperature
987 and water vapor sounding channels would address the co-incidence issue with a single instrument.
988 Radiometer instrument technology has made rapid strides in the past several years to miniaturize and
989 lower the cost of the sensors envisioned for this constellation, coupled with equal advancements in
990 low-cost CubeSat and small satellites. The US Air Force plans to demonstrate a low-cost conical
991 microwave imager (Brown et al., 2017) and NASA has two missions to demonstrate CubeSat
992 microwave imager/sounders (Reising et al., 2016; Blackwell et al., 2018). In addition, launch costs
993 have decreased through rideshare opportunities.

994 The third challenge is to improve the retrieval algorithms for near-surface air temperature and
995 humidity. While SST and wind speed accuracies are typically better than 0.3 - 0.5°C (Gentemann,
996 2014; Kilpatrick et al., 2015) and 0.5-1.4 ms⁻¹ (Zhang et al., 2018), direct retrievals of near-surface
997 air temperature and humidity a few meters above the sea surface remains challenging. Remote
998 sensing retrievals provide average values for the lower 1 km. The relationship between this average
999 and the air temperature and specific humidity at the sea surface requires an understanding of the
1000 vertical distribution of moisture within the atmospheric boundary layer and how this varies regionally
1001 and temporally. The suggested roadmap therefore includes a holistic program to improve and tune the
1002 retrieval algorithms and our understanding of their uncertainties, which will require improved remote
1003 sensing observations and a global array of in situ observation.

1004

1005 **4.2 Globally distributed *in situ* network of flux EOV and ECV**

1006 As discussed in section 2.2, the sparsity of the *in situ* network of flux EOV/ECV observations,
 1007 particularly in large regions of the Southern Hemisphere, stands as a major obstacle to progress.
 1008 Lack of *in situ* data in these regions and other regimes lead to large uncertainties in satellite air
 1009 humidity and temperature retrievals because retrieval algorithms are not sufficiently trained to
 1010 represent various near-surface boundary conditions (Yu, 2019). In regions of low winds, where SST
 1011 can have a large diurnal cycle and wind gustiness contributes significantly to the wind variance, *in*
 1012 *situ* surface observations may capture the temporal variability of air-sea fluxes better than polar-
 1013 orbiting satellite. Likewise, *in situ* observations may be better at capturing temporal variability of fast
 1014 moving storms in the northern and southern hemisphere storm tracks. These tend to be regions with
 1015 convective rainfall, which also can contaminate satellite IR scatterometer measurements. Finally,
 1016 while satellite observations have a spatial resolution that a global *in situ* array could never meet, as
 1017 discussed in section 2.2.1, satellite can have data gaps due to persistent clouds in frontal regions
 1018 precisely where air-sea fluxes are expected to be large. ***Together, these strengths and weaknesses of***
 1019 ***remotely sensed vs. in situ observations argue for developing a global in situ flux-observing array***
 1020 ***to complement the global remote-sensing constellation.***

1021 Mazloff et al. (2018, their Table 1) provide estimates for heat and carbon flux decorrelation scales in
 1022 the Southern Ocean, sorted into low-pass and high-pass scales. The low-pass requirements need very
 1023 sparse sampling (90° by 10° ; 11 measurements), but high-pass sampling is more substantial: 156
 1024 measurements in the 70° to 35° latitude range, or roughly one measurement per 4° by 4° box. Further
 1025 work will need to be done to determine the optimal design of this regionally distributed plan. But at
 1026 its center might be pairs or clusters of flux platforms within a regular grid (e.g., 10° by 10°) box. For
 1027 reference, nodes of a 10° grid are shown in Figure 8, with 368 nodes in the global ocean. We
 1028 envision a global network of flux observing platforms made up of ASVs, drifting and moored buoys,
 1029 and R/Vs, with the exact choice of platform dependent upon conditions and scientific needs. This
 1030 large-scale network of high-resolution sampling would ideally capture frontal structures that are
 1031 critical to the generation of large exchanges of heat between the ocean and atmosphere.

1032 These flux platforms could carry other sensor suites too, such as air-sea carbon dioxide flux packages
 1033 and ocean acidification sensors. In this way, the network could be multi-functional and serve a range
 1034 of communities and stakeholders beyond those described here. In the future, as true coupled data
 1035 assimilation becomes standard for NWP, we would expect that this network of co-located surface
 1036 ocean and atmospheric *in situ* observations would be particularly valuable for assimilations.

1037 This globally distributed array should be built around an expanded OceanSITES network. At present,
 1038 the OceanSITES surface flux array is too sparse, with 22 sites that measure net surface heat flux.
 1039 Nineteen key regions needing OceanSITES time series stations are shown in Figure 8. These regions
 1040 include eleven discussed in section 2.1.3, as well as regions in the western equatorial Pacific and
 1041 western North Atlantic, and eight additional high priority regions in the Southern Hemisphere. These
 1042 regions have no OceanSITES flux reference station. As discussed in section 2.1.3, an OceanSITES
 1043 station not only monitors the air-sea fluxes, but also the local response of the ocean, atmosphere, and
 1044 ecosystem to these air - sea exchanges. Tozuka et al. (2018) have shown that the contribution of
 1045 surface heat fluxes to surface frontogenesis/frontolysis depends not just on the flux gradients, but
 1046 also on the distribution of mixed layer depth, which controls the effective heat capacity of the upper
 1047 ocean. The OceanSITES flux network provides these co-located air-sea flux, mixed layer depth

1048 observations, and other EOFs so that budget analyses can be performed to determine causes for
 1049 surface variability.

1050 In some regions, such as the tropical Pacific, the number of OceanSITES flux reference stations
 1051 could be increased simply by adding a few sensors to existing OceanSITES surface moorings. In
 1052 other regions, new mooring stations are needed. The Tropical Pacific Observing System (TPOS)-
 1053 2020 project is working to optimize flux measurements in the tropical Pacific, including the eastern
 1054 and western boundary regions (Smith et al., 2019). Likewise, the Southern Ocean Flux working
 1055 group is in the process of developing a deployment strategy to optimize the positioning of a sparse
 1056 internationally-supported array of flux moorings (Swart et al., this issue). Regional groups, like these,
 1057 have the scientific expertise and local knowledge that are critical for making these long-term stations
 1058 successful. Nevertheless, the following list of new sites are considered to be a high priority as they
 1059 are all in regions that do not at present have any flux reference station:

1060 New Flux Reference Sites for 8 Key Regions with no Flux Station at Present

- 1061 1. Tropical Western Pacific (9°N , 150°E ; equatorial region west of 165°E): Typhoon corridor,
 1062 monsoon, intraseasonal oscillations, and ENSO variability.
- 1063 2. Southern Ocean (order 60°S , any longitude): Ice-edge conditions. Southern Hemisphere storm
 1064 track.
- 1065 3. Southern Ocean (40°S - 60°S , any longitude): Southern Hemisphere storm track.
- 1066 4. Agulhas (40°S , 36°E): Intense heat loss region associated with S. Indian Ocean western
 1067 boundary current (WBC), extratropical storms, interbasin eddy heat exchanges, mixed layer depth
 1068 role in front gradient.
- 1069 5. Southeast Indian Ocean (25°S , 110°E): Strongest ocean evaporation region (globally) in trade
 1070 wind return flow, subject to “Ningaloo” mid-latitude marine heat waves. Subtropical mode water
 1071 formation site.
- 1072 6. Gulf Stream (35°N , 60°W): Intense heat loss associated with N. Atlantic WBC, eddy rich
 1073 region, tropical-extratropical cyclones and interactions, cold-air outbreaks.
- 1074 7. East Australian Current (35°S , 160°E): S. Pacific WBC, Tasman Front, tropical-extratropical
 1075 interactions.
- 1076 8. Brazil-Malvinas Confluence (42°S , 42°W): S. Atlantic WBC, eddy rich region, tropical-
 1077 extratropical interactions.

1078 These regions listed here are high priority because they at present have no OceanSITES flux
 1079 reference station in them. Our boxed regions, however, are large, covering major quadrants of each
 1080 basin. Each have multiple regimes, sometimes separated by major fronts. For many regions, such as
 1081 the tropics, multiple stations are justified. Careful array design studies by regional experts is
 1082 recommended.

1083 A subset of the long-term reference stations should be enhanced for process studies and to provide
 1084 high resolution turbulent flux and mean profiles that extend 20 to 100 m into the marine atmosphere.
 1085 These “super sites” would provide critical observations to validate and guide model physics and bulk

flux and satellite retrieval algorithm development. Such a system, with multiple levels of fast-response sensors to directly measure momentum, heat and mass exchange, could be based on fixed towers, large moored spar buoys or other floating platforms, which are being developed and used by the offshore wind industry. Remote sensing systems deployed on the platforms and from nearby moorings (e.g., Lidar buoys) could provide further characterization of the coupled boundary layer, including cloud information, boundary layer height and mixed layer depth. Other key variables to be observed at these sites could include wave information, radiative fluxes (including both upwelling and downwelling fluxes), skin SST, precipitation, high-resolution upper ocean currents, fast static pressure, and a suite of oceanic boundary measurements, among others. These supersites and their associated infrastructure would also serve as testbeds for validation of innovative platforms and systems, such as low-power sensors and remote sensing systems for deployment on buoys and mobile platforms. In addition, it is recommended that some of the ships servicing the moorings and supersites be enhanced to monitor the coupled boundary layer, and host unmanned aircraft systems for observing along-wind and cross-wind variations, obtaining data to improve albedo parameterizations, and for monitoring a wide-range of coupled boundary layer processes. The breakthroughs highlighted in Figure 7 depend not only upon improved remote sensing and expanded *in situ* observations, but also upon improved models, algorithms and parameterizations. This ambitious goal is predicated upon vigorous research fed by these coupled boundary layer observations described here.

1105

1106 5 Roadmap for improving air-sea fluxes

1107 Quantifying air-sea fluxes is very challenging as multiple co-located flux EOV/ECV must be
 1108 measured at high temporal and spatial resolution, with high accuracy. At present, the global ocean
 1109 observing system does not meet the necessary requirements (Fig. 7), mainly due to the lack of global
 1110 coverage of surface humidity and air temperature. Our two major recommendations rectify this and
 1111 other deficiencies:

1112 **Major Recommendation #1:** Create a remote-sensing retrieval system designed for accurate
 1113 boundary layer measurement of air temperature, humidity, SST, and surface stress. This would
 1114 involve a holistic approach to improve resolution of satellite retrievals, time coincidence of remotely-
 1115 sensed surface flux EOVs/ECVs, and algorithms that relate the retrievals to near-surface conditions.

1116 **Major Recommendation #2:** Create a global *in situ* array of flux observing platforms, built
 1117 around an expanded OceanSITES network of time series reference station moorings. The global array
 1118 would include ~500-1000 platforms including Autonomous Surface Vehicles, moored and drifting
 1119 buoys, and RVs, with 1-3 platforms in nominal 10° by 10° boxes. The OceanSITES network of 22
 1120 flux sites must be maintained and expanded in up to 19 key regions. In addition, the *in situ* array
 1121 should include a few super sites with enhanced observations of the coupled boundary layer.

1122 These major recommendations depend upon a number of steps taking place, as shown in the
 1123 Roadmap (Figure 9):

- 1124 • The TRL for ASV and other new flux platforms must be increased before being used to form
 1125 a large global network. These platforms must be continually evaluated against satellite and
 1126 proven technology, including RVs, flux towers with vertical extent, and OceanSITES and
 1127 OOI moorings. It is recommended that an international ASV expert group form to coordinate
 1128 ASV data stream, evaluate data, and develop best practices and standardizations.

- Array designs for the *in situ* flux network must be studied. It is likely that a flux network would have some similarities to an Argo array in being globally distributed, but also have some distinct differences due to the importance of fronts and rapid variations in flux EOV/ECV. Likewise, in contrast to Argo, adaptive sampling capabilities of ASV could allow the globally distributed array to target certain phenomena and to sample in combination with other fixed platforms. Determining the optimal array design will require both model studies and pilot field studies.
- International coordination of data management and archival must be extended to flux-related data streams, including for all underway RV observations, ASVs, drifting and other flux platforms, and for observations transmitted in near real time in support of NWP on the Global Telecommunications System (GTS).
- With the expanded *in situ* array of platforms that measure all flux EOV/ECV including direct covariance flux estimates of the turbulent fluxes, the state of the art bulk aerodynamic flux algorithm can be improved, leading to reduced uncertainties. It is critical that the bulk algorithm in NWP be improved.
- Parameterizations for transforming bulk EOV/ECV into bulk algorithm state variables must be improved. These include (but are not limited to) extrapolation of bulk sea surface state variables to the air-sea interface, and parameterizations of albedo and emissivity.
- Cross-platform and cross-product intercomparisons must take place and differences must be reconciled. Sensors across all *in situ* platforms should have laboratory calibrations traceable to international standards, and field intercomparisons to verify consistency. Identification of field errors should lead to changes in best practices. Identification of model errors should lead to recommendations for improved physics and parameterizations.

6 Conclusions

In this paper, we lay out an observational strategy for producing 3-hourly at 25-km (and an aspirational goal of hourly at 10-km) gridded heat fluxes and wind stress fields over the global, ice-free ocean that have a breakthrough improvement in accuracy for heat flux and, for these scales, an improved accuracy in wind stress. The target for the net heat flux product is 1-day random uncertainty of 15 W m^{-2} (or 5% error for each radiative component and the sum of the turbulent heat fluxes) and a bias of less than 5 W m^{-2} . For the wind stress product the target is 1-day random uncertainty of $\pm 0.01 \text{ N m}^{-2}$ (or a 5% noise-to-signal ratio, whichever is higher) and a bias of 0.005 N m^{-2} . At present the heat flux uncertainty target is met only at OceanSITES reference station moorings and research vessels that follow best practices. To meet these targets in the next decade, we make two major recommendations: (1) Create a remote-sensing measurement system designed for accurate boundary layer measurements of air temperature, humidity, SST, and surface stress; and (2) Create a complementary global *in situ* array of flux observing platforms, built around an expanded OceanSITES network of time series reference station moorings. The global array would include ~500-1000 platforms including ASV, moored and drifting buoys, and RVs, with 1-3 platforms in nominal 10° by 10° boxes. The OceanSITES network of 22 flux sites must be maintained and expanded in up to 19 key regions. The *in situ* flux array would provide globally distributed measurements and metrics for satellite algorithm development and product validation. In addition, *in situ* flux EOV and ECV observations that also include direct covariance flux observations could be used to improve “bulk aerodynamic algorithm” for computation of air-sea exchange of heat and momentum. With improved coupling of the ocean and atmosphere in NWP, and constrained by the improved moisture and air temperature profiles, these NWP are expected to have improved

1175 representation of cloud formation processes and radiative properties. Together, these will lead to a
 1176 more accurate satellite-based (and blended) flux product. This better quantification of the ocean's
 1177 influence on the atmosphere will lead to improved long-term weather forecasts, seasonal-interannual-
 1178 decadal climate predictions, and regional climate projections.

1179 7 Author Contributions

1180 MC, CG, JE and IU were first authors for abstracts that were merged into the present version. MC
 1181 wrote the first draft of the paper; CG, JE, SB, IU, EK, RW, SJ, RP, SK, CF, HT, PM, TF, SS
 1182 contributed text sections; LY, MB, PM, and MC contributed figures; all authors contributed to
 1183 manuscript revision, and read and approved the submitted version.

1184 8 Conflict of Interest Statement

1185 NOAA PMEL has had a Cooperative Research and Development Agreement (CRADA) with
 1186 Saildrone, Inc. since 2014 that covers work with Saildrone ASV by MFC. This has involved in kind
 1187 contributions from Saildrone, Inc. towards NOAA ASV missions. It is expected that this work will
 1188 benefit NOAA's mission and the entire ASV industry. CG had a contract for 6 weeks of her time
 1189 from Saildrone, Inc. The contract was to coordinate a 2-month Saildrone cruise that occurred in
 1190 Spring 2018. DV had a contract for 2 weeks of his time from Saildrone Inc. in 2018 to advise on the
 1191 data collection and processing of turbulent flux measurements using their platform.

1192 9 Funding

1193 EK was funded by the NERC CLASS Programme (NE/R015953/1). CG was funded by NASA grant
 1194 80NSSC18K0837.

1195 10 Acknowledgment

1196 Three reviewers provided insightful and detailed comments that significantly improved the
 1197 manuscript. The authors gratefully acknowledge contributions from Drs. Kentaro Ando, Tatsuya
 1198 Fukuda, Yasuhisa Ishihara and Makito Yokota (all from JAMSTEC, Japan), Dr. Aderrahim Bentamy
 1199 (IFREMER, France), Dr. Shawn Smith (FSU, USA), Dr. Scott Miller (Albany University, USA) and
 1200 Sandra Bigley (NOAA PMEL). The work benefited by discussions within the OOPC, AOPC, WRCP
 1201 Data Advisory Council (WDAC) Surface Flux Task Team, National Academy of Science Workshop
 1202 "The Future of Atmospheric Boundary Layer Observing, Understanding, and Modeling", Southern
 1203 Ocean Flux Working Group (SOFLUX), and Tropical Pacific Observing System (TPOS)-2020
 1204 Planetary Boundary Layer Task Team. This is PMEL publication 4842.

1205 11 References

1206 Andersson, A., Klepp, C., Fennig, K., Bakan, S., Grassl, H., and Schulz, J. (2011). Evaluation of
 1207 HOAPS-3 ocean surface freshwater flux components. *J. Appl. Meteor. Climatol.* 50, 379–398. doi:
 1208 10.1175/2010JAMC2341.1

1209 Andreas, E. L., Persson, P. O. G., and Hare, J. E. (2008). A bulk turbulent air-sea flux algorithm for
 1210 high-wind, spray conditions. *J. Phys. Oceanogr.* 38(7), 1581–1596. doi: 10.1175/2007JPO3813.1

1211 Andreas, E. L., Mahrt, L., and Vickers, D. (2015). An improved bulk air-sea surface flux algorithm,
 1212 including spray-mediated transfer. *Q. J. Roy. Meteor. Soc.* 141(687), 642–654. doi: 10.1002/qj.2424

- 1213 Banner, M. L., and Morison, R. P. (2010). Refined source terms in wind wave models with explicit
 1214 wave breaking forecasts. Part I: Model framework and validation against field data. *Ocean Modell.*
 1215 33, 177–189.
- 1216 Beljaars, A. C. M. (1995). The parametrization of surface fluxes in large-scale models under free
 1217 convection. *Q. J. Roy. Meteor. Soc.* 121, 255–270.
- 1218 Bentamy A., Piollé, J. F., Grouazel, A., Danielson, R., Gulev, S., Paul, F., et al. (2017). Review and
 1219 assessment of latent and sensible heat flux accuracy over the global oceans. *Remote Sens. Environ.*
 1220 201, 196–218.
- 1221 Bernie, D. J., S.J. Woolnough, J.M. Slingo, and E. Guilyardi (2005). Modeling diurnal and
 1222 intraseasonal variability of the ocean mixed layer. *J. Climate* 18, 1190–1202. doi:
 1223 10.1175/JCLI3319.1
- 1224 Berry, D. I., and Kent, E. C. (2009). A new air–sea interaction gridded dataset from ICOADS with
 1225 uncertainty estimates. *Bull. Amer. Meteor. Soc.* 90, 645–656. doi: 10.1175/2008bams2639.1
- 1226 Berry, D. I., and Kent, E. C. (2011). Air-sea fluxes from ICOADS: The construction of a new
 1227 gridded dataset with uncertainty estimates. *Int. J. Climatol.* 31(7), 987–1001. doi: 10.1002/joc.2059
- 1228 Berry, D. I., Kent, E. C., and Taylor, P. K. (2004). An analytical model of heating errors in marine air
 1229 temperatures from ships. *J. Atmos. Oceanic Technol.* 21, 1198–1215. doi: 10.1175/1520-
 1230 0426(2004)021<1198:AAMOHE>2.0.CO;2
- 1231 Bigorre, S., Weller, R. A., Lord, J., Edson, J. B., and Ware, J. D. (2013). A surface mooring for air–
 1232 sea interaction research in the Gulf Stream. Part 2: Analysis of the observations and their accuracies.
 1233 *J. Atmos. Ocean. Tech.* 30, 450–469.
- 1234 Bishop, S. P., Small, R. J., Bryan, F. O., and Tomas, R. A. (2017). Scale dependence of midlatitude
 1235 air–sea interaction. *J. Climate* 30, 8207–8221. doi: 10.1175/JCLI-D-17-0159.1
- 1236 Blackwell, W. J. (2005). A neural-network technique for the retrieval of atmospheric temperature and
 1237 moisture profiles from high spectral resolution sounding data. *IEEE Trans. Geosci. Remote Sens.* 43,
 1238 2535–2546.
- 1239 Blackwell, W. J., Bickmeier, L. J., Leslie, R. V., Pieper, M. L., Samra, J. E., Surussavadee, C., et al.
 1240 (2011). Hyperspectral microwave atmospheric sounding. *IEEE Trans. Geosci. Remote Sens.* 49, 128–
 1241 142.
- 1242 Blackwell, W. J., Braun, S., Bennartz, R., Velden, C., DeMaria, M., Atlas, R., et al. (2018). An
 1243 overview of the TROPICS NASA Earth Venture Mission. *Q. J. Roy. Meteor. Soc.* 144, 16–26.
- 1244 Blomquist, B. W., Huebert, B. J., Fairall, C. W., Bariteau, L. Edson, J. B., Hare, J. E., et al. (2014).
 1245 Advances in air–sea CO₂ flux measurement by eddy correlation. *Bound.-Layer Meteorol.* 152, 245–
 1246 276. doi: 10.1007/s10546-014-9926-2
- 1247 Bond, N. A. and Cronin, M. F. (2008). Regional weather patterns during anomalous air–sea fluxes at
 1248 the Kuroshio Extension Observatory (KEO). *J. Climate* 21, 1680–1697. doi:
 1249 10.1175/2007JCLI1797.1

- 1250 Bond, N. A., Cronin, M. F., Freeland, H., and Mantua, N. (2015). Causes and impacts of the 2014
 1251 warm anomaly in the NE Pacific. *Geophys. Res. Lett.* 42, 3414–3420.
- 1252 Boukabara, S. A., and Garret, K. (2011). Benefits of a hyperspectral microwave sensor. *Sensors* 2011
 1253 IEEE, 1881–1884. doi: 10.1109/ICSENS.2011.6127357
- 1254 Bourassa, M., Gille, S., Bitz, C., Carlson, D., Cerovecki, I., Cronin, M., et al. (2013). High-latitude
 1255 ocean and sea ice surface fluxes: Requirements and challenges for climate research. *Bull. Amer.*
 1256 *Meteor. Soc.* 94, 403–423. doi: 10.1175/BAMS-D-11-00244.1
- 1257 Bourassa, M. A., Vincent, D. G., and Wood, W. L. (1999). A flux parameterization including the
 1258 effects of capillary waves and sea state. *J. Atmos. Sci.* 56, 1123–1139.
- 1259 Bradley, F., and Fairall, C. (2006). *A Guide to Making Climate Quality Meteorological and Flux*
 1260 *Measurements at Sea, NOAA Technical Memorandum OAR PSD-311*. Boulder, CO: Earth System
 1261 Research Laboratory, Physical Sciences Division.
- 1262 Brodeau, L., Barnier, B., Gulev, S. K., and Woods, C. (2017). Climatologically significant effects of
 1263 some approximations in the bulk parameterizations of turbulent air-sea fluxes. *J. Phys. Oceanogr.* 47,
 1264 5–28. doi: 10.1175/JPO-D-16-0169.1
- 1265 Brown, S., Focardi, P., Kitayakara, A., Maiwald, F., Milligan, L., Montes, O., et al. (2017). "The
 1266 COWVR Mission: Demonstrating the capability of a new generation of small satellite weather
 1267 sensors," in *2017 IEEE Aerospace Conference*, 1–7. doi: 10.1109/AERO.2017.7943884
- 1268 Brunke, M. A., Fairall, C.W., Zeng, X., Eymard, L., and Curry, J. A. (2003). Which bulk
 1269 aerodynamic algorithms are least problematic in computing ocean surface turbulent fluxes?. *J.*
 1270 *Climate*, 16, 619–635. doi: 10.1175/1520-0442(2003)016<0619:WBAAAL>2.0.CO;2
- 1271 Buckley, M. P., and Veron, F. (2016). Structure of the airflow above surface waves. *J. Phys.*
 1272 *Oceanogr.* 46, 1377–1397.
- 1273 Bulgin, C. E., Embury, O., Corlett, G., and Merchant, C. J. (2016). Independent uncertainty estimates
 1274 for coefficient based sea surface temperature retrieval from the Along-Track Scanning Radiometer
 1275 instruments. *Remote Sens. Environ.* 178, 213–222. doi: 10.1016/j.rse.2016.02.022
- 1276 Businger, J. A., Wyngaard, J. C., Izumi, Y., and Bradley, E. F. (1971). Flux-profile relationships in
 1277 the atmospheric surface layer. *J. Atmos. Sci.* 28, 181–189. doi: 10.1175/1520-
 1278 0469(1971)028<0181:FPRITA>2.0.CO;2
- 1279 Charnock, H. (1955). Wind stress on a water surface. *Q. J. Roy. Meteor. Soc.* 81, 639–640. doi:
 1280 10.1002/qj.49708135027
- 1281 Chelton, D. B., Schlax, M. G., Freilich, M. H., and Milliff, R. F. (2004). Satellite measurements
 1282 reveal persistent small-scale features in ocean winds. *Science* 303, 978–983.
- 1283 Chuda, T., Niino, H., Yoneyama, K., Katsumata, M., Ushiyama, T. and Tsukamoto, O. (2008). A
 1284 statistical analysis of surface turbulent heat flux enhancements due to precipitating clouds observed
 1285 in the tropical Western Pacific. *J. Meteorol. Soc. Jpn.*, 86, 439–457.

- 1286 Cifuentes-Lorenzen, A., Edson, J. B., and Zappa, C. J. (2018). Air-sea interaction in the Southern
 1287 Ocean: Exploring the height of the wave boundary layer at the air-sea interface. *Bound.-Layer Meteor.*
 1288 169, 461–482. doi: 10.1007/s10546-018-0376-0
- 1289 Clayson, C. A., and Brown, J. (2016). *NOAA Climate Data Record Ocean Surface Bundle (OSB)*
 1290 *Climate Data Record (CDR) of Ocean Heat Fluxes, Version 2. Climate Algorithm Theoretical Basis*
 1291 *Document (C-ATBD)*. NOAA National Center for Environmental Information. doi:
 1292 10.7289/V59K4885.
- 1293 Clayson, C. A., and Bogdanoff, A. (2013). The effect of diurnal sea surface temperature warming on
 1294 climatological air-sea fluxes. *J. Climate* 26, 2546–2556.
- 1295 Colbo, K., and Weller, R. A. (2009). Accuracy of the IMET sensor package in the subtropics. *J.*
 1296 *Atmos. Ocean. Tech.* 26, 1867–1890.
- 1297 Compo, G. P., Whitaker, J. S., Sardeshmukh, P. D., Matsui, N., Allan, R. J., Yin, X., et al. (2011).
 1298 The Twentieth Century Reanalysis Project. *Q. J. Roy. Meteor. Soc.*, 137, 1–28. doi: 10.1002/qj.776
- 1299 Corlett, G. K., Merchant, C. J., Minnett, P. J., and Donlon, C. J. (2014). “Assessment of long-term
 1300 satellite derived sea surface temperature records,” in *Experimental Methods in the Physical Sciences,*
 1301 *Vol 47, Optical Radiometry for Ocean Climate Measurements*, eds G. Zibordi, C. J. Donlon, and A.
 1302 C. Parr (Academic Press), 639–677. doi: 10.1016/B978-0-12-417011-7.00021-0
- 1303 Cronin, M. F., and Kessler, W. S. (2009). Near-surface shear flow in the tropical Pacific cold tongue
 1304 front. *J. Phys. Oceanogr.* 39, 1200–1215. doi: 10.1175/2008JPO4064.1
- 1305 Cronin, M. F., and McPhaden, M. J. (1999). Diurnal cycle of rainfall and surface salinity in the
 1306 western Pacific warm pool. *Geophys. Res. Lett.* 26, 3465–3467.
- 1307 Cronin, M. F., Fairall, C. W., and McPhaden, M. J. (2006). An assessment of buoy-derived and
 1308 numerical weather prediction surface heat fluxes in the tropical Pacific. *J. Geophys. Res.* 111,
 1309 C06038. doi: 10.1029/2005JC003324
- 1310 Cronin, M. F., Bond, N. A., Farrar, J. T., Ichikawa, H., Jayne, S. R., Kawai, Y., et al. (2013).
 1311 Formation and erosion of the seasonal thermocline in the Kuroshio Extension Recirculation Gyre.
 1312 *Deep-Sea Res. Part II* 85, 62–74. doi: 10.1016/j.dsr2.2012.07.018
- 1313 Cronin, M. F., Pelland, N. A., Emerson, S. R., and Crawford, W. R. (2015). Estimating diffusivity
 1314 from the mixed layer heat and salt balances in the North Pacific. *J. Geophys. Res. Oceans* 120, 7346–
 1315 7362. doi: 10.1002/2015JC011010
- 1316 Cronin, M. F., Bourassa, M., Clayson, C. A., Edson, J., Fairall, C., Feely, D., et al. (2014). “White
 1317 Paper #11—Wind stress and air sea fluxes observations: Status, implementation and gaps,” in
 1318 *Proceedings of the Tropical Pacific Observing System 2020 Workshop, A Future Sustained Tropical*
 1319 *Tropical Pacific Ocean Observing System for Research and Forecasting*, 27–30 January 2014 (La Jolla, CA).
- 1320 Dee, D., Uppala, S. M., Simmons, A. J., Berrisford, P., Poli, P., Kobayashi, S., et al. (2011). The
 1321 ERA-Interim reanalysis: Configuration and performance of the data assimilation system. *Q. J. Roy.*
 1322 *Meteor. Soc.* 137, 553–597, doi: 10.1002/qj.828

- 1323 Donelan, M. A., Dobson, F. W., Smith, S. D., and Anderson, R. J. (1993). On the dependence of sea
 1324 surface roughness on wave development. *J. Phys. Oceanogr.* 23, 2143–2149
- 1325 Donelan, M. A., Drennan, W. M., and Katsaros, K. B. (1997). The air–sea momentum flux in
 1326 conditions of wind sea and swell. *J. Phys. Oceanogr.* 27, 2087–2099. doi: 10.1175/1520-
 1327 0485(1997)027<2087:Tasmfi>2.0.Co;2
- 1328 Donlon, C. J., Minnett, P. J., Gentemann, C., Nightingale, T. J., Barton, I. J., Ward, B., et al. (2002).
 1329 Toward improved validation of satellite sea surface skin temperature measurements for climate
 1330 research. *J. Climate* 15, 353–369. doi: 10.1175/1520-0442(2002)015<0353:TIVOSS>2.0.CO;2
- 1331 Drennan, W. M., Taylor, P. K., and Yelland, M. J. (2005). Parameterizing the sea surface roughness.
 1332 *J. Phys. Oceanogr.* 35, 835–848.
- 1333 Drennan, W. M., Gruber, H. C., Hauser, D., and Quentin, C. (2003). On the wave age dependence of
 1334 wind stress over pure wind seas. *J. Geophys. Res.* 108(C3), 8062. doi: 10.1029/2000JC000715
- 1335 Drennan, W. M., Gruber, H. C., Collins, III, C. O., Herrera, A., Potter, H., Ramos, R. J., et al. (2014).
 1336 EASI: An air–sea interaction buoy for high winds. *J. Atmos. Ocean. Tech.* 31, 1397–1409. doi:
 1337 10.1175/jtech-d-13-00201.1
- 1338 du Penhoat, Y., Reverdin, G., and Caniaux, G. (2002). A Lagrangian investigation of vertical
 1339 turbulent heat fluxes in the upper ocean during Tropical Ocean–Global Atmosphere/Coupled Ocean-
 1340 Atmosphere Response Experiment (TOGA-COARE). *J. Geophys. Res.* 107(C5), 7-1–7-14. doi:
 1341 10.1029/2001JC000926
- 1342 Dyer, A. J., and Bradley, E. F. (1982). An alternative analysis of flux-gradient relationships at the
 1343 1976 ITCE. *Bound.-Layer Meteorol.* 22, 3–19.
- 1344 Dyer, A. J., and Hicks, B. B. (1970). Flux-gradient relationships in the constant flux layer. *Q. J. Roy.*
 1345 *Meteor. Soc.* 96, 715–721.
- 1346 Eastman, R., Warren, S. G., and Hahn, C. J. (2011). Variations in cloud cover and cloud types over
 1347 the ocean from surface observations, 1954–2008. *J. Climate* 24, 5914–5934.
- 1348 Edson, J. B., and Fairall, C. W. (1998). Similarity relationships in the marine surface layer. *J. Atmos.*
 1349 *Sci.* 55, 2311–2328.
- 1350 Edson, J., Crawford, T., Crescenti, J., Farrar, T., Frew, N., Gerbi, G., et al. (2007). The coupled
 1351 boundary layers and air–sea transfer experiment in low winds. *Bull. Amer. Meteor. Soc.* 88, 341–356.
 1352 doi: 10.1175/BAMS-88-3-341
- 1353 Edson, J. B., Zappa, C. J., Ware, J. A., McGillis, W. R., and Hare, J. E. (2004). Scalar flux profile
 1354 relationships over the open ocean. *J. Geophys. Res.*, 109, C08S09. doi: 10.1029/2003JC001960
- 1355 Edson, J. B., Jampana, V., Weller, R. A., Bigorre, S., Plueddemann, A. J., Fairall, C. W., et al.
 1356 (2013). On the exchange of momentum over the open ocean. *J. Phys. Oceanogr.* 43, 1589–1610.

- 1357 Esbensen, S. K., Chelton, D. B., Vickers, D., and Sun, J. (1993). An analysis of errors in special
 1358 sensor microwave imager evaporation estimates over the global oceans. *J. Geophys. Res.* 98(C4),
 1359 7081–7101. doi: 10.1029/93JC00011
- 1360 Fairall, C. W., Bradley, E. F., Godfrey, J. S., Wick, G. A., Edson, J. B., and Young, G. S. (1996a).
 1361 Cool skin and warm layer effects on the sea surface temperature. *J. Geophys. Res.* 101, 1295–1308.
- 1362 Fairall, C. W., Bradley, E. F., Rogers, D. P., Edson, J. B., and Young, G. S. (1996b). Bulk
 1363 parameterization of air-sea fluxes or the Tropical Ocean Coupled-Ocean Atmosphere Response
 1364 Experiment. *J. Geophys. Res.* 101(C2), 3747–3764. doi: 10.1029/95JC03205
- 1365 Fairall, C. W., White, A. B., Edson, J. B., and Hare, J. E. (1997). Integrated shipboard measurements
 1366 of the marine boundary layer. *J. Atmos. Ocean. Tech.* 14, 338–359.
- 1367 Fairall, C. W., Bradley, E. F., Hare, J. E., Grachev, A. A., and Edson, J. B. (2003). Bulk
 1368 parameterization of air-sea fluxes: Updates and verification for the COARE algorithm, *J. Climate* 16,
 1369 571–591. doi: 10.1175/1520-0442(2003)016<0571:BPOASF>2.0.CO;2
- 1370 Farrar, J. T., Rainville, L., Plueddemann, A. J., Kessler, W. S., Lee, C., Hodges, B. A., et al. (2015).
 1371 Salinity and temperature balances at the SPURS Central Mooring during fall and winter.
 1372 *Oceanography* 28, 56–65.
- 1373 Fisher, F. H., and Spiess, F. N. (1963). Flip-floating instrument platform. *J. Acoust. Soc. Am.* 35(10),
 1374 1633–1644.
- 1375 Foltz, G. R., Evan, A. T., Freitag, H. P., Brown, S., and McPhaden, M. J. (2013). Dust accumulation
 1376 biases in PIRATA shortwave radiation records. *J. Atmos. Ocean. Tech.* 30, 1414–1432.
- 1377 Freeland, H. (2007). A short history of Ocean Station Papa and Line P. *Prog. Oceanogr.* 75, 120–
 1378 125.
- 1379 Freeman, E., Kent, E. C., Brohan, P., Cram, T., Gates, L., Huang, B., et al. (2019). The International
 1380 Comprehensive Ocean-Atmosphere Data Set – Meeting users needs and future priorities. *Front. Mar.
 1381 Sci.* submitted.
- 1382 Freeman, E., Woodruff, S. D., Worley, S. J., Lubker, S. J., Kent, E. C., Angel, W. E., et al. (2017).
 1383 ICOADS Release 3.0: A major update to the historical marine climate record. *Int. J. Climatol.* 37,
 1384 2211–2232. doi: 10.1002/joc.4775
- 1385 Fu, X., and Wang, B. (2004). The boreal summer intraseasonal oscillations simulated in a hybrid
 1386 coupled atmosphere–ocean model. *Mon. Wea. Rev.* 132, 2628–2649.
- 1387 Fujitani, T. (1981). Direct measurement of turbulent fluxes over the sea during AMTEX. *Pap.
 1388 Meteor. Geophys.* 32, 119–134.
- 1389 Fujitani, T. (1985). Method of turbulent flux measurement on a ship by using a stable platform
 1390 system. *Pap. Meteor. Geophys.* 36, 157–170.
- 1391 Fung, I. Y., Harrison, D. E., and Lacis, A. A. (1984). On the variability of the net longwave radiation
 1392 at the sea surface. *Rev. Geophys. Space Phys.* 22(2), 177–193.

- 1393 Gentemann, C. L. (2014). Three way validation of MODIS and AMSR-E sea surface temperatures. *J.
1394 Geophys. Res. Oceans* 119, 2583–2598, doi: 10.1002/2013JC009716
- 1395 Gentemann, C. L., and Hilburn, K. A. (2015). In situ validation of sea surface temperatures from the
1396 GCOM-W1 AMSR2 RSS calibrated brightness temperatures. *J. Geophys. Res.* 120(5), 3567–3585.
1397 doi: 10.1002/2014JC010574
- 1398 Gruber, H. C., Terray, E., Donelan, M. A., Drennan, W. M., Van Leer, J. C., and Peters, D. B. (2000).
1399 ASIS—A new air-sea interaction Spar Buoy: Design and performance at sea. *J. Atmos. Ocean. Tech.*
1400 17, 708–720.
- 1401 Grachev, A. A., Andreas, E. L., Fairall, C. W., Guest, P. S., and Persson, P. O. G. (2007). SHEBA
1402 flux-profile relationships in the stable atmospheric boundary layer. *Bound.-Layer Meteorol.* 124(3),
1403 315–333.
- 1404 Grachev, A. A., Fairall, C. W., Hare, J. E., Edson, J. B., and Miller, S. D. (2003). Wind stress vector
1405 over ocean waves. *J. Phys. Oceanogr.* 33, 2408–2429.
- 1406 Grare, L., Lenain, L., and Melville, W. K. (2013). Wave-coherent airflow and critical layers over
1407 ocean waves. *J. Phys. Oceanogr.* 43, 2156–2172.
- 1408 Grare, L., Lenain, L., and Melville, W. K. (2018). Vertical profiles of the wave-induced airflow
1409 above ocean surface waves. *J. Phys. Oceanogr.* 48, 2901–2922.
- 1410 Grossman, R. L., and Betts, A. K. (1990). Air-sea interaction during an extreme cold air outbreak
1411 from the eastern coast of the United States. *Mon. Wea. Rev.* 118(2), 324–342.
- 1412 Gulev, S. K., and Belyaev, K. P. (2012). Probability distribution characteristics for surface air-sea
1413 turbulent heat fluxes over the global ocean. *J. Climate* 25, 184–206. doi: 10.1175/2011JCLI4211.1
- 1414 Gulev, S. K., Jung, T., and Ruprecht, E. (2007). Estimation of the impact of sampling errors in the
1415 VOS observations on air-sea fluxes. Part I. Uncertainties in climate means. *J. Climate* 20, 279–301.
- 1416 Gulev, S. K., Latif, M., Keenlyside, N., Park, W., and Koltermann, K. P. (2013). North Atlantic
1417 Ocean control on surface heat flux on multidecadal timescales. *Nature* 499, 464–467. doi:
1418 10.1038/nature12268
- 1419 Hara, T., and Belcher, S. E. (2004). Wind profile and drag coefficient over mature ocean surface
1420 wave spectra. *J. Phys. Oceanogr.* 34, 2345–2358.
- 1421 Hara, T., and Sullivan, P. P. (2015). Wave boundary layer turbulence over surface waves in a
1422 strongly forced condition. *J. Phys. Oceanogr.* 45, 868–883.
- 1423 Herbers, T. H. C., Jessen, P. F., Janssen, T. T., Colbert, D. B., and MacMahan, J. H. (2012).
1424 Observing ocean surface waves with GPS-tracked buoys. *J. Atmos. Ocean. Tech.* 29, 944–959. doi:
1425 10.1175/jtech-d-11-00128.1
- 1426 Hirahara, S., Ishii, M., and Fukuda, Y. (2014). Centennial-scale sea surface temperature analysis and
1427 its uncertainty. *J. Climate* 27, 57–75, doi: 10.1175/JCLI-D-12-00837.1

- 1428 Hobday, A. J., Oliver, E. C. J., Sen Gupta, A., Benthuysen, J. A., Burrows, M. T., Donat, M. G., et al.
 1429 (2018). Categorizing and naming marine heatwaves. *Oceanography* 31(2), 162–173. doi:
 1430 10.5670/oceanog.2018.205
- 1431 Hristov, T., and Ruiz-Plancarte, J. (2014). Dynamic balances in a wavy boundary layer. *J. Phys.*
 1432 *Oceanogr.* 44, 3185–3194. doi: 10.1175/JPO-D-13-0209.1
- 1433 Huang, B., Thorne, P. W., Banzon, V. F., Boyer, T., Chepurin, G., Lawrimore, J. H., et al. (2017).
 1434 Extended Reconstructed Sea Surface Temperature, Version 5 (ERSSTv5): Upgrades, validations, and
 1435 intercomparisons. *J. Climate* 30, 8179–8205. doi: 10.1175/JCLI-D-16-0836.1
- 1436 Jackson, D. L., and Stephens, G. L. (1995). A study of SSM/I-derived columnar water vapor over the
 1437 global oceans. *J. Climate* 8, 2025–2038. doi: 10.1175/1520-
 1438 0442(1995)008<2025:ASOSDC>2.0.CO;2
- 1439 Jackson, D. L., and Wick, G.A. (2010). Near-surface air temperature retrieval derived from AMSU-A
 1440 and sea surface temperature observations. *J. Atmos. Ocean. Technol.* 27, 1769–1776. doi:
 1441 10.1175/2010JTECHA1414.1
- 1442 Jacob, S. D., Shay, L. K., and Mariano, A. J. (2000). The 3D oceanic mixed layer response to
 1443 Hurricane Gilbert. *J. Phys. Oceanogr.* 30, 1407–1429. doi: 10.1175/1520-
 1444 0485(2000)030<1407:TOMLRT>2.0.CO;2
- 1445 Jiang, C., Cronin, M. F., Kelly, K. A., and Thompson, L. (2005). Evaluation of a hybrid satellite- and
 1446 NWP-based turbulent heat flux product using Tropical Atmosphere-Ocean (TAO) buoys. *J. Geophys.*
 1447 *Res. Oceans* 110, C09007. doi: 10.1029/2004JC002824
- 1448 Jin, Z., Charlock, T. P., Smith, W. L., and Rutledge, K. (2004). A parameterization of ocean surface
 1449 albedo. *Geophys. Res. Lett.* 31, L22301. doi: 10.1029/2004GL021180
- 1450 Josey, S. A., Kent, E. C., and Taylor, P. K. (1999). New insights into the ocean heat budget closure
 1451 problem from analysis of the SOC air-sea flux climatology. *J. Climate* 12, 2856–2880.
- 1452 Josey, S. A., Gulev, S. and Yu, L. (2013). “Exchanges through the ocean surface,” in *Ocean*
 1453 *Circulation and Climate: A 21st Century Perspective. 2nd Edition*, eds G. Siedler, S. Griffies, J.
 1454 Gould, and J. Church (Oxford: Academic Press), 115–140.
- 1455 Kaimal, J. C., Wyngaard, J. C., Izumi, Y. and Coté, O. R. (1972). Spectral characteristics of surface-
 1456 layer turbulence. *Q. J. Roy. Meteor. Soc.* 98, 563–589.
- 1457 Kalnay, E., Kanamitsu, M., Kistler, R., Collins, W., Deaven, D., Gandin, L., et al. (1996). The
 1458 NCEP/NCAR 40-Year Reanalysis Project. *Bull. Amer. Meteor. Soc.* 77, 437–472. doi: 10.1175/1520-
 1459 0477(1996)077<0437:TNYRP>2.0.CO;2
- 1460 Kato, S., Rose, F. G., Rutan, D. A., Thorsen, T. J., Loeb, N. G., Doelling, D. R., et al. (2018). Surface
 1461 irradiances of Edition 4.0 Clouds and the Earth’s Radiant Energy System (CERES) Energy Balanced
 1462 and Filled (EBAF) data product. *J. Climate* 31, 4501–4527. doi: 10.1175/JCLI-D-17-0523.1
- 1463 Kawamura, R., Fukuta, Y., Ueda, H., Matsuura, T., and Iizuka, S. (2002). A mechanism of the onset
 1464 of the Australian summer monsoon. *J. Geophys. Res. Atmospheres* 107(D14), ACL 5-1–ACL 5-15.

- 1465 Kennedy, J. J., Rayner, N. A., Smith, R. O., Parker, D. E., and Saunby, M. (2011). Reassessing biases
 1466 and other uncertainties in sea surface temperature observations measured in situ since 1850: 1.
 1467 Measurement and sampling uncertainties. *J. Geophys. Res.* 116, D14103. doi:
 1468 10.1029/2010JD015218
- 1469 Kent, E. C., Rayner, N. A., Berry, D. I., Saunby, M., Moat, B. I., Kennedy, J. J., et al. (2013). Global
 1470 analysis of night marine air temperature and its uncertainty since 1880: The HadNMAT2 data set. *J.*
 1471 *Geophys. Res. Atmos.* 118, 1281–1298. doi: 10.1002/jgrd.50152
- 1472 Kilpatrick, K. A., Podestá, G., Walsh, S., Williams, E., Halliwell, V., Szczodrak, M., et al. (2015). A
 1473 decade of sea surface temperature from MODIS. *Remote Sens. Environ.* 165, 27–41. doi:
 1474 10.1016/j.rse.2015.04.023
- 1475 Kilpatrick, K. A., Podestá, G., Williams, E., Walsh, S., and Minnett, P. J. (2019). Alternating
 1476 decision trees for cloud masking MODIS and VIIRS NASA SST products. *J. Atmos. Ocean. Tech.*
 1477 36(3), 387–407. doi: 10.1175/JTECH-D-18-0103.1
- 1478 Kobayashi, S., Ota, Y., Harada, Y., Ebita, A., Moriya, M., Onoda, H., et al. (2015). The JRA-55
 1479 reanalysis: General specifications and basic characteristics. *J. Meteor. Soc. Jpn.* 93, 5–48. doi:
 1480 10.2151/jmsj.2015-001
- 1481 Kudryavtsev, V., Chapron, B., and Makin, V. (2014). Impact of wind waves on the air-sea fluxes: A
 1482 coupled model. *J. Geophys. Res. Oceans* 119, 1217–1236. doi: 10.1002/2013JC009412.
- 1483 Kukulka, T., Hara, T., and Belcher, S. E. (2007). A model of the air-sea momentum flux and
 1484 breaking-wave distribution for strongly forced wind waves. *J. Phys. Oceanogr.* 37, 1811–1828. doi:
 1485 10.1175/JPO3084.1
- 1486 Landwehr, S., O'Sullivan, N., and Ward, B. (2015). Direct flux measurements from mobile platforms
 1487 at sea: Motion and airflow distortion corrections revisited. *J. Atmos. Oceanic. Tech.* 32, 1163–1178.
- 1488 Large, W. G., and Pond, S. (1981). Open ocean momentum flux measurements in moderate to strong
 1489 winds. *J. Phys. Oceanogr.* 11, 324–336. doi: 10.1175/1520-
 1490 0485(1981)011<0324:OOMFMI>2.0.CO;2
- 1491 Large, W. G., and Yeager, S. G. (2009). The global climatology of an interannually varying air-sea
 1492 flux data set. *Climate Dyn.* 33, 341–364.
- 1493 Lenain, L., and Melville, W. K. (2014). Autonomous surface vehicle measurements of the ocean's
 1494 response to Tropical Cyclone Freda. *J. Atmos. Oceanic Tech.* 31, 2169–2190. doi: 10.1175/jtech-d-
 1495 14-00012.1
- 1496 Levitus, S., Antonov, J. I., Boyer, T. P., Baranova, O. K., Garcia, H. E., Locarnini, R. A., et al.
 1497 (2012). World ocean heat content and thermosteric sea level change (0–2000 m), 1955–2010.
 1498 *Geophys. Res. Lett.* 39, L10603. doi: 10.1029/2012GL051106
- 1499 Li, J., Scinocca, J., Lazare, M., McFarlane, N., von Salzen, K., and Solheim, L. (2006). Ocean
 1500 surface albedo and its impact on radiation balance in climate models. *J. Climate* 19, 6314–6333.

- 1501 Li, X., Dick, G., Lu, C., Ge, M., Nilsson, T., Ning, T., et al. (2015). Multi-GNSS meteorology: Real-
1502 time retrieving of atmospheric water vapor from BeiDou, Galileo, GLONASS, and GPS
1503 observations. *IEEE Trans. Geosci. Remote Sens.* 53(12), 6385–6393.
- 1504 Liman, J., Schröder, M., Fennig, K., Andersson, A., and Hollmann, R. (2018). Uncertainty
1505 characterization of HOAPS 3.3 latent heat-flux-related parameters. *Atmos. Meas. Tech.* 11, 1793–
1506 1815. doi: 10.5194/amt-11-1793-2018
- 1507 Lin, W., Portabella, M., Stoffelen, A., Verhoef, A., and Turiel, A. (2015). ASCAT wind quality
1508 control near rain. *IEEE Trans. Geosci. Remote Sens.* 53(8), 4165–4177. doi:
1509 10.1109/TGRS.2015.2392372
- 1510 Lindstrom, E. J., Gunn, A., Fischer, A., and McCurdy, L. K. (2012). *A Framework for Ocean
1511 Observing. By the Task Team for an Integrated Framework for Sustained Ocean Observing.*
1512 UNESCO 2012, IOC/INF-1284 rev.
- 1513 Liu, W. T., and Niiler, P. P. (1984). Determination of monthly mean humidity in the atmospheric
1514 surface layer over oceans from satellite data. *J. Phys. Oceanogr.* 14, 1451–1457. doi: 10.1175/1520-
1515 0485(1984)014<1451:DOMMHI>2.0.CO;2
- 1516 Liu, W. T., Katsaros, K., and Businger, J. (1979). Bulk parameterization of air-sea exchanges of heat
1517 and water vapor including the molecular constraints at the interface. *J. Atmos. Sci.*, 36, 1722–1735.
- 1518 Liu, Y., and Minnett, P. J. (2016). Sampling errors in satellite-derived infrared sea-surface
1519 temperatures. Part I: Global and regional MODIS fields. *Remote Sens. Environ.* 177, 48–64.
- 1520 Mahrt, L., Vickers, D., Howell, J., Højstrup, J., Wilczak, J. M., Edson, J. B., et al. (1996). Sea surface
1521 drag coefficients in RASEX. *J. Geophys. Res.* 101, 14,327–14,335.
- 1522 May, J., and Bourassa, M. A. (2011). Quantifying variance due to temporal and spatial difference
1523 between ship and satellite winds. *J. Geophys. Res.* 116, C08013. doi: 10.1029/2010JC006931
- 1524 Mazloff, M. R., Cornuelle, B. D., Gille, S. T., and Verdy, A. (2018). Correlation lengths for
1525 constraining the large-scale carbon and heat content of the Southern Ocean. *J. Geophys. Res. Oceans*
1526 123, 883–901. doi: 10.1002/2017JC013408
- 1527 McPhaden, M. J., Busalacchi, A. J., Cheney, R., Donguy, J.-R., Gage, K. S., Halpern, D., et al.
1528 (1998). The Tropical Ocean Global Atmosphere observing system: A decade of progress. *J. Geophys.
1529 Res.* 103(C7), 14,169–14,240. doi: 10.1029/97JC02906
- 1530 McPhaden, M. J., Meyers, G., Ando, K., Masumoto, Y., Murty, V. S. N., Ravichandran, M., et al.
1531 (2009). RAMA: The Research Moored Array for African-Asian-Australian Monsoon Analysis and
1532 Prediction. *Bull. Am. Meteor. Soc.* 90, 459–480.
- 1533 Mechoso, C. R., Wood, R., Weller, R., Bretherton, C. S., Clarke, A. D., Coe, H., et al. (2014). Ocean-
1534 cloud-atmosphere-land interactions in the southeastern Pacific: The VOCALS program. *Bull. Amer.
1535 Meteor. Soc.*, 95, 357–375. doi:10.1175/BAMS-D-11-00246.1

- 1536 Meissner, T., Wentz, F. J., and Ricciardulli, L. (2014). The emission and scattering of L-band
 1537 microwave radiation from rough ocean surfaces and wind speed measurements from the Aquarius
 1538 sensor. *J. Geophys. Res. Oceans* 119, 6499–6522.
- 1539 Meissner, T., and Wentz, F. J. (2012). The emissivity of the ocean surface between 6 and 90 GHz
 1540 over a large range of wind speeds and earth incidence angles. *IEEE Trans. Geosci. Remote Sens.* 50,
 1541 3004–3026.
- 1542 Minnett, P. J., Smith, M., and Ward, B. (2011). Measurements of the oceanic thermal skin effect.
 1543 *Deep-Sea Res. Part II—Top. Stud. Oceanogr.* 58, 861–868. doi: 10.1016/j.dsr2.2010.10.024
- 1544 Minobe, S., Miyashita, M., Kuwano-Yoshida, A., Tokinaga, H., and Xie, S. P. (2010). Atmospheric
 1545 response to the Gulf Stream: Seasonal variations*. *J. Climate* 23 (13), 3699–3719.
- 1546 Mitarai, S., and McWilliams, J. C. (2016). Wave glider observations of surface winds and currents in
 1547 the core of Typhoon Danas. *Geophys. Res. Lett.* 43, 11,312–11,319. doi: 10.1002/2016GL071115
- 1548 Molod, A., Takacs, L., Suarez, M., and Bacmeister, J. (2015). Development of the GEOS-5
 1549 atmospheric general circulation model: Evolution from MERRA to MERRA2. *Geosci. Model Dev.* 8,
 1550 1339–1356. doi: 10.5194/gmd-8-1339-2015
- 1551 Monteiro, P. M. S., Gregor, L., Lévy, M., Maenner, S., Sabine, C. L., and Swart, S. (2015).
 1552 Intraseasonal variability linked to sampling alias in air-sea CO₂ fluxes in the Southern Ocean.
 1553 *Geophys. Res. Lett.* 42, 8507–8514. doi: 10.1002/2015GL066009
- 1554 Morey, S. L., Dukhovskoy, D. S., and Bourassa, M. A. (2009). Connectivity of the Apalachicola
 1555 River flow variability and the physical and bio-optical oceanic properties of the northern West
 1556 Florida Shelf. *Cont. Shelf Res.* 29, 1264–1275. doi: 10.1016/j.csr.2009.02.003
- 1557 Parfitt, R., Czaja, A., Minobe, S., and Kuwano-Yoshida, A. (2016). The atmospheric frontal response
 1558 to SST perturbations in the Gulf Stream region. *Geophys. Res. Lett.* 43(5), 2299–2306.
- 1559 Parfitt, R., and Seo, H. (2018). A new framework for near-surface wind convergence over the
 1560 Kuroshio Extension and Gulf Stream in wintertime: The role of atmospheric fronts. *Geophys. Res.
 1561 Lett.* 45(18), 9909–9918.
- 1562 Payne, R. E. (1972). Albedo of the sea surface. *J. Atmos. Sci.* 29, 959–970.
- 1563 Petrenko, B., Ignatov, A., Kihai, Y., Stroup, J., and Dash, P. (2014). Evaluation and selection of SST
 1564 regression algorithms for JPSS VIIRS. *J. Geophys. Res. Atmos.* 119, 4580–4599. doi:
 1565 10.1002/2013JD020637
- 1566 Pinker, R. T., Zhang, B. Z., Weller, R. A., and Chen, W. (2018). Evaluating surface radiation fluxes
 1567 observed from satellites in the southeastern Pacific Ocean. *Geophys. Res. Lett.* 45, 2404–2412. doi:
 1568 10.1002/2017GL076805
- 1569 Potter, H., Graber, H. C., Williams, N. J., Collins, C. O., Ramos, R. J., and Drennan, W. M. (2014).
 1570 In situ measurements of momentum fluxes in typhoons. *J. Atmos. Sci.* 72, 104–118. doi:
 1571 10.1175/JAS-D-14-0025.1

- 1572 Reising, S. C., Gaier, T. C., Kummerow, C. D., Padmanabhan, S., Lim, B. H., Brown, S. T., et al.
 1573 (2016). "Temporal experiment for storms and tropical systems technology demonstration
 1574 (TEMPEST-D): Reducing risk for 6U-Class nanosatellite constellations," in *2016 IEEE International*
 1575 *Geoscience and Remote Sensing Symposium (IGARSS)*, 5559–5560.
- 1576 Renfrew, I. A., and Moore, G. W. K. (1999). An extreme cold-air outbreak over the Labrador Sea:
 1577 Roll vortices and air-sea interaction. *Mon. Wea. Rev.* 127(10), 2379–2394.
- 1578 Reynolds, R. W., Chelton, D. B., Roberts-Jones, J., Martin, M. J., Menemenlis, D., and Merchant, C.
 1579 J. (2013). Objective determination of feature resolution in two sea surface temperature analyses. *J.*
 1580 *Climate* 26, 2514–2533. doi: 10.1175/JCLI-D-12-00787.1
- 1581 Richter, D. H., and Veron, F. (2016). Ocean spray: An outsized influence on weather and climate.
 1582 *Phys. Today* 66(11), 34–39.
- 1583 Roberts, J. B., Clayson, C. A., Robertson, F. R., and Jackson, D. (2010). Predicting near-surface
 1584 characteristics from SSM/I using neural networks with a first guess approach. *J. Geophys. Res.* 115,
 1585 D19113. doi: 10.1029/200d9JD013099
- 1586 Rodríguez, E., Bourassa, M., Chelton, D., Farrar, J. T., Long, D., Perkovic-Martin, D., and R.
 1587 Samelson, 2018: The winds and currents mission concept. *Front. Mar. Sci.*, submitted.
- 1588 Roemmich, D., Church, J., Gilson, J., Monselesan, D., Sutton, P. and Wijffels, S. (2015). Unabated
 1589 planetary warming and its ocean structure since 2006. *Nat. Clim. Change* 5, 240–245. doi:
 1590 10.1038/NCLIMATE2513
- 1591 Rutan, D. A., Kato, S., Doelling, D. R., Rose, F. G., Nguyen, L. T., Caldwell, T. E., et al. (2015).
 1592 CERES Synoptic product: Methodology and validation of surface radiant flux. *J. Atmos. Oceanic
 1593 Technol.* 32, 1121–1143. doi: 10.1175/JTECH-D-14-00165.1
- 1594 Saha, S., Moorthi, S., Pan, H.-L., Wu, X., Wang, J., Nadiga, S., et al. (2010). The NCEP Climate
 1595 Forecast System Reanalysis. *Bull. Amer. Meteor. Soc.* 91, 1015–1057. doi:
 1596 10.1175/2010BAMS3001.1
- 1597 Schmidt, K. M., Swart, S., Reason, C., and Nicholson, S.-A. (2017). Evaluation of satellite and
 1598 reanalysis wind products with in situ wave glider wind observations in the Southern Ocean. *J. Atmos.
 1599 Ocean. Tech.* 34, 2551–2568. doi: 10.1175/jtech-d-17-0079.1
- 1600 Schulz, E. W., Josey, S. A., and Verein, R. (2012). First air-sea flux mooring measurements in the
 1601 Southern Ocean, *Geophys. Res. Lett.*, 39, L16606, doi: 10.1029/2012GL052290
- 1602 Shaman, J., Samelson, R. M., and Skillingstad, E. (2010). Air-sea fluxes over the Gulf Stream
 1603 region: Atmospheric controls and trends. *J. Climate* 23(10), 2651–2670.
- 1604 Shi, Q. (2017). *Coupling ocean currents and waves with wind stress over the Gulf Stream*. Ph.D.
 1605 dissertation, Florida State University, Tallahassee, FL.

- 1606 Shibata, A. (2012). Ocean wind speed retrieval algorithm using the frequency 36GHz
 1607 vertical/horizontal and 6GHz horizontal data of the Advanced Microwave Scanning Radiometer
 1608 (AMSR). *Eur. J. Remote Sens.* 45(1), 133–140. doi: 10.5721/EuJRS20124513
- 1609 Shinoda, T., Hendon, H., and Glick, J. (1998). Intraseasonal variability of surface fluxes and sea
 1610 surface temperature in the tropical western Pacific and Indian Oceans. *J. Climate* 11, 1685–1702.
- 1611 Silverthorne, K. E., and Toole, J. M. (2013). Quasi-Lagrangian observations of the upper ocean
 1612 response to wintertime forcing in the Gulf Stream. *Deep-Sea Res. Part II* 91, 25–34.
- 1613 Smith, S. D. (1988). Coefficients for sea surface wind stress, heat flux, and wind profiles as a
 1614 function of wind speed and temperature. *J. Geophys. Res.*, 93(C12), 15,467–15,472. doi:
 1615 10.1029/JC093iC12p15467
- 1616 Smith, N., Kessler, W. S., Cravatte, S., Sprintall, J., Wijffels, S., Cronin, M. F., et al. (2019). Tropical
 1617 Pacific Observing System. *Front. Mar. Sci.* 6, 31, Oceanobs19: An Ocean of Opportunity. doi:
 1618 10.3389/fmars.2019.00031
- 1619 Sullivan, P. P., McWilliams, J. C., and Patton, E. G. (2014). Large-eddy simulation of marine
 1620 atmospheric boundary layers above a spectrum of moving waves. *J. Atmos. Sci.* 71, 4001–4027.
- 1621 Sullivan, P. P., Banner, M. L., Morison, R. P., and Peirson, W. L. (2018). Turbulent flow over steep
 1622 steady and unsteady waves under strong wind forcing. *J. Phys. Oceanogr.* 48, 3–27.
- 1623 Swart, S., Gille, S. T., Delille, B., Josey, S., Mazloff, M., Newman, L., Thompson, A. F., Thomson,
 1624 J., Ward, B., Du Plessis, M. D., Kent, E. C., Girton, J., Gregor, L., Hyder, P. H., Pezzi, L. P., De
 1625 Souza, R. B., Tamsitt, V., Weller, R.A., Zappa, C. J., (2019). Constraining Southern Ocean air-sea-
 1626 ice fluxes through enhanced observations. *Frontiers Mar. Sci.* in review.
- 1627 Thomson, J. (2012). Wave breaking dissipation observed with “SWIFT” drifters. *J. Atmos. Ocean.
 1628 Tech.* 29, 1866–1882. doi: 10.1175/jtech-d-12-00018.1
- 1629 Thomson, J., and Girton, J. (2017). Sustained measurements of Southern Ocean air-sea coupling
 1630 from a Wave Glider autonomous surface vehicle. *Oceanography* 30(2), 104–109. doi:
 1631 10.5670/oceanog.2017.228
- 1632 Tilinina, N., Gavrikov, A., and Gulev, S. (2018). Association of the North Atlantic surface turbulent
 1633 heat fluxes with midlatitude cyclones. *Mon. Wea. Rev.* 146, 3691–3715. doi: 10.1175/MWR-D-17-
 1634 0291.1
- 1635 Tomita, H., Hihara, T., and Kubota, M. (2018). Improved satellite estimation of near-surface
 1636 humidity using vertical water vapor profile information. *Geophys. Res. Lett.* 45, 899–906. doi:
 1637 10.1002/2017GL076384
- 1638 Tomita, H., Hihara, T., Kako, S. Kubota, M., and Kutsuwada, K. (2019). An introduction to J-
 1639 OFURO3, a third-generation Japanese ocean flux data set using remote-sensing observations. *J.
 1640 Oceanogr.* 75, 171–194. doi: 10.1007/s10872-018-0493-x

- 1641 Tomita, H., Kawai, Y., Cronin, M. F., Hihara, T., and Kubota, M. (2015). Validation of AMSR2 sea
 1642 surface wind and temperature over the Kuroshio Extension region. *SOLA* 11, 43–47. doi:
 1643 10.2151/sola.2015-010
- 1644 Tozuka, T., Ohishi, S., and Cronin, M. F. (2018). A metric for surface heat flux effect on horizontal
 1645 sea surface temperature gradients. *Climate Dyn.* 51, 547–561. doi: 10.1007/s00382-017-3940-2
- 1646 Tsujino, H., Urakawa, S., Nakano, H., Small, R. J., Kim, W. M., Yeager, S. G., et al. (2018). JRA-55
 1647 based surface dataset for driving ocean-sea-ice models (JRA55-do). *Ocean Model.* 130, 79–139. doi:
 1648 10.1016/j.ocemod.2018.07.002
- 1649 Tu, Q., Pan, D., and Hao, Z. (2015). Validation of S-NPP VIIRS sea surface temperature retrieved
 1650 from NAVO. *Remote Sens.* 7, 17,234–17,245.
- 1651 Valdivieso, M., Haines, K., Balmaseda, M., Chang, Y.-S., Drevillon, M., Ferry, N., et al. (2017). An
 1652 assessment of air–sea heat fluxes from ocean and coupled reanalyses. *Climate Dyn.* 49, 983–1008.
- 1653 Vickers, D., and Mahrt, L. (1999). Observations of non-dimensional wind shear in the coastal zone.
 1654 *Q. J. Roy. Meteor. Soc.* 125, 2685–2702.
- 1655 Villas Bôas, A. B., Sato, O. T., Chaigneau, A., and Castelão, G. P. (2015). The signature of
 1656 mesoscale eddies on the air-sea turbulent heat fluxes in the South Atlantic Ocean. *Geophys. Res. Lett.*
 1657 42, 1856–1862.
- 1658 von Engeln, A., and Teixeira, J. (2013). A planetary boundary layer height climatology derived from
 1659 ECMWF reanalysis data. *J. Climate* 26, 6575–6590. doi: 10.1175/JCLI-D-12-00385.1
- 1660 Wallcraft, A. J., Kara, A. B., Barron, C. N., Metzger, E. J., Pauley, R. L., and Bourassa, M. A.
 1661 (2009). Comparisons of monthly mean 10 m wind speeds from satellites and NWP products over the
 1662 global ocean. *J. Geophys. Res. Atmos.* 114, D16109. doi: 10.1029/2008JD011696
- 1663 Wang, W., and McPhaden, M. J. (2000). The surface-layer heat balance in the equatorial Pacific
 1664 Ocean. Part II: Interannual variability. *J. Phys. Oceanogr.* 30, 2989–3008.
- 1665 Webster, P. J., Clayson, C. A., and Curry, J. A. (1996). Clouds, radiation, and the diurnal cycle of sea
 1666 surface temperature in the tropical western Pacific. *J. Climate* 9, 1712–1730.
- 1667 Weller, R. A. (2015). Variability and trends in surface meteorology and air-sea fluxes at a site off
 1668 northern Chile. *J. Climate* 28(8), 3004–3023. doi: 10.1175/JCLI-D-14-00591.1
- 1669 Weller, R. A., Bigorre, S. P., Lord, J., Ware, J. D., and Edson, J. B. (2012). A surface mooring for air-
 1670 sea interaction research in the Gulf Stream. Part 1: Mooring design and instrumentation. *J. Atmos.*
 1671 *Ocean. Tech.* 29, 1363–1376.
- 1672 Wong, E. W., and Minnett, P. J. (2016a). Retrieval of the ocean skin temperature profiles from
 1673 measurements of infrared hyperspectral radiometers—Part I: Derivation of an algorithm. *IEEE Trans.*
 1674 *Geosci. Remote Sens.* 54, 1879–1890. doi: 10.1109/TGRS.2015.2483746

- 1675 Wong, E. W., and Minnett, P. J. (2016b). Retrieval of the ocean skin temperature profiles from
 1676 measurements of infrared hyperspectral radiometers—Part II: Field data analysis. *IEEE Trans.*
 1677 *Geosci. Remote Sens.* 54, 1891–1904. doi: 10.1109/TGRS.2015.2501425
- 1678 Wong, E. W., and Minnett, P. J. (2018). The response of the ocean thermal skin layer to variations in
 1679 incident infrared radiation. *J. Geophys. Res. Oceans* 123, 2475–2493. doi: 10.1002/2017JC013351
- 1680 Wu, J. (1994). The sea surface is aerodynamically rough even under light winds. *Bound. Layer*
 1681 *Meteorol.* 69, 149–158.
- 1682 Yelland, M. J., Moat, B. I., Taylor, P. K., Pascal, R. W., Hutchings, J., and Cornell, V. C. (1998).
 1683 Wind stress measurements from the open ocean corrected for airflow distortion by the ship. *J. Phys.*
 1684 *Oceanogr.* 28, 1511–1526. doi: 10.1175/1520-0485(1998)028<1511:WSMFTO>2.0.CO;2
- 1685 Yokoi, S., Katsumata, M., and Yoneyama, K. (2014). Variability in surface meteorology and air-sea
 1686 fluxes due to cumulus convective systems observed during CINDY/DYNAMO. *J. Geophys. Res.*
 1687 *Atmos.* 119, 2064–2078. doi: 10.1002/2013JD020621
- 1688 Yu, L. (2019). Global air–sea fluxes of heat, fresh water, and momentum: Energy budget closure and
 1689 unanswered questions. *Annu. Rev. Mar. Sci.* 11(1), 227–248. doi: 10.1146/annurev-marine-010816-
 1690 060704
- 1691 Yu, L., and Jin, X. (2012). Buoy perspective of a high-resolution global ocean vector wind analysis
 1692 using passive radiometers and active scatterometers from 1987 to the present. *J. Geophys. Res.* 117,
 1693 C11013. doi: 10.1029/2012JC008069
- 1694 Yu, L., and Jin, X. (2018). A regime-dependent retrieval algorithm for near-surface air temperature
 1695 and specific humidity from multi-microwave sensors. *Remote Sens. Environ.* 215, 199–216.
- 1696 Yu, L., and Weller, R. A. (2007). Objectively analyzed air-sea heat fluxes for the global ice-free
 1697 oceans (1981–2005). *Bull. Amer. Meteor. Soc.* 88(4), 527–539.
- 1698 Yu, L., Jin, X., Schulz, E. W., and Josey, S. A. (2017). Air-sea interaction regimes in the sub-
 1699 Antarctic Southern Ocean and Antarctic marginal ice zone revealed by icebreaker measurements. *J.*
 1700 *Geophys. Res. Oceans* 122, 6547–6564. doi: 10.1002/2016JC012281
- 1701 Zhang, D., Cronin, M. F., Wen, C., Xue, Y., and Kumar, A. (2016). Assessing surface heat fluxes in
 1702 atmospheric reanalyses with a decade of data from the NOAA Kuroshio Extension Observatory. *J.*
 1703 *Geophys. Res.* 121, 6874–6890. doi: 10.1002/2016JC011905
- 1704 Zhang, L., Shi, H., Wang, Z., Yu, H., Yin, X., and Liao, Q. (2018). Comparison of wind speeds from
 1705 spaceborne microwave radiometers with in situ observations and ECMWF data over the global
 1706 ocean. *Remote Sens.* 10(3), 425. doi: 10.3390/rs10030425
- 1707

1708
 1709
 1710
 1711
 1712
 1713
 1714
 1715
 1716

Table 1. Summary of flux EOV/ECV uncertainties based upon ASIMET sensor uncertainties stemming from laboratory calibration, sensor drift, and field impacts with estimates of total uncertainties in instantaneous, daily, and annual values (after Colbo and Weller, 2009). Flux uncertainties computed for tropical conditions using a database of ship observations and the COARE 3.5 algorithm; the uncertainty is the difference in fluxes averaged over the database (14103 tropical 1-hr observations) with and without the perturbation in the mean variable. Because passive radiation shields are used for air temperature and humidity sensors, values are given for different ranges of wind speed; in low winds and high insolation, air temperature and humidity errors are larger.

				Sensor Error (and contribution to Q_{net} error)		
Flux EOV/ECV	Lab Calibration	Drift	Field	Instantaneous	Daily	Annual
Downwelling Longwave Radiation	Coefficients of fit: 1.5 W m^{-2} Noise: 0.5 W m^{-2}	2 W m^{-2}	Tilt: < 2 W m^{-2} Temperature gradients: 4 W m^{-2} Salt spray: <1 W m^{-2} Solar: <1% SW_{in}	7.5 W m^{-2}	4 W m^{-2}	4 W m^{-2}
Downwelling Shortwave Radiation	2 W m^{-2}	< 2 W m^{-2}	Tilt: <2 W m^{-2} Temperature gradients: 1–2 W m^{-2} Salt spray: < 1 W m^{-2}	20 W m^{-2} , more in broken cloud	6 W m^{-2}	5 W m^{-2}
Humidity	Linear: 0.16 %RH Cubic: 0.1 %RH	0.9	Under 95 %RH: ± 1 %RH Heating in low winds: 3 %RH	1 %RH, 3.2 W m^{-2} 3 %RH, low winds, 10 W m^{-2}	1 %RH, 3.2 W m^{-2} 3 %RH, 10 W m^{-2}	1 %RH, 3.2 W m^{-2}
Air Temperature	<0.03 °C	0.05 °C	>1 °C, wind < 1 m s^{-1} 0.7 °C, wind = 2 m s^{-1} 0.4 °C, wind = 3 m s^{-1}	0.2 °C, more in low wind, 3.5 W m^{-2}	0.1 °C, 2.2 W m^{-2}	0.1 °C, 2.2 W m^{-2}
Barometric Pressure	0.06 hPa	1.5 hPa (max) 0.2 hPa	Temperature: 0.1 hPa Wind: <0.1 hPa (wind <10 m s^{-1})	0.3 hPa, 0.0 W m^{-2}	0.2 hPa, 0.0 W m^{-2}	0.2, 0.0 W m^{-2}
Sea Surface Temperature	0.001 °C	0.05 °C	Low wind: 0.1 °C Cool skin: <0.02 °C	0.1 °C, -4.4 W m^{-2}	0.1 °C, 4.4 W m^{-2}	0.04 °C, 1.7 W m^{-2}
Wind Speed	1%	+0.1 m s^{-1}	Tilt: <0.3% Sea state: uncertain Very low wind: $\pm 1 \text{ m s}^{-1}$	max (1.5%, 0.1 m s^{-1}) more in low wind 1.7 W m^{-2}	max (1%, 0.1 m s^{-1}) 1.6 W m^{-2}	max (1%, 0.1 m s^{-1}) 1.6 W m^{-2}
Wind Direction	Raw compass: 1° Buoy spin: 4°	2°	Low wind: 1° Flow distortion: <5°	6° (more in low wind)	5°	5°

1717
 1718

1719 **Table 2.** Accuracy of long-term average of heat flux components, net heat flux, wind stress
 1720 magnitude, and freshwater flux for an ASIMET system deployed in the subtropics, after Colbo and
 1721 Weller (2009). These numbers reflect the typical magnitude of systematic errors after averaging a
 1722 sufficiently large number of measurements so that random errors can be considered negligible (e.g.,
 1723 one year of hourly measurements). Numbers given for covariance are estimated assuming a single
 1724 commercial sonic anemometer and infrared absorption fast hygrometer system. Some uncertainty
 1725 will cancel out when combining data from an ensemble of covariance observing systems. For
 1726 example, for the PSD ship database containing data from 41 cruises residual statistical uncertainty in
 1727 mean covariance stress (averaged in wind speed bins) is described by $\text{sqrt}[(0.0003)^2 + (0.02|\tau|)^2]$.
 1728

	Q_{LW}	Q_{SW}	Q_{lat}	Q_{sen}	Q_{net}	$ \tau $	E-P
% Error (covariance flux % Error)	10	2.5	6 (5)	16 (14)	20 (16)	20 (9)	10 cm
Typical Error (covariance flux typical error)	3.9 W m^{-2}	5 W m^{-2}	7 W m^{-2} (5 W m^{-2})	2 W m^{-2} (1.5 W m^{-2})	10 W m^{-2} (8 W m^{-2})	0.007 N m^{-2} (0.005 N m^{-2})	10 cm

1729
 1730

1731
 1732
 1733
 1734
 1735
 1736
 1737
 1738
 1739
 1740
 1741
 1742
Table 3. Current capability in remotely sensed flux EOVS and corresponding error in net surface heat flux and wind stress. Accuracy values estimated from comparisons with buoys. Contribution to error in net surface heat flux computed from the tropical database as per Table 1. Column 2 (Sensor) describes instrumentation and where technological advances are needed. Column 5 shows daily resolution of gridded fields for all variables except solar and longwave radiation. For these, monthly-averaged resolution is shown. Unless otherwise noted, accuracies are total uncertainties, including random uncertainty. Also unless otherwise noted, accuracies are estimated from globally distributed comparisons. As the quoted effect of these uncertainty values on the net heat flux are based on Tropical/sub-Tropical measurements they may not apply at mid-high latitudes. Uncertainties of the gridded products do not include uncertainties due to sampling error, and therefore underestimate the true uncertainty by some unknown percentage.

Observable	Sensor	Horizontal Temporal Resolution	Sensor accuracy of swath (and contribution to Q_{net} uncertainty)	Uncertainty of gridded product at available daily or monthly resolution (and contribution to Q_{net} uncertainty)	Citations
Ocean surface wind speed and direction	Scatterometer and Passive Microwave Radiometer	25 km / 12 hr	0.6–1.6 m s ⁻¹ (13–26 W m ⁻²)	0.6–1.6 m s ⁻¹ (9.6–26 W m ⁻²)	Zhang et al. (2018) Yu and Jin (2012)
Skin SST	Infrared Radiometer; Passive Microwave Radiometer (which measures an approximation to the sub-skin temperature)	1 km / 12 hr	0.2–0.6 K (9–26 W m ⁻²)	0.2–0.6 K (9–26 W m ⁻²)	Corlett et al. (2014) Tu et al. (2015) Gentemann and Hilburn (2015) Kilpatrick et al. (2015) Bulgin et al. (2016)
Near surface air temp	Technology advancements needed	25 km / 12 hr	1.3–1.55 K (18–22 W m ⁻²)	0.5–1.55 K (6–22 W m ⁻²)	Jackson and Wick (2010) Roberts et al. (2010) Yu and Jin (2018)
Near surface specific air humidity	Passive Microwave Radiometer	25 km / 12 hr	1–1.3 g/kg (20–26 W m ⁻²)	0.8–1 g/kg (16–20 W m ⁻²)	Roberts et al. (2010) Tomita et al. (2018) Yu and Jin (2018)
Surface solar radiation	Imagers (multi-channel), CERES, ancillary	100 km / 3 hr	55 W m ⁻²	11 W m ⁻²	Rutan et al. (2015)

			(55 W m ⁻²)	(11W m ⁻²)	Kato et al. (2018)
Surface longwave radiation	Imagers (multi-channel), CERES, ancillary	100 km / 3 hr	20 W m ⁻² (20 W m ⁻²)	5 W m ⁻² (5 W m ⁻²)	Rutan et al. (2015) Kato et al. (2018)

1743

1744

1745

1746 **Table 4.** Various flux products information (based on Valdivieso et al. 2017, Bentamy et al. 2017,
 1747 Tomita et al. 2018 and Yu 2018), including temporal and horizontal (in degrees) resolution, period of
 1748 availability, flux components (Shortwave (Q_{SW}), Longwave (Q_{LW}), Sensible (Q_{sen}), Latent (Q_{lat}), Net
 1749 surface heat flux (Q_{net}), Freshwater Flux (FW), and Momentum flux (τ)). For Q_{net} products, their
 1750 global ocean mean value is also shown.

Type	Product	Resolution	Period	Flux availability	Global mean of NH [W m ⁻²] * ocean only	Citations
Satellite-based	CERES Surface EBAF, SYN1Deg	hourly, daily monthly, 1°	2000–	Q_{SW}, Q_{LW}	-	Kato et al. (2018); Rutan et al. (2015)
	HOAPS3.2	daily, 0.5°	1987–2008	$Q_{lat}, Q_{sen}, FW, \tau$	-	Andersson et al. (2011)
	IFREMER V4	daily, 0.25°	1992–June 2017	Q_{lat}, Q_{sen}	-	Bentamy et al. (2017)
	J-OFURO3	daily, 0.25°	1988–2013	$Q_{lat}, Q_{sen}, Q_{SW}, LW, Q_{net}, \tau, FW$	23	Tomita et al. (2018)
	OAFlux HR	daily, 0.25°	1988–	$Q_{lat}, Q_{sen}, FW, \tau$	5 (when combined with CERES EBAF)	Yu (2019)
	SeaFlux CDR	3 hr, 0.25°	1998–	Q_{lat}, Q_{sen}	-	Clayson and Brown (2016)
Latest atmospheric reanalysis	CFSR	1 hr, T382	1979–	$Q_{lat}, Q_{sen}, Q_{SW}, Q_{LW}, Q_{net}, \tau, FW$	15	Saha et al. (2010)
	ERA-Interim	6 hr, T255	1979–	$Q_{lat}, Q_{sen}, Q_{SW}, Q_{LW}, Q_{net}, \tau, FW$	9	Dee et al. (2011)
	JRA-55	3 hr, T319	1958–	$Q_{lat}, Q_{sen}, Q_{SW}, Q_{LW}, Q_{net}, \tau, FW$	-15	Kobayashi et al. (2015)

	MERRA2	1 hr, 0.5°	1979–	$Q_{lat}, Q_{sen}, Q_{SW}, Q_{LW}, Q_{net}, \tau, FW$	-5	Molod et al. (2015)
Blended	CORE.2	monthly, 1°	1984–2006	$Q_{lat}, Q_{sen}, Q_{SW}, Q_{LW}, Q_{net}, \tau, FW$	30 (unadjusted) 2 (adjusted)	Large and Yeager (2009) Josey et al. (2013)
	JRA-55-do	3 hr, 1.25°		$Q_{lat}, Q_{sen}, Q_{SW}, Q_{LW}, Q_{net}, \tau, FW$	1.8	Tsujino et al. (2018)
	OAFlux	daily, 1° monthly, 1°	1983–1958–	$Q_{lat}, Q_{sen}, Q_{SW}, Q_{LW}, Q_{net}, \tau$	25 (when combined with ISCCP)	Yu and Weller (2007)
Ship-based	NOC 2	monthly, 1°	1973–	$Q_{lat}, Q_{sen}, Q_{SW}, Q_{LW}, Q_{net}, \tau, FW$	24	Berry and Kent (2011)

1751
1752

1753 **Table 5.** Sampling and uncertainty targets for producing a 3-hourly 25-km (aspirational goal of
 1754 hourly at 10-km) gridded product of Q_{net} with a 1-day random uncertainty of 15 W m⁻² and a bias of
 1755 less than 5 W m⁻². This gridded product will likely use NWP to blend satellite and *in situ*
 1756 observations to meet these targets. Some regions, such as ice margins, may need better resolution
 1757 than these.

Flux EOV/ECV	Comment	Native Spatial Resolution	Temporal Resolution	Uncertainty Target (1-day)
Net surface heat flux	Technology advancements / improvement of bulk flux parameterization needed	≤10 km	hourly	random: 15 W m ⁻² bias: <5 W m ⁻²
Wind stress	Technology advancements	≤10 km	hourly	random: 0.01 N m ⁻² or 4% bias: 0.005 N m ⁻²
Ocean surface wind speed/direction	Technology advancements for resolution	≤10 km	hourly	random: 0.4 m s ⁻¹ or 4% bias: 0.24 m s ⁻¹
SST	Algorithm improvement needed	1 km	hourly	random: 0.2 K bias: 0.1 K
Near surface air temp	Technology advancements / algorithm improvements needed	≤10 km	hourly	random: 0.5 K bias: 0.2 K
Near surface specific air humidity	Technology advancements / algorithm improvements needed	≤10 km	hourly	random: 0.5 g k ⁻¹ bias: 0.3 g k ⁻¹
Sea surface current	Technology advancement needed	≤10 km	3 hourly	0.3 m s ⁻¹
Upwelling/downwelling surface solar radiation	Technology advancements / algorithm improvements	≤10 km	hourly	random: 5 W m ⁻² bias: 3 W m ⁻²
Upwelling/downwelling surface longwave radiation	Technology advancements / algorithm improvements	≤10 km	hourly	random: 5 W m ⁻² bias: 3 W m ⁻²

1758

1759

1760 **Figure Captions**

1761 **Figure 1.** (a) Annual mean net surface heat flux (Q_{net}) for 2016 from the OAFlux-HR + CERES
 1762 EBAFv4.0 product. (b) Annual mean wind stress curl and wind stress vectors for 2016 from the
 1763 OAFlux-HR. (c) Standard deviation of annual-mean Q_{net} from 12 products. (d) Standard deviation of
 1764 annual mean of surface wind stress magnitude from 12 products. (e) Standard deviation of annual-
 1765 mean surface shortwave and longwave ($Q_{sw} - Q_{lw}$) from 10 products. (f) Standard deviation of
 1766 annual-mean turbulent latent and sensible heat flux ($Q_{lat} + Q_{sen}$) from 11 products. Based on Yu
 1767 (2019).

1768 **Figure 2.** Target flux accuracy and scales for different phenomena. The space and time scales are
 1769 indicated by the extent of the bubble. The target accuracies, estimated at 10 to 20% of the observed
 1770 variability, are indicated by the color for net heat flux, and by the bubble's outline for surface stress.
 1771 The accuracy requirement for stress is a factor of 2 smaller for phenomena that are dependent on the
 1772 curl of the stress rather than the stress magnitude. See Table S1 for more detail. This figure is
 1773 updated and adapted from Bourassa et al. (2013).

1774 **Figure 3.** Examples of different types of air-sea flux *in situ* platforms. Clockwise from upper left:
 1775 UK weathership Polar Front (image courtesy of Norwegian Meteorological Institute); NOAA ship
 1776 Ron Brown (from www.noaa.gov); OSU "ROSS" ASV (ross.ceoas.oregonstate.edu; image courtesy
 1777 of San Nguyen, NguyenSan Photography); RSMAS "ASIS" spar buoy (Graber et al., 2000);
 1778 Saildrone, Inc. "Saildrone" ASV (image courtesy of Saildrone, Inc.; www.saildrone.com), Liquid
 1779 Robotics "Wave Glider" ASV (from www.liquid robotics.com with modifications by UW/APL),
 1780 UW/APL "SWIFT" drifter (Thomson, 2012); JAMSTEC TRITON buoy (from JAMSTEC,
 1781 www.jamstec.go.jp); and, in the center, the WHOI SPURS buoy (Farrar et al., 2015).

1782 **Figure 4.** Root mean square error and bias (satellite minus buoy) between daily buoy and J-
 1783 OFURO3 Q_{lat} and Q_{sen} (in Wm^{-2}) for the period 2002 – 2013. From Figure 5 of Tomita et al. (2019).

1784 **Figure 5.** Satellite sensors that are producing data that can be used in deriving estimates of ocean
 1785 surface fluxes. Normal text indicates current satellites and sensors, with * indicating those that are
 1786 beyond their planned lifetime. Italic font shows missions that are expected to be launched in the next
 1787 decade. Bold text shows areas needing attention in coming decade; red borders highlight where
 1788 significant action and progress are needed. Not all derived variables from all sensors will reach the
 1789 accuracies given in Table 3.

1790 **Figure 6.** (a) Global-ocean mean energy (Q_{net}) budget. (b) The ratio of the mean averages of $Q_{sw} -$
 1791 Q_{lw} to $Q_{lat} + Q_{sen}$; the dashed line denotes that this ratio equals 1.0. Abbreviations: 20CR, Twentieth
 1792 Century Reanalysis; CERES, Clouds and the Earth's Radiant Energy System–Energy Balanced and
 1793 Filled; CFSR, Climate Forecast System Reanalysis; ERA-20C, European Centre for Medium-Range
 1794 Weather Forecasts Twentieth Century; ERA-Interim, European Centre for Medium-Range Weather
 1795 Forecasts Interim; GPCP, Global Precipitation Climatology Project; JRA-55, Japanese 55-Year
 1796 Reanalysis; MERRA, Modern-Era Retrospective Analysis for Research and Applications; NCEP,
 1797 National Center for Environmental Prediction; NOC, National Oceanography Centre; OAFlux-1×1,
 1798 1°-gridded Objectively Analyzed Air–Sea Fluxes; OAFlux-HR3 and -HR4, high-resolution (0.25°-
 1799 gridded) Objectively Analyzed Air–Sea Fluxes analysis computed from Coupled Ocean–Atmosphere
 1800 Response Experiment (COARE) version 3 and version 4, respectively. The 12 products used here are
 1801 the same as used in Figure 1. From Yu (2019).

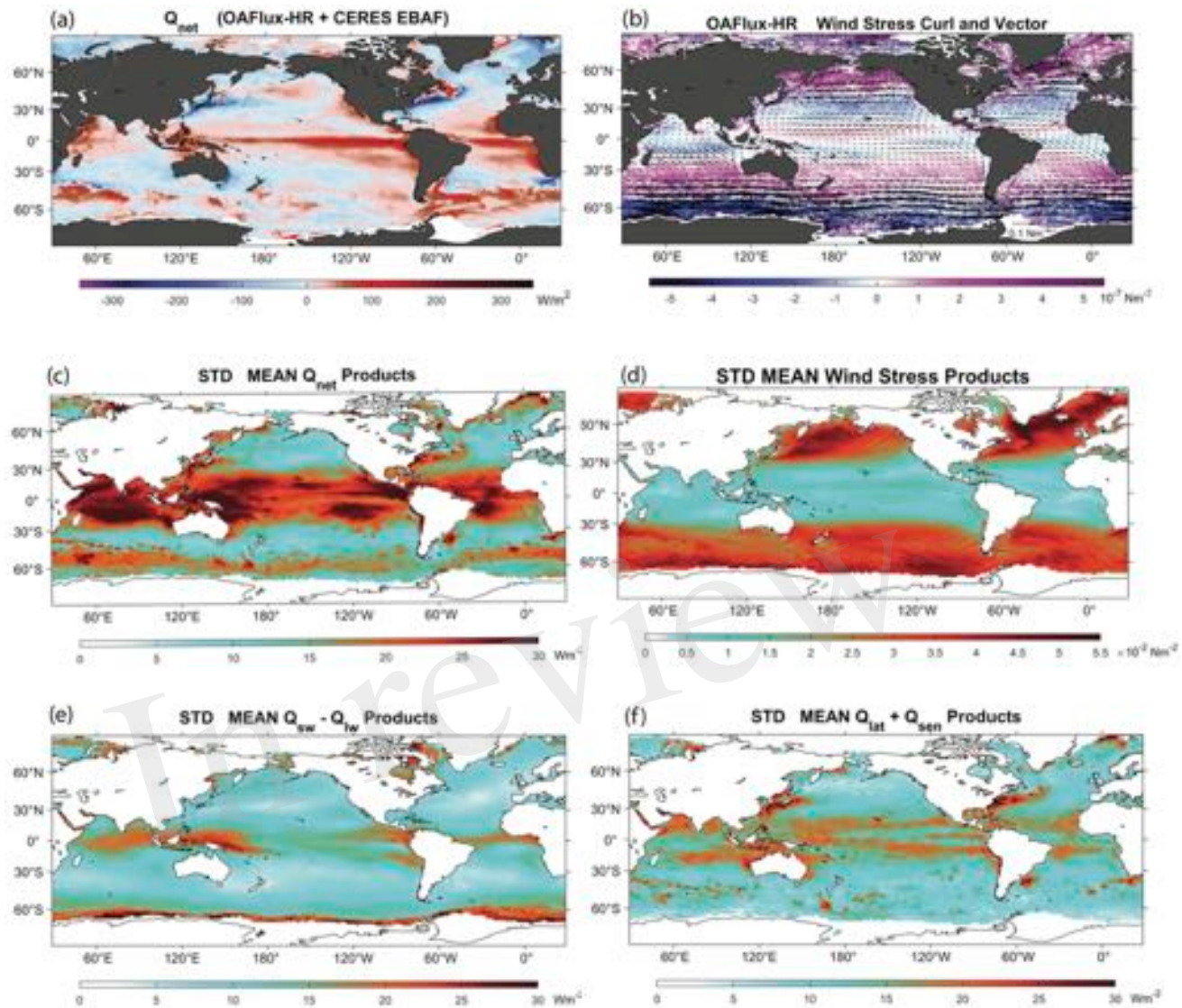
1802 **Figure 7.** Overall status of flux EOVS/ECVs, assuming recommendations made here are followed.

1803 **Figure 8.** Existing OceanSITES network of surface heat fluxes (filled black squares) with priority
1804 regions for new OceanSITES stations indicated by black boxes. The grey dots indicate nodes of a 10°
1805 by 10° grid, with 368 grid boxes in the global oceans. The background mean net surface heat flux is
1806 constructed from OAFlux-HR (Yu, 2019) and CERES EBAF (Kato et al., 2018) for the period of
1807 2001-2015.

1808 **Figure 9.** Roadmap chart for making improvements in air-sea fluxes over the next decade. Major
1809 recommendation activities are indicated in green. Arrows indicate that these activities are likely to be
1810 ongoing.

1811

1812

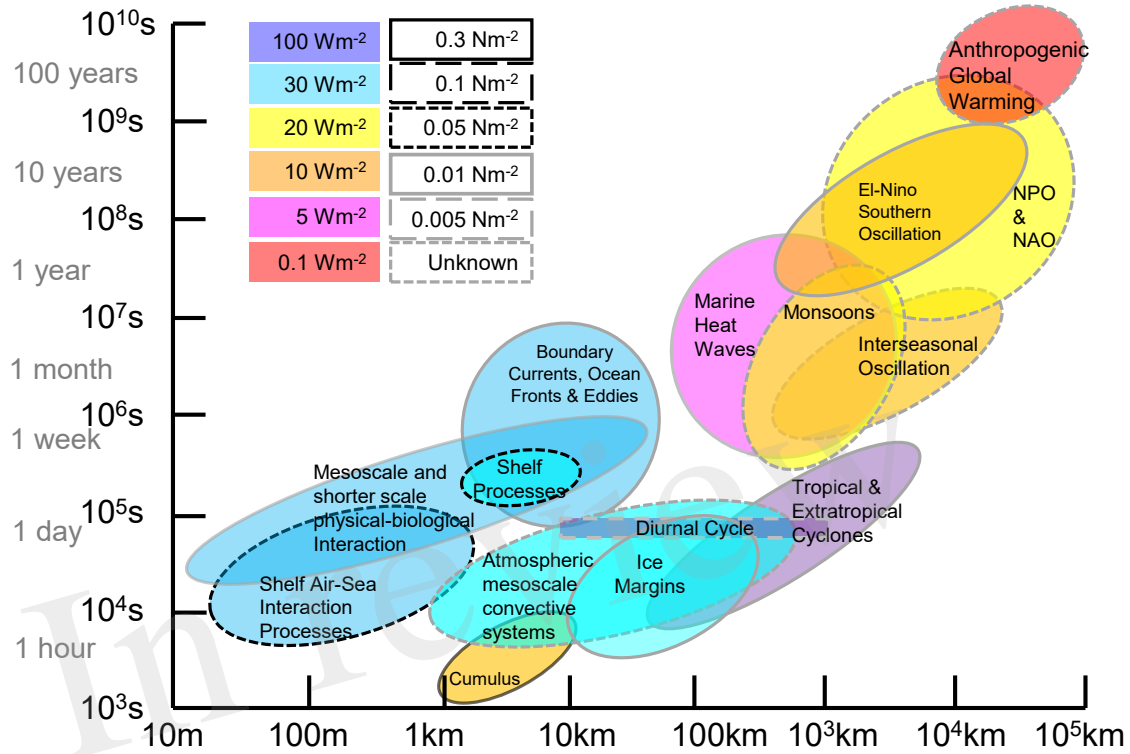


1813

1814 **Figure 1.** (a) Annual mean net surface heat flux (Q_{net}) for 2016 from the OAFlux-HR + CERES
 1815 EBAFv4.0 product. (b) Annual mean wind stress curl and wind stress vectors for 2016 from the
 1816 OAFlux-HR. (c) Standard deviation of annual-mean Q_{net} from 12 products. (d) Standard deviation of
 1817 annual mean of surface wind stress magnitude from 12 products. (e) Standard deviation of annual-
 1818 mean surface shortwave and longwave ($Q_{sw} - Q_{lw}$) from 10 products. (f) Standard deviation of
 1819 annual-mean turbulent latent and sensible heat flux ($Q_{lat} + Q_{sen}$) from 11 products. Based on Yu
 1820 (2019).

1821

Flux Accuracies and Processes

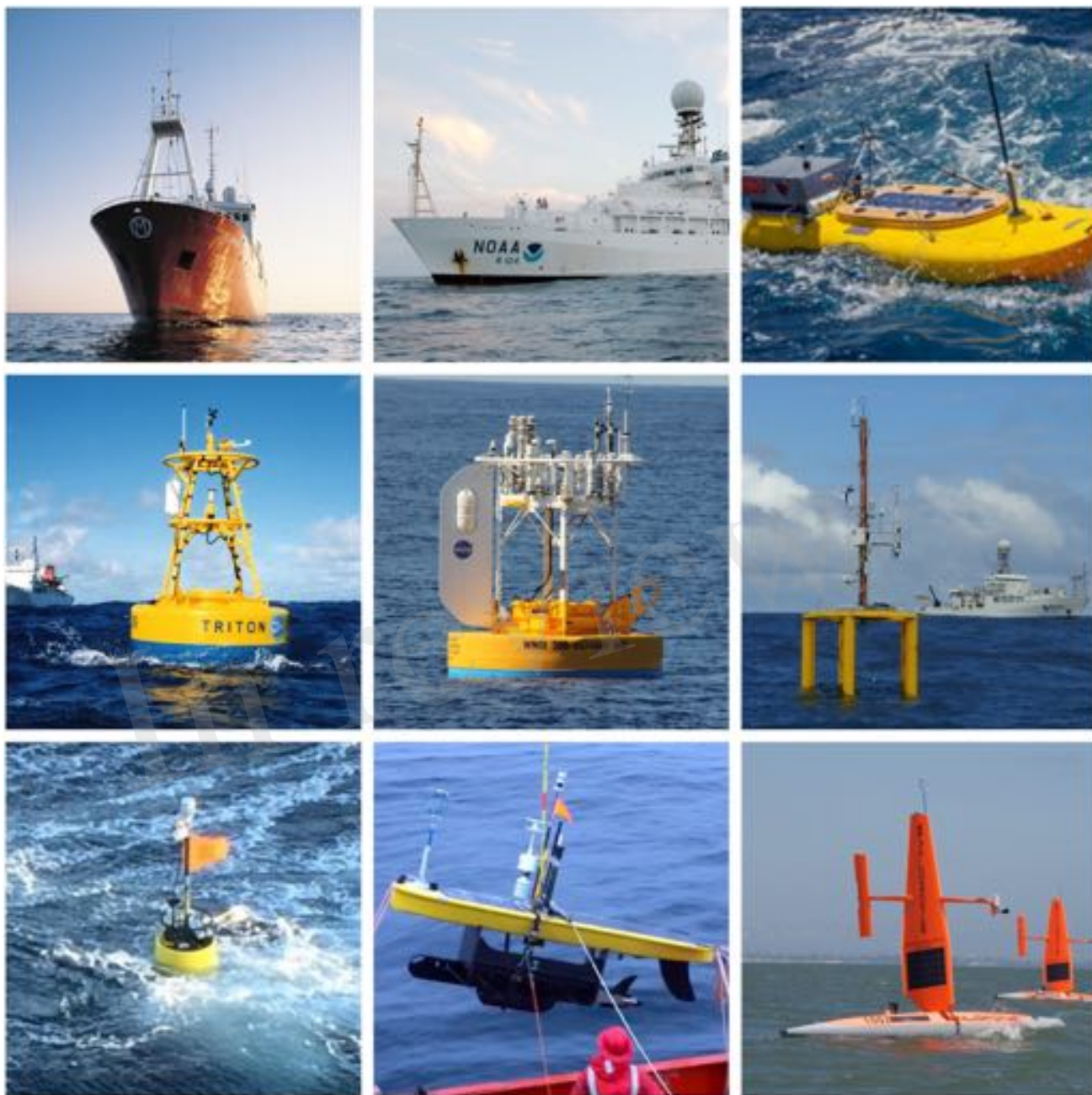


1822

1823 **Figure 2.** Target flux accuracy and scales for different phenomena. The space and time scales are indicated by the extent of the bubble. The target accuracies, estimated at 10 to 20% of the observed variability, are indicated by the color for net heat flux, and by the bubble's outline for surface stress. The accuracy requirement for stress is a factor of 2 smaller for phenomena that are dependent on the curl of the stress rather than the stress magnitude. See Table S1 for more detail. This figure is updated and adapted from Bourassa et al. (2013).

1829

1830

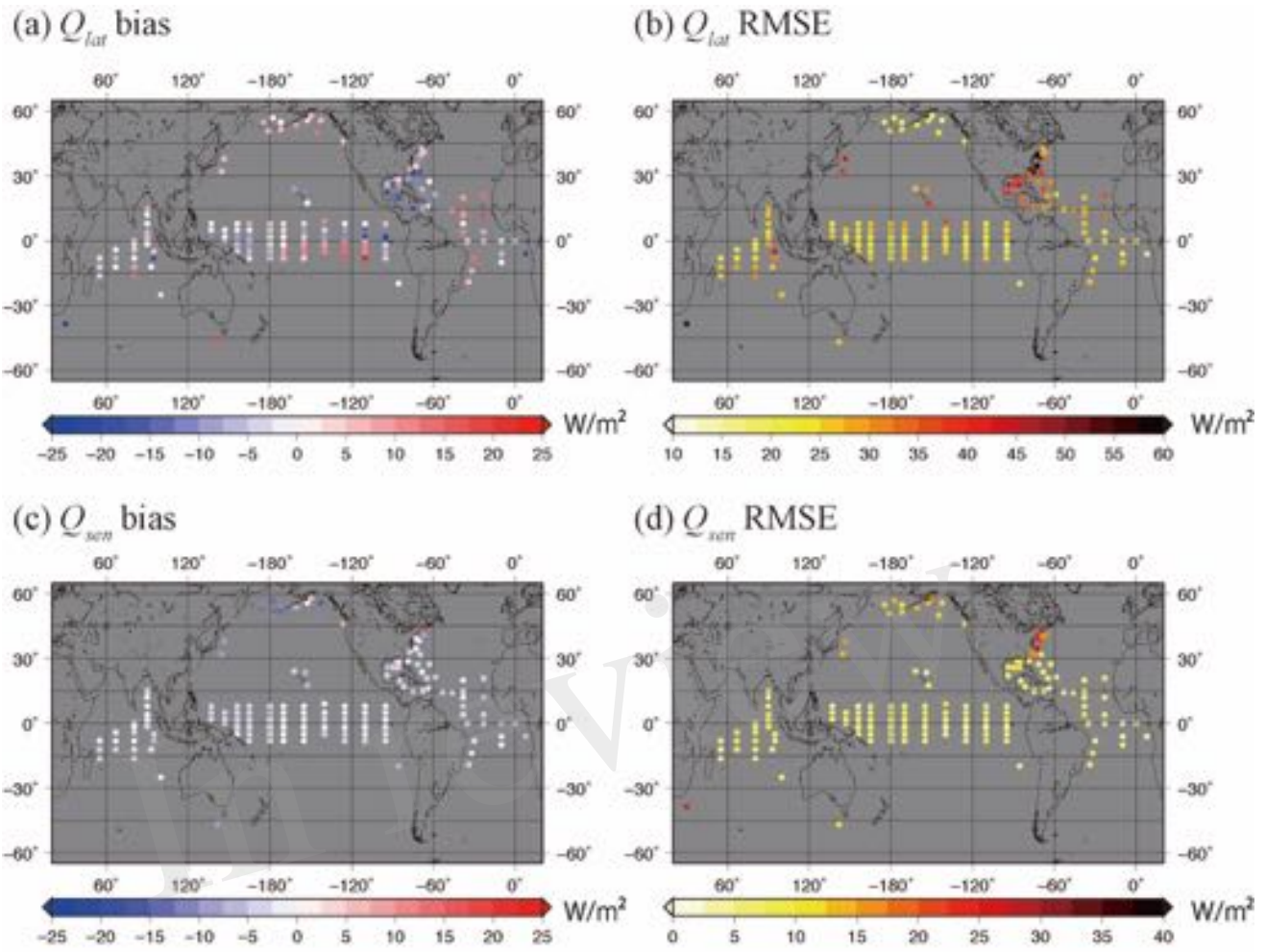


1831

1832 **Figure 3.** Examples of different types of air-sea flux *in situ* platforms. Clockwise from upper left:
 1833 UK weathership Polar Front (image courtesy of Norwegian Meteorological Institute); NOAA ship
 1834 Ron Brown (from www.noaa.gov); OSU “ROSS” ASV (ross.ceoas.oregonstate.edu; image courtesy
 1835 of San Nguyen, NguyenSan Photography); RSMAS “ASIS” spar buoy (Graber et al., 2000);
 1836 Saildrone, Inc. “Saildrone” ASV (image courtesy of Saildrone, Inc.; www.saildrone.com), Liquid
 1837 Robotics “Wave Glider” ASV (from www.liquid-robotics.com with modifications by UW/APL),
 1838 UW/APL “SWIFT” drifter (Thomson, 2012); JAMSTEC TRITON buoy (from JAMSTEC,
 1839 www.jamstec.go.jp); and, in the center, the WHOI SPURS buoy (Farrar et al., 2015).

1840

1841



1842

1843 **Figure 4.** Root mean square error and bias (satellite minus buoy)
 1844 between daily buoy and J-OFURO3 Q_{lat} and Q_{sen} (in Wm^{-2}) for the period 2002 – 2013. From Figure 5 of Tomita et al. (2019).

1845

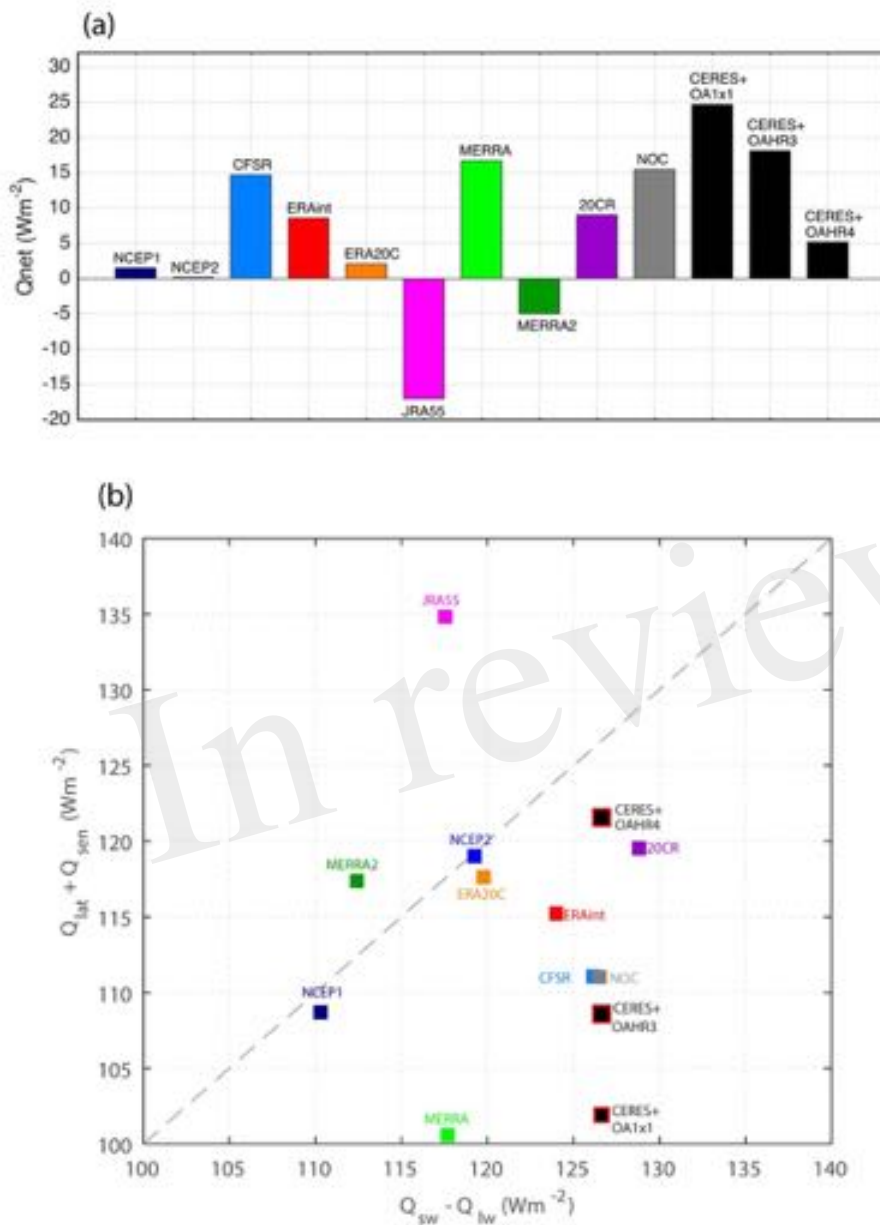
Variable	Instrument Type	Relevant Satellite Sensors - 2018-2030	Status and Actions
Ocean surface wind speed/direction	Radar scatterometers	ASCAT on MetOp-A, B, C; OSCAT on Seasat-1 and QuikSat-1, -2, -3, -4; SCAT & SWIM on CPODATE, Follow-On mission from 2022; WindSAT on FY-3E, 2H from 2030; SCAT on HY-2C, ZD, 2E, 2F from 2030; SCA on MetOp SG from 2022.	Technology and algorithms are mature, but directional accuracy needs improvement. Technology improvements to include Doppler could give better swath surface winds.
	PW& radiometers	WindSat* on TerraSats; AMSR2* on ECOM-W1; SMAP on DMSP F16, F17, F18; GMI on GPM Core Observatory.	Technology and algorithms are mature. Constellation is fragile. Sampling is poor. Speed only in most cases. Directional accuracy needs improvement.
	SAR	Sentinel 3 a & b, followed by c & d; TerraSar-X, TanDEM-X & PAZ; COSMO-SkyMed; RADARSAT-2; RADARSAT Constellation.	Technology is mature, algorithm improvement needed. High resolution, but very poor global coverage. Directional accuracy needs improvement.
	GNSS reflectometry	CYGNSS,*	Technology is quite mature, but GNSS satellites were not adequately intercalibrated, algorithm improvement needed. CYGNSS in tropics only, launched 2015 for two-year mission. Speed only. Long-term prospects unknown.
	Doppler LIDAR	Atmospheric Dynamics Mission - Aeolus.	Experimental, 2D wind profile in flight direction, component in look direction. Should reach into PBL. Launched in 2018 for a 3-year mission. Large footprint, and poor sampling.
Surface currents	SAR	Sentinel 3 a & b, followed by c & d; TerraSar-X, TanDEM-X & PAZ; COSMO-SkyMed; RADARSAT-2; RADARSAT Constellation.	Experimental, narrow swath, poor sampling, selected locations, current component only in look direction.
	Altimeters	Sentinel 3 a & b, followed by c & d; Jason 3, followed by Jason CS-4 and -5; SWOT in 2022	Mature technology and algorithms. Derived from surface topography using sub-satellite track using geodesy. SWOT is experimental. Resolution is roughly 200 km and 5 days.
Sea-surface temperature	IR radiometers – polar orbiters	AVHRR on NOAA-19, MetOp-B, -C; MODIS* on Terra and Aqua; VIIRS on S-NPP & NOAA-20; JPSS-2, -3; SLSTR on Sentinel 3 a & b, followed by c & d; AVNirage on MetOp SG from 2022.	Technology is mature, algorithm improvement needed to reach required goals.
	IR radiometers – geostationary	Imager on GOES-15; SEVIRI on MSG-10; Imager on INSAT-3, -3DR, -3D, AHI on Himawari-8, -9; ABI on GOES-16 (IR bands on GOES-17 have problems); AGR on FY-4A, -4B, -4C; GIRS on FY-4A, -4B, -4C, -4D; AMI on Geo-Kompsat-2A, FC on MTG-I.	Technology is mature, algorithm improvement needed to reach required goals.
	PW& radiometers	WindSat* on TerraSats – current; AMSR2* on ECOM-W1.	Technology is mature, algorithm improvement needed to reach required goals. Constellation is fragile.
Near-surface air temperature	IR sounders – polar orbiters	AIRS* on Aura; TES-N* on Aura; IASI on MetOp-B, -C; MSI-MG on MetOp SG from 2022; CRIS on S-NPP & NOAA-20; JPSS-2, -3.	Technology and algorithms mature for coarse resolution sounding; new algorithms, and probably new technology, needed for PBL temperature.
	IR sounders – geostationary	Sounder on GOES-15; Sounder on INSAT-3, -3DR, -3D; GIRS on FY-4A, -4B, -4C, -4D, -4E; IRS on MTG-I.	
	PW& radiometers	SSMIS on DMSP series; AMSU on MetOp-B, -C, and NOAA-20; ATMS on S-NPP & NOAA-20; JPSS-2, -3; MWS on MetOp SG from 2022.	
Near-surface air humidity	IR sounders – polar orbiters	AIRS* on Aura; IASI on MetOp-B, -C; MSI-MG on MetOp SG from 2022.	Technology and algorithms mature for coarse resolution sounding; new algorithms, and probably new technology, needed for PBL humidity.
	IR sounders – geostationary	Sounder on GOES-15; Sounder on INSAT-3, -3DR, -3D; GIRS on FY-4A, -4B, -4C, -4D, -4E; IRS on MTG-I.	
	PW& sounders	AMSU on Aura, MetOp-B, -C and NOAA-20; ATMS on S-NPP & NOAA-20; JPSS-2, -3; MWS on MetOp SG from 2022.	
Surface insolation	VISSR radiometers – polar orbiters & geostationary	CERES on Terra, Aqua, S-NPP, NOAA-20; RBN on JPSS-2 & -3 from 2022; Imager on GOES-15; SEVIRI on MSG-10; Imager on INSAT-3, -3DR, -3D, -3S; AHI on Himawari-8, -9; ABI on GOES-16 (IR bands on GOES-17 have problems); AGR on FY-4A, -4B, -4C; GIRS on FY-4A, -4B, -4C, -4D, -4E; AMI on Geo-Kompsat-2A, FC on MTG-I.	Highly derived, needing frequent samples (3 hr or better) of top-of-atmosphere emitted radiance, 3D distributions of clouds, aerosols, water vapor and some trace gases. Wind-speed-dependent surface albedo need to derive net insolation. Accuracy of input data and algorithms need improvement to reach goals.
Net surface infrared fluxes	VISSR radiometers – polar orbiters & geostationary	CERES on Terra, Aqua, S-NPP, NOAA-20; RBN on JPSS-2 & -3 from 2022; Imager on GOES-15; SEVIRI on MSG-10; Imager on INSAT-3, -3DR, -3D, -3S; AHI on Himawari-8, -9; ABI on GOES-16 (IR bands on GOES-17 have problems); AGR on FY-4A, -4B, -4C; GIRS on FY-4A, -4B, -4C, -4D, -4E; AMI on Geo-Kompsat-2A, FC on MTG-I.	Highly derived, needing frequent samples (3 hr or better) of top-of-atmosphere emitted radiance, 3D distributions of clouds, aerosols, water vapor and some trace gases, cloud base emissivity. Accurate skin SSTs and surface emissivity needed to derive net IR fluxes. Accuracy of input data and algorithms need improvement to reach goals.

1847 **Figure 5.** Satellite sensors that are producing data that can be used in deriving estimates of ocean
1848 surface fluxes. Normal text indicates current satellites and sensors, with * indicating those that are
1849 beyond their planned lifetime. Italic font shows missions that are expected to be launched in the next
1850 decade. Bold text shows areas needing attention in coming decade; red borders highlight where
1851 significant action and progress are needed. Not all derived variables from all sensors will reach the
1852 accuracies given in Table 3.

1853

1854

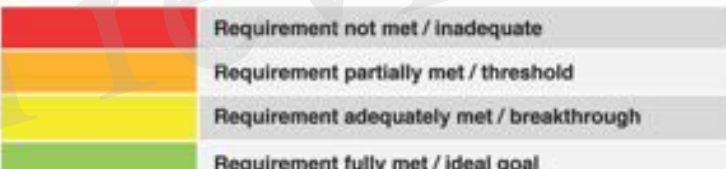
1855



1856

1857 **Figure 6.** (a) Global-ocean mean energy (Q_{net}) budget. (b) The ratio of the mean averages of $Q_{sw} - Q_{lw}$ to $Q_{lat} + Q_{sen}$; the dashed line denotes that this ratio equals 1.0. Abbreviations: 20CR, Twentieth
1858 Century Reanalysis; CERES, Clouds and the Earth's Radiant Energy System–Energy Balanced and
1859 Filled; CFSR, Climate Forecast System Reanalysis; ERA-20C, European Centre for Medium-Range
1860 Weather Forecasts Twentieth Century; ERA-Interim, European Centre for Medium-Range Weather
1861 Forecasts Interim; GPCP, Global Precipitation Climatology Project; JRA-55, Japanese 55-Year
1862 Reanalysis; MERRA, Modern-Era Retrospective Analysis for Research and Applications; NCEP,
1863 National Center for Environmental Prediction; NOC, National Oceanography Centre; OAFlux-1×1,
1864 1°-gridded Objectively Analyzed Air–Sea Fluxes; OAFlux-HR3 and -HR4, high-resolution (0.25°-
1865 gridded) Objectively Analyzed Air–Sea Fluxes analysis computed from Coupled Ocean–Atmosphere
1866 Response Experiment (COARE) version 3 and version 4, respectively. The 12 products used here are
1867 the same as used in Figure 1. From Yu (2019).

Flux EOV/ECV	2018	2019	2020	2021	2022	2023	2024	2025	2026	2027	2028	2029	2030
Bulk SST	Partially met											Adequate	
Skin Temperature	Partially met											Adequate	
Wind Speed and Direction	Partially met											Adequate	
Air Temperature	Not met											Adequate	
Humidity	Not met											Adequate	
Bulk Surface Currents	Partially met											Adequate	
Skin Surface Currents	Not met											Adequate	
Surface Solar Radiation	Partially met											Adequate	
Surface Longwave Radiation	Partially met											Adequate	
Albedo	Partially met											Met	
Sea State	Requirement Unknown											Requirement Known	



 Requirement not met / inadequate

Requirement partially met / threshold

Requirement adequately met / breakthrough

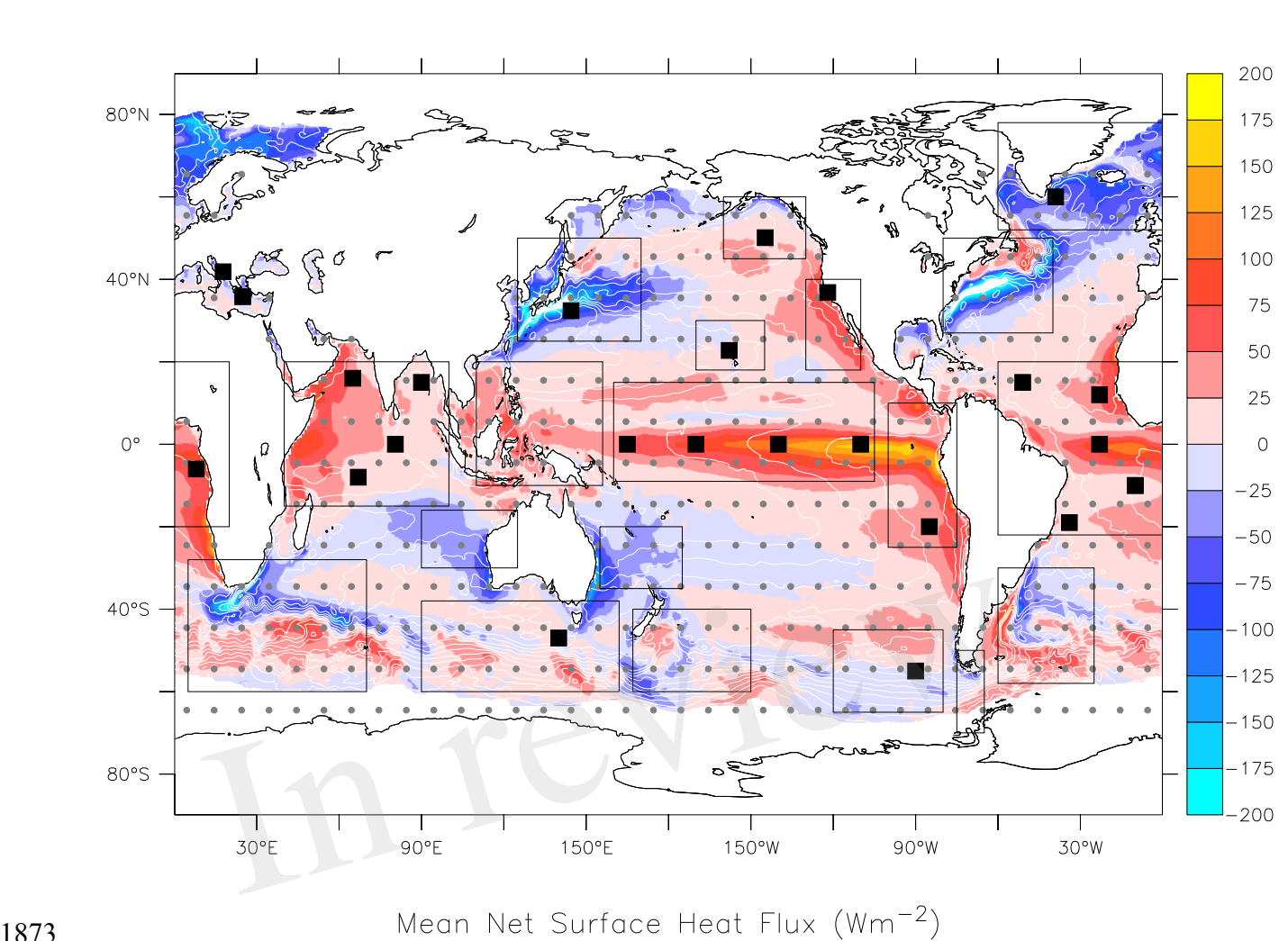
Requirement fully met / ideal goal

1869

1870 **Figure 7.** Overall status of flux EOV/ECV, assuming recommendations made here are followed.

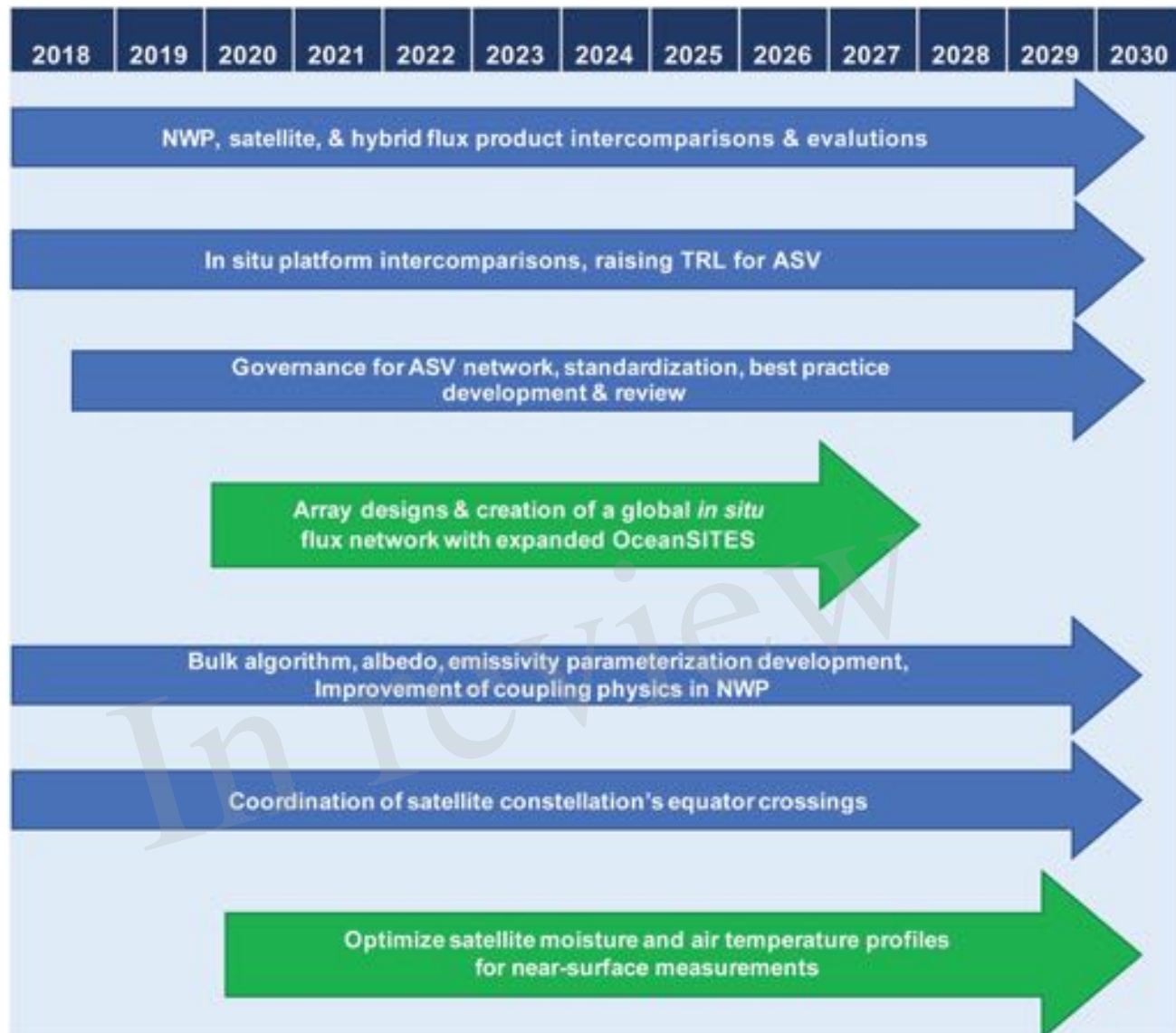
1871

1872



1873

1874 **Figure 8.** Existing OceanSITES network of surface heat fluxes (filled black squares) with priority
 1875 regions for new OceanSITES stations indicated by black boxes. The grey dots indicate nodes of a 10°
 1876 by 10° grid, with 368 grid boxes in the global oceans. The background mean net surface heat flux is
 1877 constructed from OAFlux-HR (Yu, 2019) and CERES EBAF (Kato et al., 2018) for the period of
 1878 2001–2015.



1879

1880

1881 **Figure 9.** Roadmap chart for making improvements in air-sea fluxes over the next decade. Major
1882 recommendation activities are indicated in green. Arrows indicate that these activities are likely to be
1883 ongoing.

1884

Figure 1.JPEG

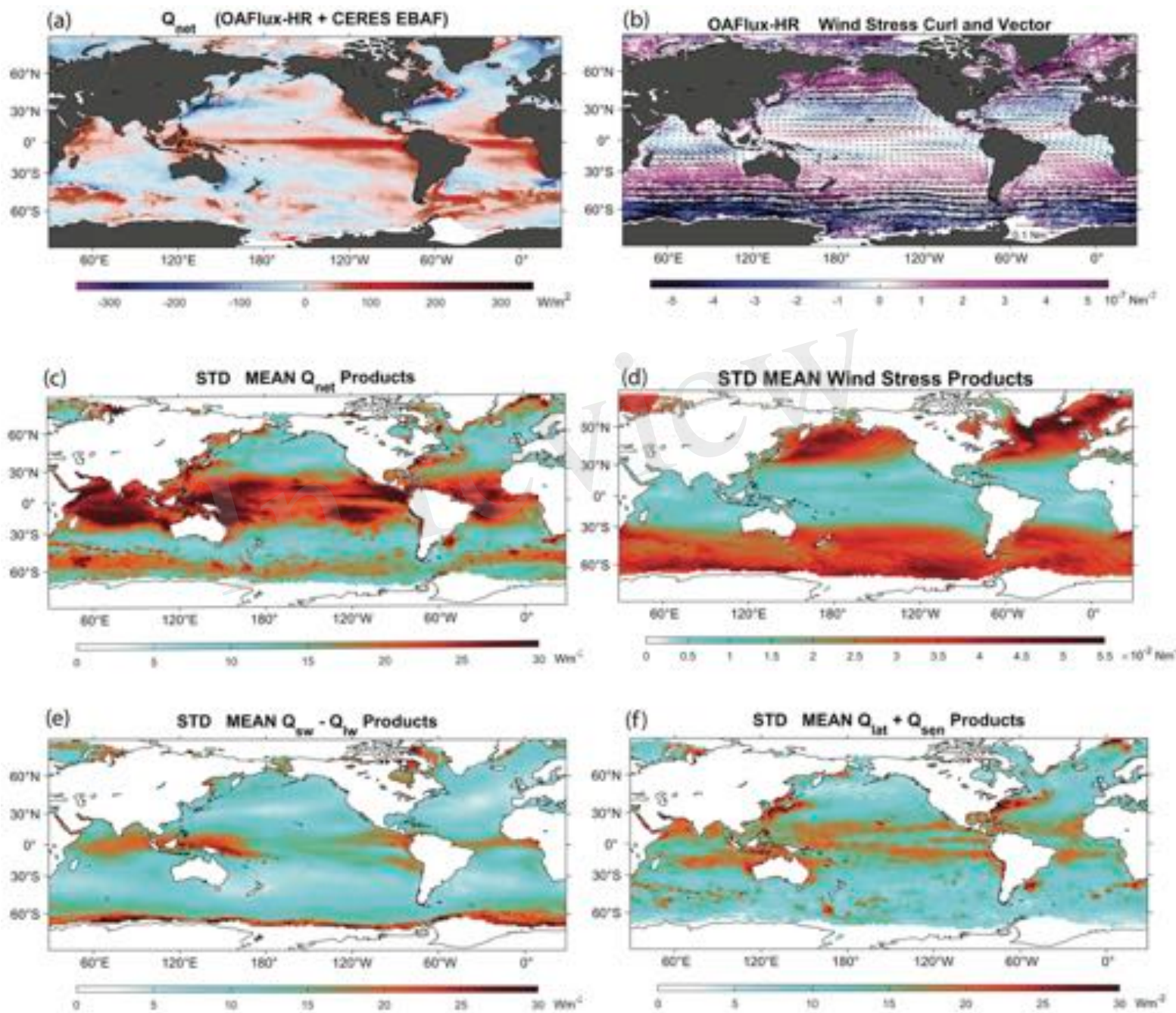


Figure 2.JPG

Flux Accuracies and Processes

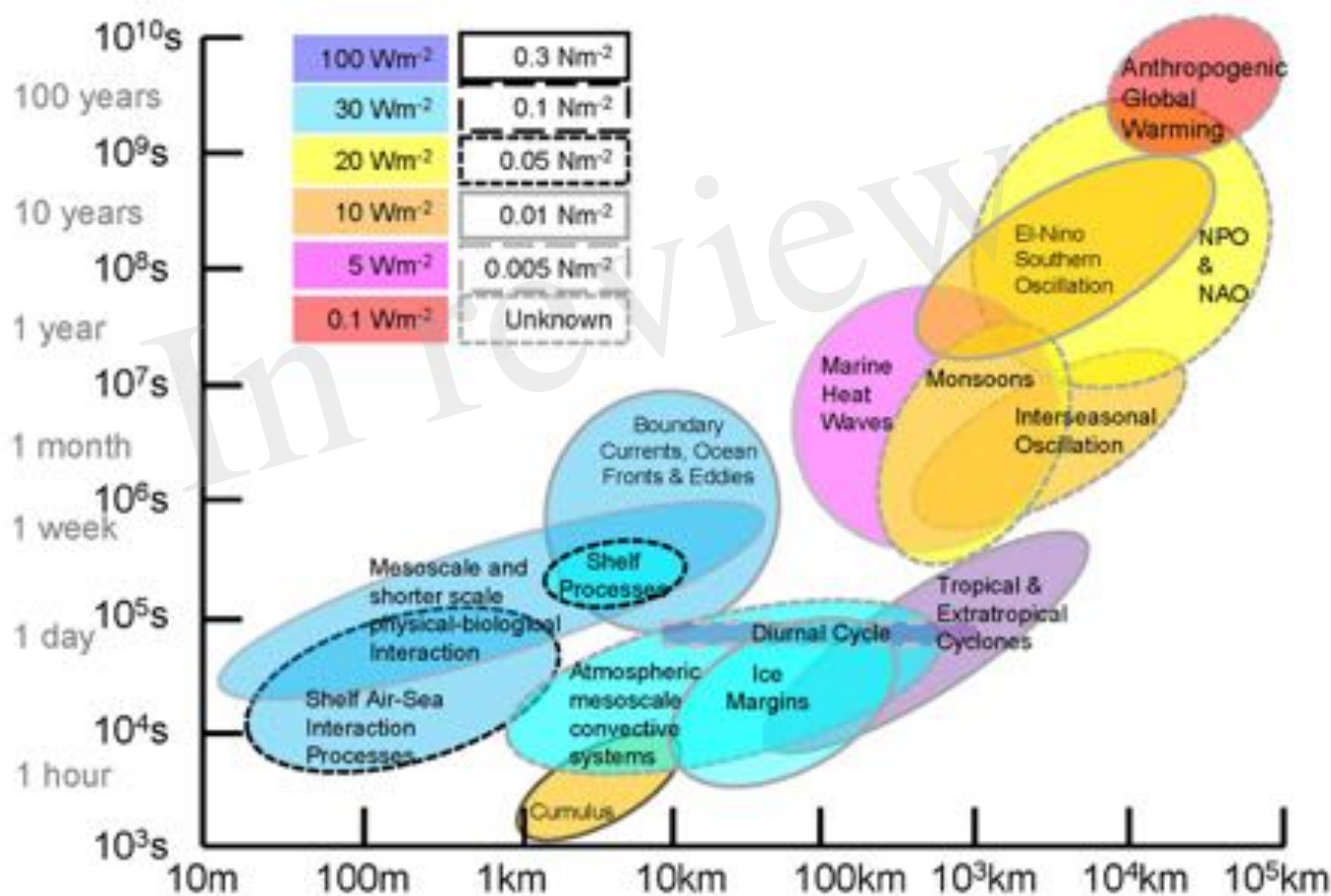
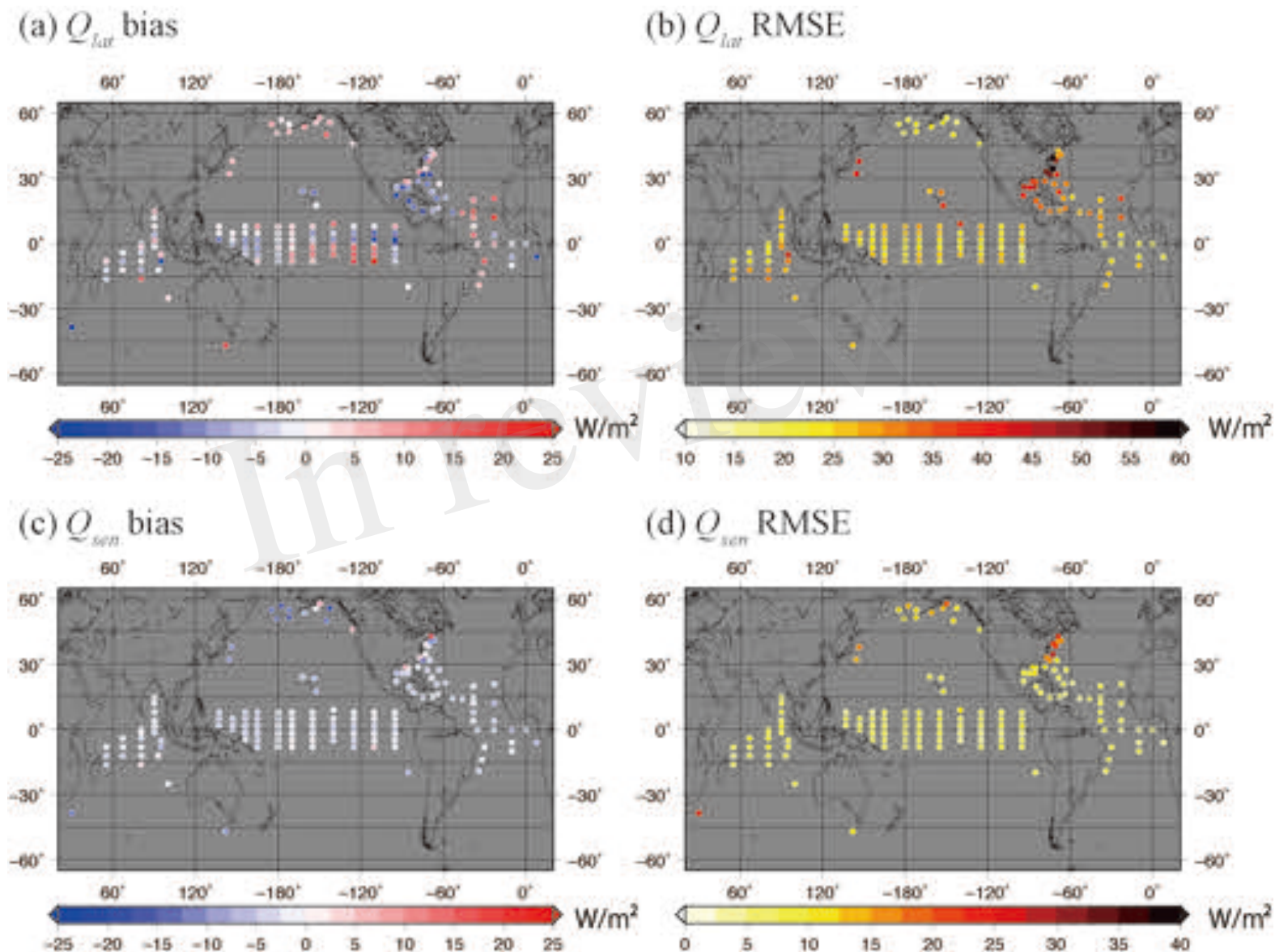


Figure 3.TIF



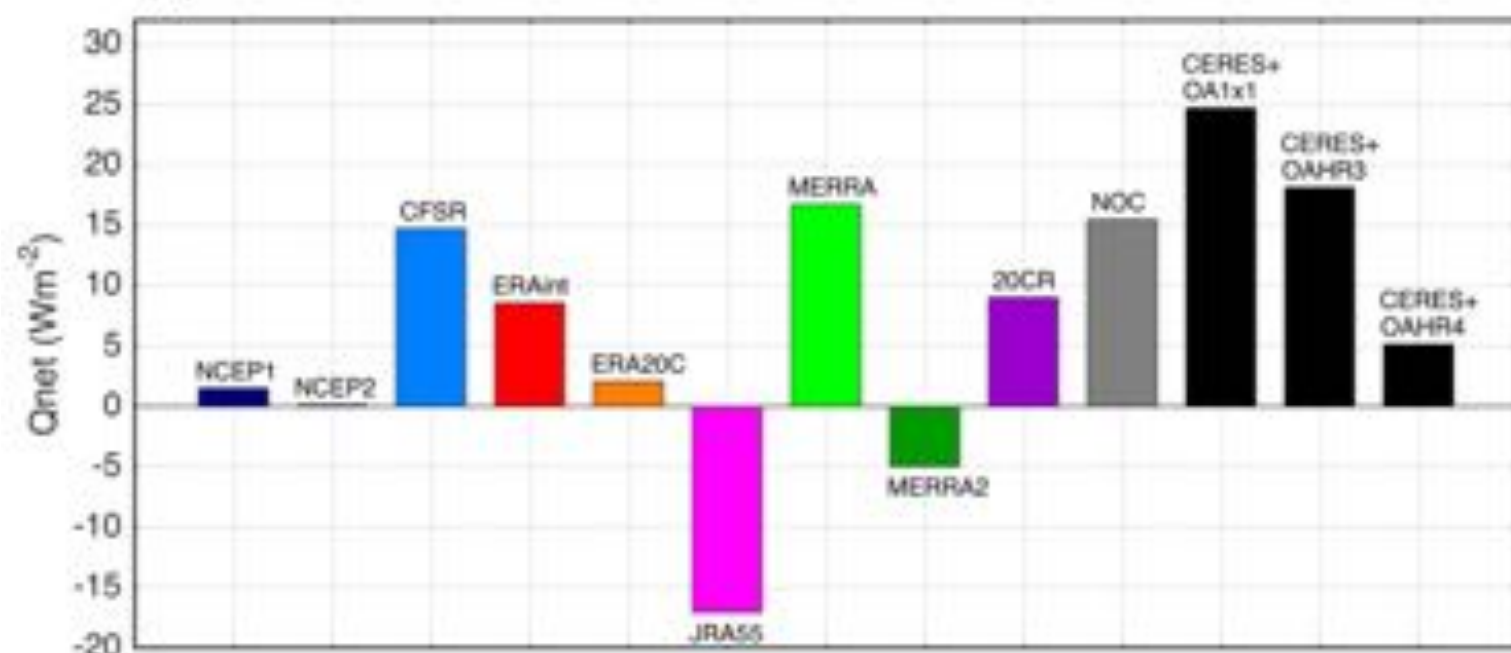
Figure 4.JPEG



Variable	Instrument type	Relevant Satellite Sensors (2018-2050)	Status and Actions
Ocean surface wind speed/direction	Radar scatterometers	ASCAT on MetOp-A, B, C; OSCAT on Seasat-1 and OceanSat-2, -3, -3A; SCAT & SWIM on CFOSAT, Follow-On mission from 2022; WindRAD on FY-3E, 3H from 2019; SCAT on HY-2C, 2D, 2E, 2F from 2019; SCA on MetOp SG from 2022.	Technology and algorithms are mature, but directional accuracy needs improvement. Technology improvements to include Doppler could give broad swath surface currents.
	PMW radiometers	WindSat® on Coriolis; AMSR2® on GCOM-W1; SSMS on DMSP F16, F17, F18; GMW on GPM Core Observatory	Technology and algorithms are mature. Constellation is fragile. Sampling is poor. Speed only in most cases. Directional accuracy needs improvement.
	SAR	Sentinel 1 a & b, followed by c & d; TerraSar-X, TanDEM-X & PAZ; COSMO-SkyMed; RADARSAT-2; RADARSAT Constellation.	Technology is mature, algorithm improvement needed. High resolution, but very poor global coverage. Directional accuracy needs improvement.
	GNSS reflectometry	CYGNSS®	Technology is quite mature, but GPS satellites were not adequately intercalibrated, algorithm improvement needed. CYGNSS in tropics only. Launched 2013 for two-year mission. Speed only. Long-term prospects unknown.
Surface currents	Doppler LIDAR	Atmospheric Dynamics Mission – Aeolus.	Experimental. 2D wind profile in flight direction, component in look direction. Should reach into PBL. Launched in 2018 for a 3-year mission. Large footprint, and poor sampling.
	SAR	Sentinel 1 a & b, followed by c & d; TerraSar-X, TanDEM-X & PAZ; COSMO-SkyMed; RADARSAT-2; RADARSAT Constellation.	Experimental, narrow swath, poor sampling, selected locations, current component only in look direction.
	Altimeters	Sentinel 3 a & b, followed by c & d; JASON 3, followed by JASON-CS-A and -B; SWOT in 2022.	Mature technology and algorithms. Derived from surface topography along sub-satellite track using geostrophy. SWOT is experimental. Resolution is roughly 200 km and 5 days.
Sea-surface temperature	IR radiometers – polar orbiters	AVHRR on NOAA-18, MetOp-B, -C; MODIS® on Terra and Aqua; VIIRS on S-NPP & NOAA-20; JPSS-2, -3; SLSTR on Sentinel 3 a & b, followed by c & d; MLIImage on MetOp SG from 2022.	Technology is mature, algorithm improvement needed to reach required goals.
	IR radiometers – geostationary	Imager on GOES-15; SEVIRI on MSG-3B; Imager on INSAT-3, -3DR, -3DS; AHI on Himawari-8, -9; ABI on GOES-16 (IR bands on GOES-17 have problems); AGRI on FY-4A, -4B, -4C; GIRS on FY-4A, -4B, -4C, -4D; AMI on Geo-Kompsat-2A; PCI on MTG-C	Technology is mature, algorithm improvement needed to reach required goals.
	PMW radiometers	WindSat® on Coriolis – current; AMSR2® on GCOM-W1.	Technology is mature, algorithm improvement needed to reach required goals. Constellation is fragile.
Near-surface air temperature	IR sounders – polar orbiters	AIRS® on Aqua; TES-N® on Aura; IASI on MetOp-B, -C; IASI-NG on MetOp SG from 2022; CRIS on S-NPP & NOAA-20; JPSS-2, -3.	Technology and algorithms mature for coarse resolution sounding; new algorithms, and probably new technology, needed for PBL temperature.
	IR sounders – geostationary	Sounder on GOES-15; Sounder on INSAT-3, -3DR, -3DS; GRS on FY-4A, -4B, -4C, -4D, -4E; IRS on MTG-S.	
Near-surface air humidity	PMW radiometers	SSMS on DMSP series; AMSU on MetOp-B, -C, and NOAA-19; ATMS on S-NPP & NOAA-20; JPSS-2, -3; MHS on MetOp SG from 2022.	
	IR sounders – polar orbiters	AIRS® on Aqua; IASI on MetOp-B, -C; IASI-NG on MetOp SG from 2022.	
	IR sounders – geostationary	Sounder on GOES-15; Sounder on INSAT-3, -3DR, -3DS; GRS on FY-4A, -4B, -4C, -4D, -4E; IRS on MTG-S.	Technology and algorithms mature for coarse resolution sounding; new algorithms, and probably new technology, needed for PBL humidity.
Surface insulation	PMW sounders	AMISU on Aqua, MetOp-B, -C and NOAA-19; ATMS on S-NPP & NOAA-20; JPSS-2, -3; MHS on MetOp SG from 2022.	
	VIS/IR radiometers – polar orbiters & geostationary	CERES on Terra, Aqua, S-NPP, NOAA-20; RBI on JPSS-2 & -3 from 2022; Imager on GOES-15; SEVIRI on MSG-3B; Imager on INSAT-3, -3DR, -3DS, -3DS; AHI on Himawari-8, -9; ABI on GOES-16 (IR bands on GOES-17 have problems); AGRI on FY-4A, -4B, -4C; GIRS on FY-4A, -4B, -4C, -4D, -4E; AMI on Geo-Kompsat-2A; PCI on MTG-C.	Highly derived, needing frequent samples (1 hr or better) of top-of-atmosphere emitted radiance, 3D distributions of clouds, aerosols, water vapor and some trace gases. Wind-speed dependent surface albedo need to derive net insulation. Accuracy of input data and algorithms need improvement to reach goals.
Net surface infrared fluxes	VIS/IR radiometers – polar orbiters & geostationary	CERES on Terra, Aqua, S-NPP, NOAA-20; RBI on JPSS-2 & -3 from 2022; Imager on GOES-15; SEVIRI on MSG-3B; Imager on INSAT-3, -3DR, -3DS, -3DS; AHI on Himawari-8, -9; ABI on GOES-16 (IR bands on GOES-17 have problems); AGRI on FY-4A, -4B, -4C; GIRS on FY-4A, -4B, -4C, -4D, -4E; AMI on Geo-Kompsat-2A; PCI on MTG-C.	Highly derived, needing frequent samples (1 hr or better) of top-of-atmosphere emitted radiance, 3D distributions of clouds, aerosols, water vapor and some trace gases; cloud base emissivity. Accurate skin TS% and surface emissivity needed to derive net IR fluxes. Accuracy of input data and algorithms need improvement to reach goals.

Figure 6.JPEG

(a)



(b)

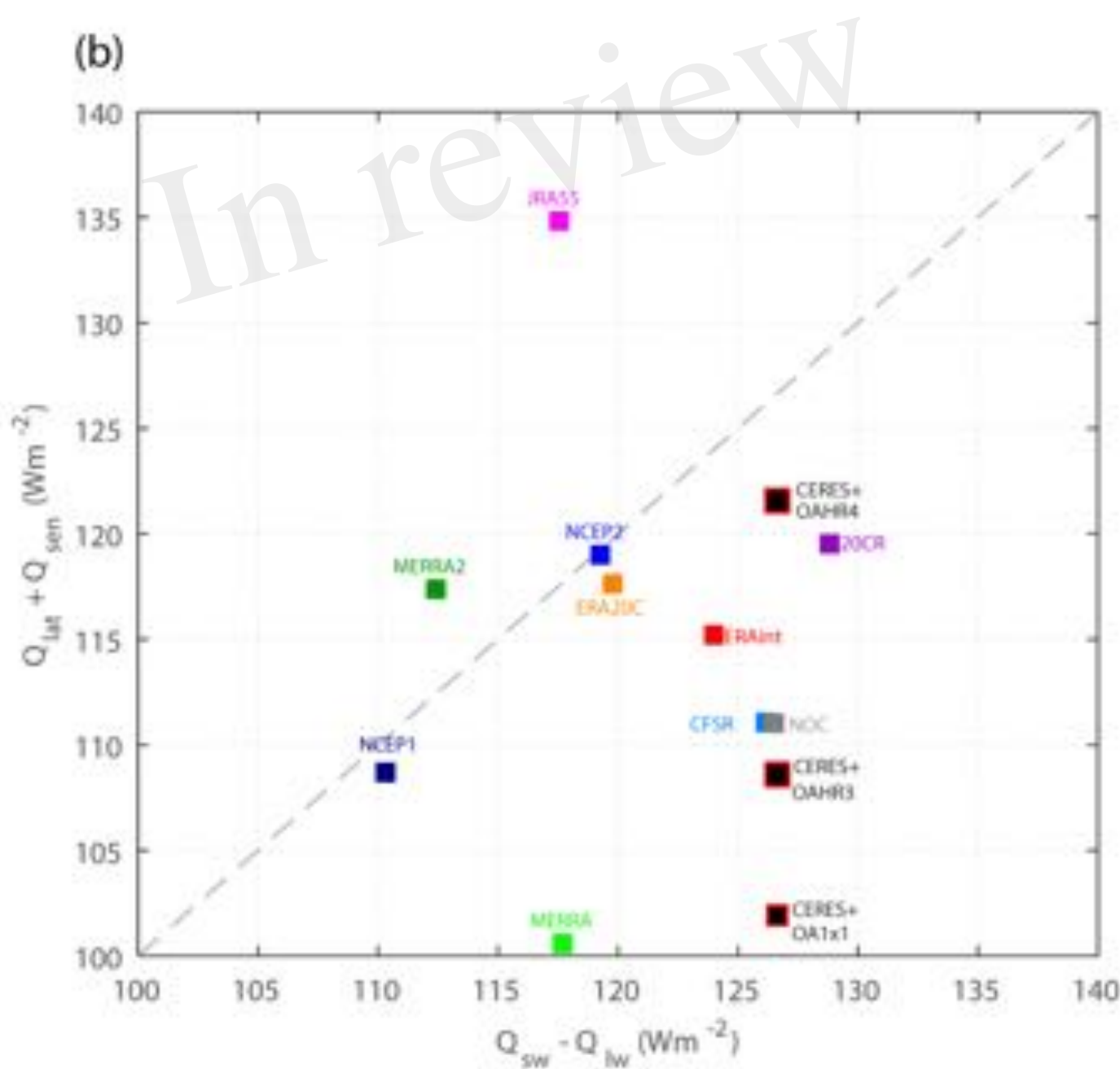


Figure 7.JPEG

Figure 8.JPEG

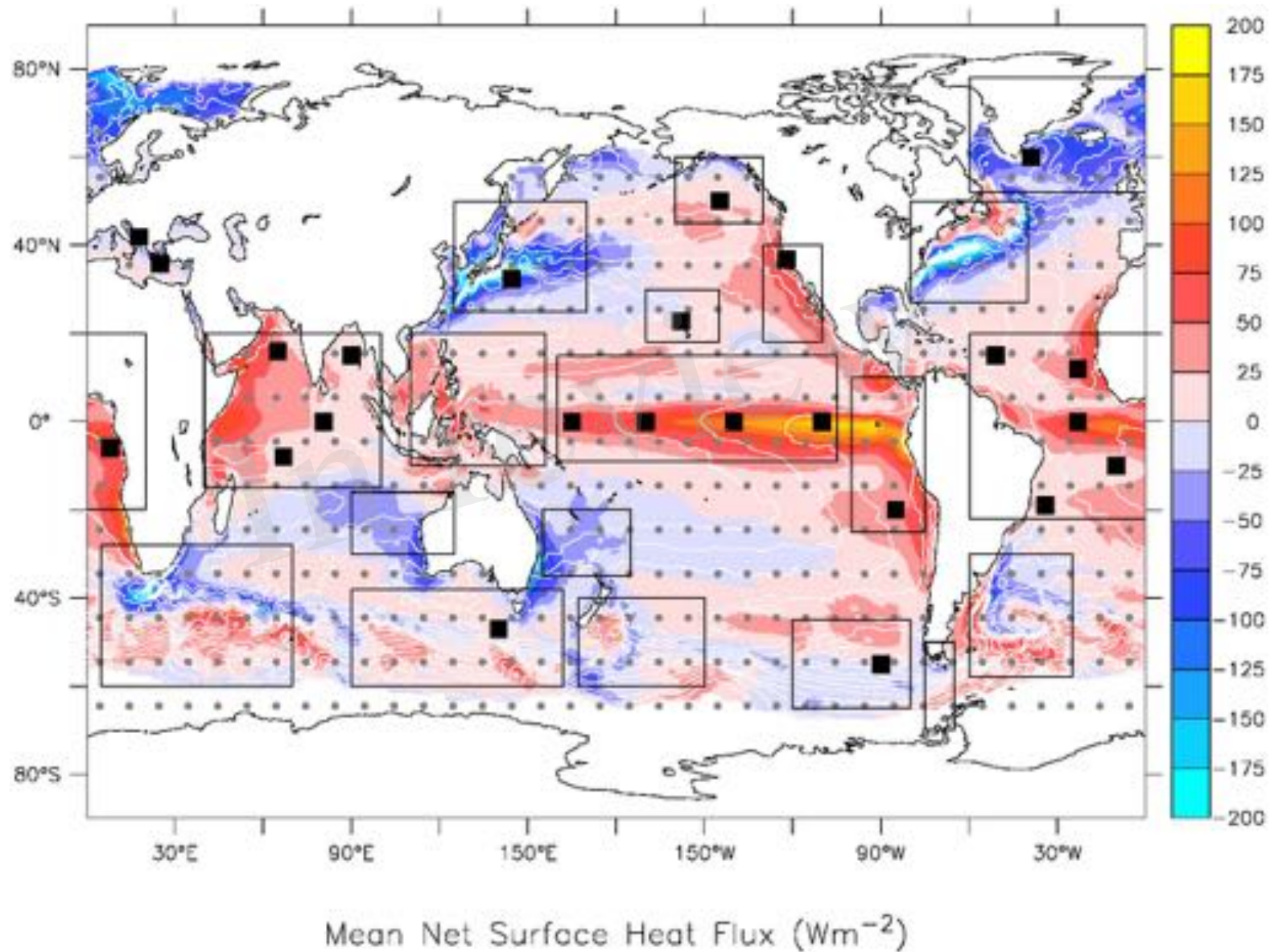


Figure 9.JPEG

